

**IDENTIFYING THE  
MINERALOGICAL INFLUENCES ON  
POROSITY-PERMEABILITY  
VARIATION IN SANDSTONE,  
USING SHORT-WAVE INFRARED  
SPECTROSCOPY:  
IMPLICATIONS FOR GEOTHERMAL  
POTENTIAL IN TWENTE**

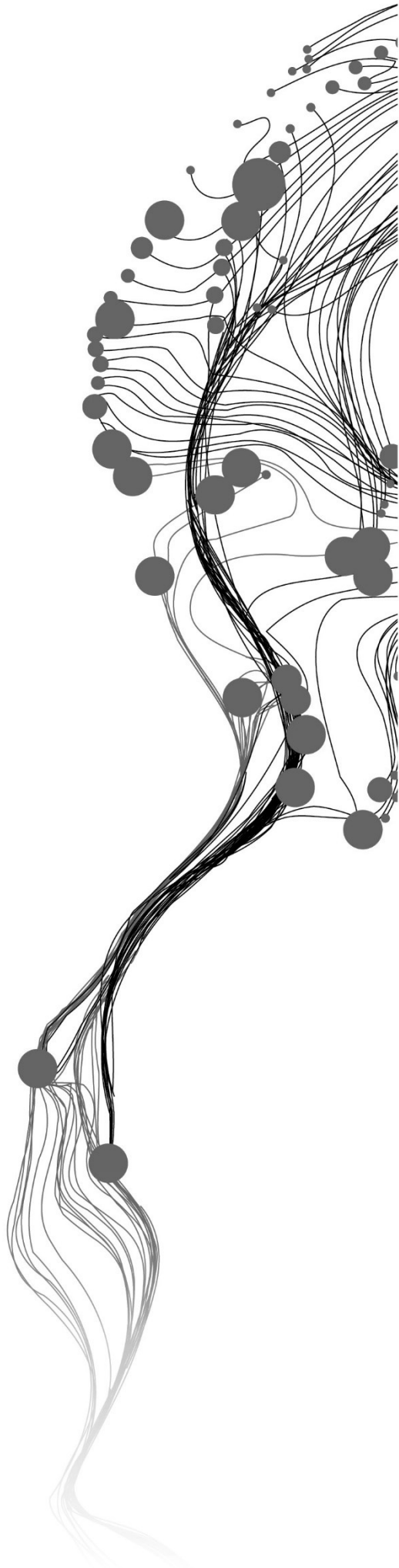
MAHASSEN KULUGAMMANA

July 2024

SUPERVISORS:

Dr. C.A. Hecker

Prof. dr. Mark van der Meijde



# **IDENTIFYING THE MINERALOGICAL INFLUENCES ON POROSITY-PERMEABILITY VARIATION IN SANDSTONE, USING SHORT-WAVE INFRARED SPECTROSCOPY: IMPLICATIONS FOR GEOTHERMAL POTENTIAL IN TWENTE**

MAHASEN KULUGAMMANA

Enschede, The Netherlands, July 2024

Thesis submitted to the Faculty of Geo-Information Science and Earth Observation of the University of Twente in partial fulfilment of the requirements for the degree of Master of Science in Geo-information Science and Earth Observation.

Specialization: Applied Remote Sensing for Earth Sciences

## **SUPERVISORS:**

Dr. C.A. Hecker

Prof. dr. M. van der Meijde

## **THESIS ASSESSMENT BOARD:**

Dr. H. van der Werff (Chair)

Dr. P. de Groot (External Examiner, dGB Earth Sciences)

#### DISCLAIMER

This document describes work undertaken as part of a programme of study at the Faculty of Geo-Information Science and Earth Observation of the University of Twente. All views and opinions expressed therein remain the sole responsibility of the author, and do not necessarily represent those of the Faculty.



# ABSTRACT

Geothermal energy development requires specific subsurface conditions to realise the resource economically. Geothermal energy is gradually becoming popular and developing as a clean, sustainable power source in the Netherlands. The Twente region in East Netherlands also carries out geothermal explorations focusing on the sandstone reservoirs in the *Tubbergen* Formation, which has been identified as having geothermal potential. Existing drillhole data from extensive hydrocarbon explorations within the region suggest that the porosity and permeability of the *Tubbergen* sandstone are highly variable, posing a risk for successful geothermal developments. Publicly available scientific information on the porosity-permeability variation is extremely rare to find. Thus, the current research used infrared spectroscopy techniques to reveal the mineralogical factors affecting the *Tubbergen* sandstone's porosity-permeability.

The study is based on the porosity-permeability data from two drill holes (*Fleringen 1/FLN* and *Reutum 1/REU*) located north of the University of Twente. Porosity-permeability data was measured on drill core plugs obtained from the depth levels of *Tubbergen* sandstone layers. The porosity vs permeability plot of the drillhole data shows two distinct trends. FLN samples create one trend while REU samples show another trend with relatively higher permeability values for the same porosity than FLN. The same core plugs were used to acquire shortwave infrared (SWIR) hyperspectral data and analyse the mineralogy to compare it with porosity-permeability data to identify the relationships between the two petrophysical properties and mineralogy.

SWIR data was mainly studied using principal component (PC) analysis. The first 12 PC bands were selected for useful information and to conduct further analysis. Mean PC values from each band for each sample were compared against porosity-permeability value to recognise the PC bands, which shows a trend with petrophysical properties. Identified PC bands were further analysed by comparing the image spectra from PCs' dark and bright pixel locations. Brightness intensity (albedo), kaolinite crystallinity (KC), illite/kaolinite relative proportion, and siderite were identified with SWIR data as the controlling factors of porosity permeability. Since PC bands can consist of multiple spectral information, band math operations were used to clarify the effect of individual factors. Mean values of the band math operations for each sample were compared against the porosity and permeability to identify the relationships.

Finally, it is revealed that high KC and siderite cause a reduction in porosity, while high illite to kaolinite relative proportions reduce both porosity and permeability. Albedo variation distinguishes the abundance of feldspar-quartz relative to clay, with high and low albedo values, respectively, and indicates a positive relationship with the porosity. As the next step, mineralogical factors were visualised on the SWIR data with linear spectral unmixing, using spectra of siderite, high KC kaolinite, low KC kaolinite, and illite as endmembers. Spectral unmixed results were visualised as RGB colour composite. Endmember distributions showed that illite content in REU is relatively low compared to FLN, which explains the high permeability values of REU samples.

**Key words:** Sandstone porosity-permeability, Tubbergen formation mineralogy, SWIR hyperspectral spectroscopy, Principle component analysis

## ACKNOWLEDGEMENTS

First and foremost, I thank my two supervisors, Dr Chris Hecker and Prof. Dr Mark van der Meijde, for their valuable guidance throughout the research. I highly acknowledge the Dutch Petroleum Company (NAM) for providing the drill core samples for the study. Next, I thank all the teachers who taught me and the members of the AES department for their valuable help during the MSc journey. I am forever thankful to the ITC Excellence Scholarship, which granted me the MSc opportunity.

I give heartfelt thanks to my ARS colleagues and ITC buddies for making my MSc journey a wonderful memory and sharing the joy as well as the sorrow in times of need.

I give my hearty gratitude to my loving parents for encouraging me from the beginning to the end of my studies. Also, I am forever in debt of my supportive two uncles “Loku thaththa” and “Hemachandra”. Without them, I couldn’t start my journey in the Netherlands.

# TABLE OF CONTENTS

---

Abstract .....	i
Acknowledgements .....	ii
Table of contents .....	iii
List of figures .....	v
List of tables .....	x
List of abbreviations .....	xi
List of Appendices.....	xii
1. Introduction.....	1
1.1. Geothermal Energy.....	1
1.1.1. Geothermal exploration in the Netherlands.....	1
1.1.2. Geothermal potential of the <i>Tubbergen</i> formation, Twente .....	2
1.2. Research Problem and Objectives.....	4
1.2.1. The main objective and the sub-objectives.....	4
1.2.2. Research questions.....	4
2. Research Data.....	5
2.1. Porosity and Permeability Data .....	5
2.2. SWIR Hyperspectral Data .....	5
3. Research Methodology.....	7
3.1. Porosity-Permeability Data Preparation.....	7
3.2. SWIR Imaging Spectroscopy of Drill Core Samples .....	8
3.2.1. Acquisition of SWIR hyperspectral data .....	8
3.2.2. Preprocessing of SWIR hyperspectral data.....	9
3.3. Identifying the Mineralogical Factors of Porosity-Permeability Variation.....	10
3.3.1. Principal component analysis of the SWIR hyperspectral image.....	11
3.3.2. Relationships between PC bands and porosity-permeability .....	11
3.3.3. Relationships between band math-derived mineralogical components and porosity-permeability .....	12
3.3.4. Visualising the distribution of identified mineralogical parameters using linear spectral unmixing .....	13
4. Results.....	14
4.1. Rearranged Porosity-Permeability Data .....	14
4.2. Pre-processed SWIR Hyperspectral Data .....	14
4.3. PCA results of SWIR Image.....	16
4.4. Relationships between PC Bands and Porosity-Permeability.....	21
4.5. Determining the Spectral Information of PC Bands .....	26
4.5.1. Analysis of FLN PC bands.....	26

4.5.2.	Analysis of REU PC bands .....	28
4.6.	Relationships between Band Math-Derived Mineralogical Components and Porosity-Permeability .....	30
4.6.1.	Albedo variation; using the reflectance value of SWIR band 1600.72nm .....	30
4.6.2.	Variation of kaolinite crystallinity (KC) .....	31
4.6.3.	Variation of ferrous iron (Fe <sup>2+</sup> ) response .....	33
4.6.4.	Variation of illite : kaolinite relative proportion .....	34
4.6.5.	Variation of illite spectral maturity (ISM) .....	35
4.7.	Visualising the Mineralogy Distribution Causing the Porosity-Permeability Variation .....	36
5.	Discussion.....	38
5.1.	Datasets .....	38
5.1.1.	Porosity and Permeability Datasets .....	38
5.1.2.	SWIR Hyperspectral Data.....	38
5.2.	Data Analysis.....	38
5.2.1.	PC band colour composites .....	38
5.2.2.	Relationships between PC bands and porosity-permeability.....	39
5.2.3.	PC band spectra analysis of FLN.....	40
5.2.4.	PC band spectra analysis of REU .....	40
5.2.5.	Comparison of PCA colour composite results and porosity scatterplots .....	42
5.3.	The Effects of Identified Mineralogical Variants to the Sandstone Porosity-Permeability .....	42
5.3.1.	The effect of SWIR albedo on porosity and permeability .....	42
5.3.2.	The effect of kaolinite crystallinity on porosity and permeability.....	43
5.3.3.	The effect of Fe <sup>2+</sup> response on porosity and permeability .....	44
5.3.4.	The effect of illite : kaolinite relative proportion on porosity and permeability .....	44
5.3.5.	The effect of illite spectral maturity on porosity and permeability.....	44
5.4.	Visualising the Distribution of Poro-Perm Controlling Mineralogy with Linear Spectral Unmixing.....	45
5.5.	Limitations in the Research .....	45
6.	Conclusions and recommendations.....	46
6.1.	Main Findings of the Research .....	46
6.2.	Further Refinements for the Current Research .....	46
6.3.	Future Research Potential.....	46
	List of references .....	49
	Appendices .....	53

# LIST OF FIGURES

---

## Chapter 1

Figure 1.1: Lateral extension of the *Tubbergen* formation. The *Tubbergen* formation and Gronau Fault Zone are only indicated within the Netherlands. They do not indicate the actual geographical extent; they are only illustrated for visual interpretation. Modified after TNO-GDN (2024) and Veenstra et al. (2020). .....3

Figure 1.2: Chronostratigraphy of the *Tubbergen* formation, which is grouped in onshore fluvial-lacustrine deposits, overlaid by *De Lutte* formation and underlaid by the *Maurits* formation. Modified after NLOG, (2024).....3

Figure 1.3: Porosity and permeability variation of *Tubbergen* sandstone in Twente from five drill holes: FLN – 01, TUM – 01, REU – 01, AMO – 03, and LUT – 06 (NLOG, 2023b). The *Tubbergen* formation is found at different levels between 1470 and 3193m depths. The sub-trend enclosed in a red ellipse shows the clean sandstone. REU-01 has higher permeabilities for lower porosities, and AMO-03 has high values for both porosity and permeability. C1, C2, and C3 clusters are demarcated to highlight the value variation. Modified after Veenstra et al. (2020). .....4

## Chapter 2

Figure 2.1: Four of the core plugs used in the research. (a) A plug from FLN on its vertical position with a labelled surface. (b) A plug from FLN on its horizontal position. (c) A disintegrated plug from FLN, which the permeability value is unavailable. (d) A plug from REU on its horizontal positions. Plugs from both drill holes are the same diameter, while the plug thickness of REU is higher than the FLN, as seen in (b) and (d). .....6

## Chapter 3

Figure 3.1: Textural comparison of two core plugs from FLN and REU with similar porosity and permeability. The FLN plug consists of loosely bound larger grains relative to the REU sample. REU consists of tightly arranged fine grains. ....8

Figure 3.2: The statistics plot of a single reflectance image with corrupt pixels and the band math operator for highlighting the spike-causing pixels in the red-coloured "Maximum" plot. Wavelength positions of all the troughs and crests were included in the band math operation. The shape of the "Mean" resulted from the plastic spectra because plastic pixels are more abundant than rock pixels. .... 10

Figure 3.3: Three reflectance spectra of the plastic scanning tray and indicated wavelength positions for the band math operation highlighting plastic. The spectra with low reflectance are from the tray's plug shadows, and the highest albedo spectrum is from a tray pixel with no illumination barrier. .... 10

## Chapter 4

Figure 4.1: The comparison of two laboratory poro-perm analysis reports from Germany and the Netherlands for FLN. (a) Porosity comparison. (b) Permeability comparison. Tabular data for the two plots is given in Appendix 2 ..... 14

Figure 4.2: Preprocessing results of HS reflectance data (RGB of (a) and (c) are 1499.41 nm, 1752.41 nm, and 1943.09 nm). (a) Reflectance image from SWIR HS raw data. Yellow arrow indicates splitting of a core plug. The plastic is seen in reddish colour due to the false colour composite. (b) Monochrome image to differentiate plastic vs rocks. (c) Image after the preprocessing: pixels of plastic, labels, and splitting were removed..... 14

Figure 4.3: The statistics plot of the pre-processed HS image mosaic. Note the disappearances of spikes in the "max" plot and the shapes of plastic spectra after the preprocessing when compared with Figure 3.2.

Absorption features from the dominant constituents from the rock pixels at 2200nm, 1900nm, and 1400nm wavelengths can be seen in mean plots. .... 15

Figure 4.4: Comparison of two spectral profiles of the same rock pixel before and after the “Fast mean 1+5+1 neighbourhood” smoothing filter. Small wiggles in the left spectrum have disappeared in the right spectrum after filtering. .... 15

Figure 4.5: An example of pixel spectra from quartz (in blue) and feldspar (in orange) clasts containing absorption features similar to plastic trays. The plastic spectrum is indicated in black colour. Plastic absorption feature positions, seen in quartz and feldspar, are indicated by dashed lines..... 16

Figure 4.6: Example spectra from minerals observed in the SWIR image. Characteristic wavelength ranges are highlighted in the same colour as in mineral spectra on the offset profiles. (a) Reflectance spectral profiles. (b) Offset reflectance profiles. (c) Continuum-removed offset reflectance profiles. Note that the broad feature of ferrous drop (blue spectrum) on the continuum-removed profile is not an actual absorption feature but an effect of hull-removal of the spectrum (Pontual et al., 1997c). .... 16

Figure 4.7: (a) RGB colour composite of the PC bands 3, 2, and 1 for FLN, showing the variations across the samples with the constituent PCs. (b) Labelled plugs in Figure 11a. The samples are organized in a downhole direction, going from top to bottom and then left to right. White areas are identical to the plugs in the left figure, and the black area is the masked pixels. Some plugs are incomplete (due to masking of sample number pen markings), so their labels are in white font. The Beginning of *De Lutte* formation is indicated as S-DL and the ending as E-DL. The beginning of the *Tubbergen* formation is indicated a..... 18

Figure 4.8: (a) RGB colour composite of the PC bands 3, 2, and 1 for REU, showing the variations across the samples with the constituent PCs. (b) Labelled plugs in Figure 12a. The samples are organized in a downhole direction, going from top to bottom and then left to right. White areas are identical to the plugs in the left figure, and the black area is the masked pixels. Some plugs are incomplete (due to masking of sample number pen markings), so their labels are in white font. .... 19

Figure 4.9: Porosity vs permeability plot of FLN with the colours from PCA colour composite in Figure 4.7, assigned to corresponding samples. Data point colours were chosen to represent the colours from PCA colour composite. Data points in the sharp horizontal bottom line are the 0.2 mD permeability samples (These samples do not have a permeability value in the original report since the minimum permeability measurement is 0.4 mD). .... 20

Figure 4.10: Porosity vs permeability plot of REU with the colours from PCA colour composite in Figure 4.8, assigned to corresponding samples. Data point colours were chosen to represent the colours from PCA colour composite. Data points in the sharp horizontal bottom line are the 0.2 mD permeability samples (These samples do not have a permeability value in the original report since the minimum permeability measurement is 0.4 mD). .... 20

Figure 4.11: Scatterplots of mean PC vs porosity for the FLN - 01. Blue points represent the mean PC value of each core plug and their measured porosities. Orange points denote only the most homogenous samples for the PC (1/3 of core plugs with the lowest SD). .... 22

Figure 4.12: Scatterplots of mean PC vs permeability for the FLN - 01. Blue points represent the mean PC value of each core plug and their measured porosities. Orange points denote only the most homogenous samples for the PC (1/3 of core plugs with the lowest SD). .... 23

Figure 4.13: Scatterplots of mean PC vs porosity for the REU. Blue points represent the mean PC value of each core plug and their measured porosities. Orange points denote only the most homogenous samples for the PC (1/3 of core plugs with the lowest SD). .... 24

Figure 4.14: Scatterplots of mean PC vs permeability for the REU. Blue points represent the mean PC value of each core plug and their measured porosities. Orange points denote only the most homogenous samples for the PC (1/3 of core plugs with the lowest SD)..... 25

Figure 4.15: Comparing 0.5% of the brightest (red) and darkest (blue) mean spectra of the PC1 band from FLN. (a) Reflectance spectral profiles. (b) Offset reflectance spectral profiles. (c) Continuum-removed offset spectral profiles. Characteristic absorption wavelength ranges of the kaolinite reference spectrum (Kokaly et al., 2017) are indicated with the same profile colour on offset spectral plots to distinguish the feature position on mean spectra. .... 26

Figure 4.16: Comparing 0.5% of the brightest (red) and darkest (blue) mean spectra of the PC2 band from FLN. (a) Reflectance spectral profiles. (b) Offset reflectance spectral profiles. (c) Continuum-removed offset spectral profiles. Characteristic absorption wavelength ranges of the kaolinite reference spectrum (Kokaly et al., 2017) are indicated with the same profile colour on offset spectral plots to distinguish the feature position on mean spectra. .... 27

Figure 4.17: Comparing 0.5% of the brightest (red) and darkest (blue) mean spectra of the PC3 band from FLN. (a) Reflectance spectral profiles. (b) Offset reflectance spectral profiles. (c) Continuum-removed offset spectral profiles. Characteristic absorption wavelength ranges of the kaolinite reference spectrum (Kokaly et al., 2017) are indicated with the same profile colour on offset spectral plots to distinguish the feature position on mean spectra. .... 27

Figure 4.18: Comparing 0.5% of the brightest (red) and darkest (blue) mean spectra of the PC5 band from FLN. (a) Reflectance spectral profiles. (b) Offset reflectance spectral profiles. (c) Continuum-removed offset spectral profiles. Characteristic absorption wavelength ranges of the kaolinite reference spectrum (Kokaly et al., 2017) are indicated with the same profile colour on offset spectral plots to distinguish the feature position on mean spectra. .... 28

Figure 4.19: Comparing 0.5% of the brightest (red) and darkest (blue) mean spectra of the PC1 band from REU. (a) Reflectance spectral profiles. (b) Offset reflectance spectral profiles. (c) Continuum-removed offset spectral profiles. Characteristic absorption wavelength ranges of kaolinite and illite reference spectra (Kokaly et al., 2017) are indicated with the same profile colours on offset spectral plots to distinguish the feature position on mean spectra. .... 29

Figure 4.20: Comparing 0.5% of the brightest (red) and darkest (blue) mean spectra of the PC2 band from REU. (a) Reflectance spectral profiles. (b) Offset reflectance spectral profiles. (c) Continuum-removed offset spectral profiles. Characteristic absorption wavelength ranges of kaolinite and ferroan dolomite reference spectra (Kokaly et al., 2017) are indicated with the same profile colours on offset spectral plots to distinguish the feature position on mean spectra. .... 29

Figure 4.21: Comparing 0.5% of the brightest (red) and darkest (blue) mean spectra of the PC8 band from REU. (a) Reflectance spectral profiles. (b) Offset reflectance spectral profiles. (c) Continuum-removed offset spectral profiles. Characteristic absorption wavelength ranges of kaolinite and ferroan dolomite reference spectra (Kokaly et al., 2017) are indicated with the same profile colours on offset spectral plots to distinguish the feature position on mean spectra. .... 30

Figure 4.22: Comparison between the monochrome images of (a) Image mosaic 1600.72nm wavelength band and (b) FLN PC1 band. .... 31

Figure 4.23: Scatterplots of mean 1600.72nm band value of FLN samples against porosity and permeability. The permeability plot has fewer data points than porosity due to samples with no values (disintegrated plugs) and values falling beyond the minimum measuring limits. .... 31

Figure 4.24: Scatterplots of mean 1600.72nm band value of REU samples against porosity and permeability. The permeability plot has fewer data points than porosity due to samples with no values (disintegrated plugs) and values falling beyond the minimum measuring limits.....31

Figure 4.25: Kaolinite crystallinity variation in the dataset, calculated using the given band math operation to indicate the variation of the absorption feature intensity within the highlighted wavelength region. The colour intensity variation is proportional to the crystallinity intensity, where the highest crystallinity is shown in the strong red colour, and the weak crystallinity is shown in faded red. ....32

Figure 4.26: Scatterplots of mean KC of FLN samples against porosity and permeability. The permeability plot has fewer data points than porosity due to the samples with no values (disintegrated plugs) and values falling beyond the minimum measuring limits. ....32

Figure 4.27: Scatterplots of mean KC of REU samples against porosity and permeability. The permeability plot has fewer data points than porosity due to samples with no values (disintegrated plugs) and values falling beyond the minimum measuring limits. ....32

Figure 4.28: Fe<sup>2+</sup> response variation in the dataset, which was calculated using the given band ratio to indicate the variation of the presence of Fe<sup>2+</sup>. The colour intensity variation is proportional to the crystallinity intensity, where the highest response is shown in the strong red colour, and the weak response is shown in faded blue. ....33

Figure 4.29: Scatterplots of mean Fe<sup>2+</sup> response of FLN samples against porosity and permeability. The permeability plot has fewer data points than porosity due to samples with no values (disintegrated plugs) and values falling beyond the minimum measuring limits.....33

Figure 4.30: Scatterplots of mean Fe<sup>2+</sup> response of REU samples against porosity and permeability. The permeability plot has fewer data points than porosity due to samples with no values (disintegrated plugs) and values falling beyond the minimum measuring limits.....33

Figure 4.31: The variation of illite : kaolinite relative proportion in the dataset, which was calculated using the given band ratio. The colour intensity variation is proportional to the relative proportion, where 100% illite (0% kaolinite) is indicated with a strong purple colour, and 100% kaolinite (0% illite) is indicated with a strong tan colour. ....34

Figure 4.32: Scatterplots of mean illite : kaolinite of FLN samples against porosity and permeability. The permeability plot has fewer data points than porosity due to samples with no values (disintegrated plugs) and values falling beyond the minimum measuring limits.....34

Figure 4.33: Scatterplots of mean illite : kaolinite of REU samples against porosity and permeability. The permeability plot has fewer data points than porosity due to samples with no values (disintegrated plugs) and values falling beyond the minimum measuring limits.....34

Figure 4.34: The ISM variation in the dataset, which was calculated using the given depth ratio, where the depths were calculated on continuum-removed spectra. Pure illite spectra from the dataset are shown in dark yellow, and ISM variation is shown in purple. The colour intensity variation is proportional to the calculated intensity, where the highest ISM is shown in the strong purple, and the weak crystallinity is shown in faded purple. ....35

Figure 4.35: Scatterplots of mean IC of FLN samples against porosity and permeability. The permeability plot has fewer data points than porosity due to samples with no values (disintegrated plugs) and values falling beyond the minimum measuring limit. ....35

Figure 4.36: Scatterplots of mean IC of REU samples against porosity and permeability. The permeability plot has fewer data points than porosity due to samples with no values (disintegrated plugs) and values falling beyond the minimum measuring limits..... 35

Figure 4.37: Spectral profiles of endmember spectra extracted from the SWIR data for the linear unmixing classification..... 36

Figure 4.38: Endmember RGB colour composites of linear spectral unmixing of the mosaic image. A colour composite consists of both FLN and REU datasets and the boundary between the two datasets is demarcated with a line. The beginning and end of the *De Lutte* samples are indicated in the FLN section as in the legend. Both colour composites have the same endmember/mineralogy for green and blue colours for convenience comparisons. .... 37

## Chapter 5

Figure 5.1: Porosity and permeability distribution of the samples from *De Lutte* formation relative to the *Tubbergen* formation values. *De Lutte* samples cover the complete poro-perm range of the *Tubbergen* samples. .... 38

Figure 5.2: Comparison of feldspar-quartz-rich and clay-rich samples using true colour, PC band 1, and SWIR band 1600.72nm. Variation of mineral enrichments is seen in different colour tones. .... 43

Figure 5.3: Comparison of albedo variation in a core plug with feldspar and quartz clasts between the PC band 1 and SWIR band 1600.72. Feldspar clasts are encircled in green, and quartz is encircled in blue in the three images. .... 43

## LIST OF TABLES

---

Table 2.1: A summary of the drill holes where the core plugs were obtained. The section that belongs to <i>De Lutte</i> formation is highlighted in grey.....	5
Table 3.1: Instrument configuration for HSI acquisition .....	9
Table 4.1: PCA Statistics of the first 12 principal components of FLN and the scree plot of eigen values.	17
Table 4.2: PCA Statistics of the first 12 principal components of REU and the scree plot of eigen values. .....	17
Table 4.3: Summary of the mineralogy identified as causing poor-perm heterogeneity.....	36
Table 5.1: Summary of PC band spectral information from PCA of FLN and REU, with clear trends in Porosity vs mean PC scatterplots. ....	41

## LIST OF ABBREVIATIONS

---

EM	Electromagnetic
FLN	<i>Fleringen 1</i>
HS	Hyperspectral
HSI	Hyperspectral imaging
IC	Illite crystallinity
IR	Infrared
ISM	Illite spectral maturity
KC	Kaolinite crystallinity
NAM	<i>Nederlandse Aardolie Maatschappij</i>
PC	Principal component
PCA	Principal component analysis
RE	Renewable energy
REU	<i>Reutum 1</i>
SD	Standard deviation
SWIR	Short wave infrared
SWIR band 1600.72nm	B <sub>1600.72</sub>
TIR	Thermal infrared
USGS	United states geological survey
VNIR	Visible-near infrared

## LIST OF APPENDICES

---

Appendix 1: Porosity-Permeability data of FLN - 01. * indicates the disintegrated plugs, which do not have permeability values. Data were obtained from the core analysis report compiled by NAM (Kernanalyse   NAM 370.08.19   Fleringen 1 (NLOG, 2023b)). The original report does not contain sample numbers. Permeability values indicated as “< 0.4 mD” were replaced with 0.2 mD.....	53
Appendix 2: Porosity-permeability analyses of 61 FLN samples from two laboratories: <i>C. Deilmann</i> Mining Company (Germany) and <i>NAM</i> (Netherlands). A 0.05 – 0.1m difference is seen in the mentioned depths between the two reports, possibly caused by the measurement scale.....	59
Appendix 3: Porosity-Permeability data of REU - 01. * Indicates the disintegrated plugs which do not have permeability values. Data were obtained from the core analysis report compiled by NAM (Core Analysis, Reutum 1 (NLOG, 2023b)). Permeability values indicated as “< 0.4 mD” were replaced with 0.2 mD.....	61
Appendix 4: Scatterplots of FLN Porosity vs Standard Deviation (SD) of the first 12 Principal Component (PC) bands.....	63
Appendix 5: Scatterplots of FLN Permeability vs Standard Deviation (SD) of the first 12 Principal Component (PC) bands.....	64
Appendix 6: Scatterplots of REU Porosity vs Standard Deviation (SD) of the first 12 Principal Component (PC) bands.....	65
Appendix 7: Scatterplots of REU Permeability vs Standard Deviation (SD) of the first 12 Principal Component (PC) bands.....	66

# 1. INTRODUCTION

## 1.1. Geothermal Energy

Geothermal resources contain the heat energy beneath the Earth's surface, encapsulated within rocks, aquifers, and confined steam. For these resources to be viable, the underground rock structures must possess enough porosity to retain fluids or steam that draws thermal energy from the surrounding rocks. Additionally, these formations should have the necessary permeability to allow the movement of fluids (Goldstein et al., 2011). This fluid movement is essential for extracting energy in economically feasible quantities. Therefore, porosity-permeability (poro-perm) is a critical element in evaluating the potential of geothermal reservoirs (Worden et al., 2018).

Poro-perm is primarily determined by the size and shape of grains, the spatial distribution of particles, and the diagenetic alterations they undergo (Boggs, 2009). In particular, the formation of in-situ sedimentary minerals (authigenic minerals), mineral hydration, and the compaction due to sediment burial tend to reduce poro-perm, whereas dissolution processes enhance it (Wolela & Gierlowski-Kordesch, 2007). Common structural grains such as quartz, feldspar, and mica originate from initial sedimentary deposits (Tucker, 2001), while diagenesis and mechanical infiltration introduce clays and muds (Walker et al., 1978; Whetten & Hawkins, 1972). Also, carbonates and evaporites play a significant role in developing and creating secondary porosity (Schmidt et al., 1977). Morad et al. (2010) outlined the standard diagenetic sequence in sandstones, which includes mechanical compaction, dissolution of less stable materials, coating of grains, substitution by clays, carbonate cementation, and mineral overgrowth. Notably, these diagenetic processes greatly influence the heterogeneity of sandstone reservoirs and, as a result, their overall quality.

### 1.1.1. Geothermal exploration in the Netherlands

Presently, The Netherlands is exploring and investing in all the potential renewable energy (RE) sources to reach their energy target of 100% from REs by 2050, as for many other countries (Hannan et al., 2021). In 2022, 15% of the Netherlands' total energy was generated from RE sources, where biomass, wind, and solar are the main contributors, while geothermal and other sources contributed a minor percentage (CBS, 2023a). Although the Netherlands started the development of geothermal resources a few decades ago, geothermal energy accounts for just over 1% of the total energy (including electricity) (CBS, 2023). Nevertheless, the potential for geothermal energy within the Dutch subsurface is believed to be greater than what is currently being utilised (Mijnlieff, 2020). The geothermal reservoirs in the Netherlands, much like the country's hydrocarbon reservoirs, are situated within sedimentary rock formations, which consist of porous and permeable sandstone and carbonates of Cenozoic, Upper Jurassic to Lower Cretaceous, Triassic, Rotliegend, and Lower Carboniferous ages (MEA, 2017).

The extensive hydrocarbon exploration and extraction activities carried out in the Netherlands over the years have yielded a wealth of subsurface geological data, which is also invaluable for geothermal exploration, especially in regions that have not yet been investigated specifically for geothermal energy, due to the similarities between hydrocarbon and geothermal reservoirs. The geothermal resources in the Netherlands are classified as low-temperature systems, with an average geothermal gradient of  $31^{\circ}\text{Ckm}^{-1}$  (Bonté et al., 2012).

Like hydrocarbon reservoirs in the Netherlands, the yield of geothermal reservoirs is a key factor (Mijnlieff, 2020) directly linked to reservoir quality. Therefore, investigating reservoir mineralogy is crucial for poro-perm evaluation (Goldstein et al., 2011). According to Buijze et al. (2023), about 20 geothermal projects are

currently active that produce appropriate temperatures for agriculture and district heating, using the primary poro-perm in sedimentary rocks.

The current operational geothermal wells use fluids from reservoirs with a minimum permeability of 50 mD and a minimum of 15% (Buijze et al., 2023). Reservoir thicknesses range from 50 to 200m, and the transmissivity (the rate of horizontal groundwater flow within the aquifer, thus, proportional to permeability and reservoir thickness) varies from 5 – 100 Dm. Even though the temperature is increased towards depth, in general, porosity, permeability, and transmissivity are typically reduced with increasing depth. The minimum transmissivity of 10 Dm is required for economically successful geothermal projects (Mijnlieff, 2020). Accordingly, the optimal depth range for geothermal energy realisations with sufficient heat and transmissivity is often considered the 1500 – 3000m range (Buijze et al., 2023). The Netherlands' most widely available geothermal system is known as "doublet", which comprises two wells for extraction/production and injection, developed into the same reservoir. The two wells are connected through a heat exchanger at the surface.

### 1.1.2. Geothermal potential of the *Tubbergen* formation, Twente

The eastern part of the *Overijssel* province of the Netherlands is known as *Twente*. Geothermal explorations are ongoing in the region, but no production wells have been established yet (NLOG, 2023). Using the information from the existing drill holes, researchers have recognised that the sandstone reservoirs within the *Tubbergen* formation carry geothermal potential (Mijnlieff, 2020; Veenstra et al., 2020). The formation is named after the Dutch village *Tubbergen*. The formation's lateral extension covers most of the northeastern part of the country's subsurface (Figure 1.1), making the *Tubbergen* formation a suitable target for further investigation. The University of Twente is also considering establishing a geothermal well within the premises, possibly targeting the *Tubbergen* Formation, which is an additional inspiration for the current research.

According to the TNO-GDN (2024), the formation is characterised by layers of sandstone, mudstone, and occasional narrow coal seams varying in thicknesses. The sandstone grain sizes range from fine to very coarse, with a moderate degree of sorting. Thus, the depositional setting of the formation is depicted as a braided fluvial environment from the late Carboniferous age (Figure 1.2). Braided fluvial depositional environments are dynamic over time due to energy variation of the water flow. Therefore, the depositional sequence becomes heterogeneous with depth. The *Maurits* formation underlies the *Tubbergen* formation and can be recognised by increasing coal seams in mudstone with lesser sandstones towards depth. On top of the *Tubbergen*, *De Lutte* formation is available and identified by dominating reddish-brown sandy mudstone (Figure 1.2).

Veenstra et al. (2020) showed the poro-perm variation of the *Tubbergen* formation using publicly available data to assess the geothermal potential. Porosity varies from extremely low values to 20%, and permeability also varies from very low values to several hundreds of millidarcy, as shown in Figure 1.3 (permeability values in the current research and the mentioned references is the horizontal permeability which was measured parallel to the bedding plane of the rock formations). Such permeability-porosity heterogeneity can result from a dynamic depositional origin, like braided-fluvial. The authors also emphasise the very high poro-perm values closer to the faults extending from *Gronau* (Gronau Fault Zone; (Duin et al., 2006)). These historic poro-perm measurements show that certain sections of the *Tubbergen* formation have poro-perm similar to existing Dutch geothermal doublets. However, the poro-perm variation becomes a geological risk for geothermal resource development (Veenstra et al., 2020).

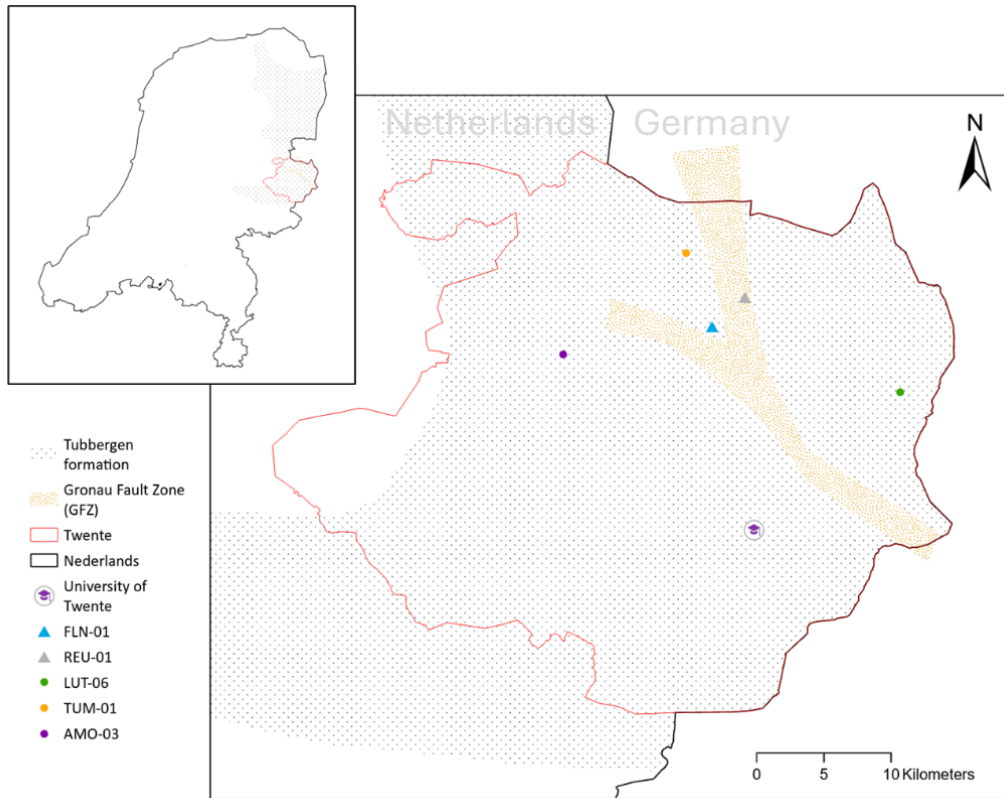


Figure 1.1: Lateral extension of the *Tubbergen* formation. The *Tubbergen* formation and Gronau Fault Zone are only indicated within the Netherlands. They do not indicate the actual geographical extent; they are only illustrated for visual interpretation. Modified after TNO-GDN (2024) and Veenstra et al. (2020).

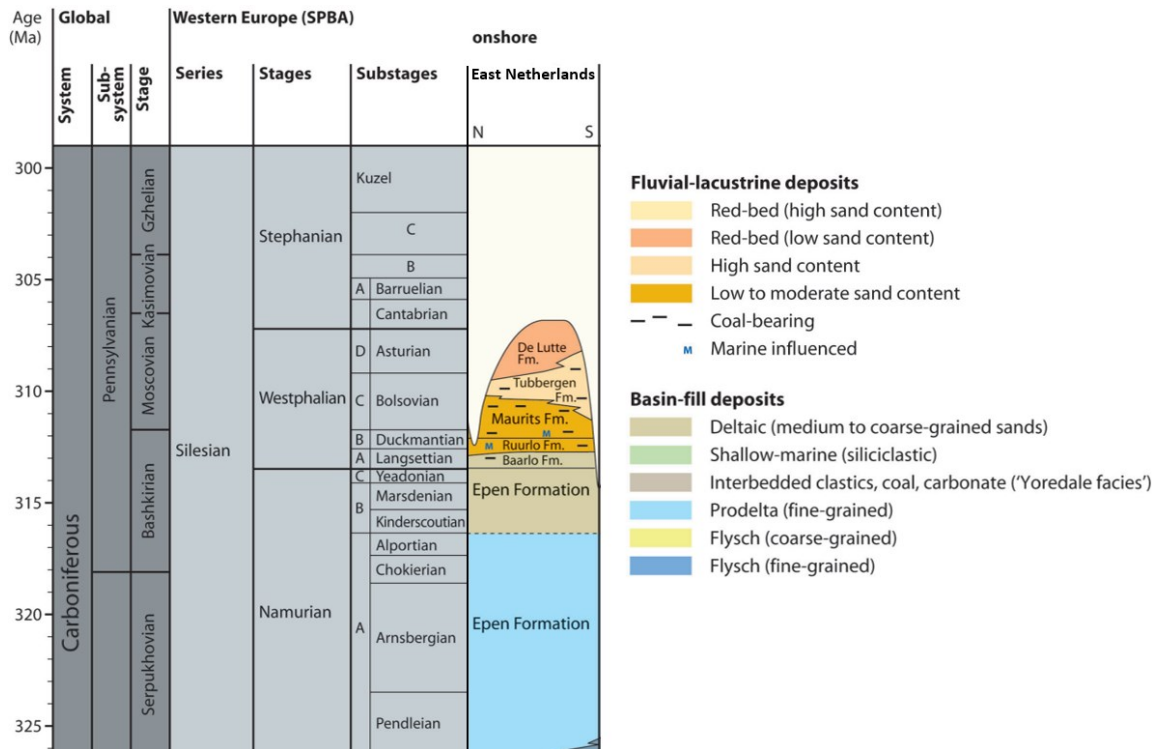


Figure 1.2: Chronostratigraphy of the *Tubbergen* formation, which is grouped in onshore fluvial-lacustrine deposits, overlaid by *De Lutte* formation and underlaid by the *Maurits* formation. Modified after NLOG, (2024).

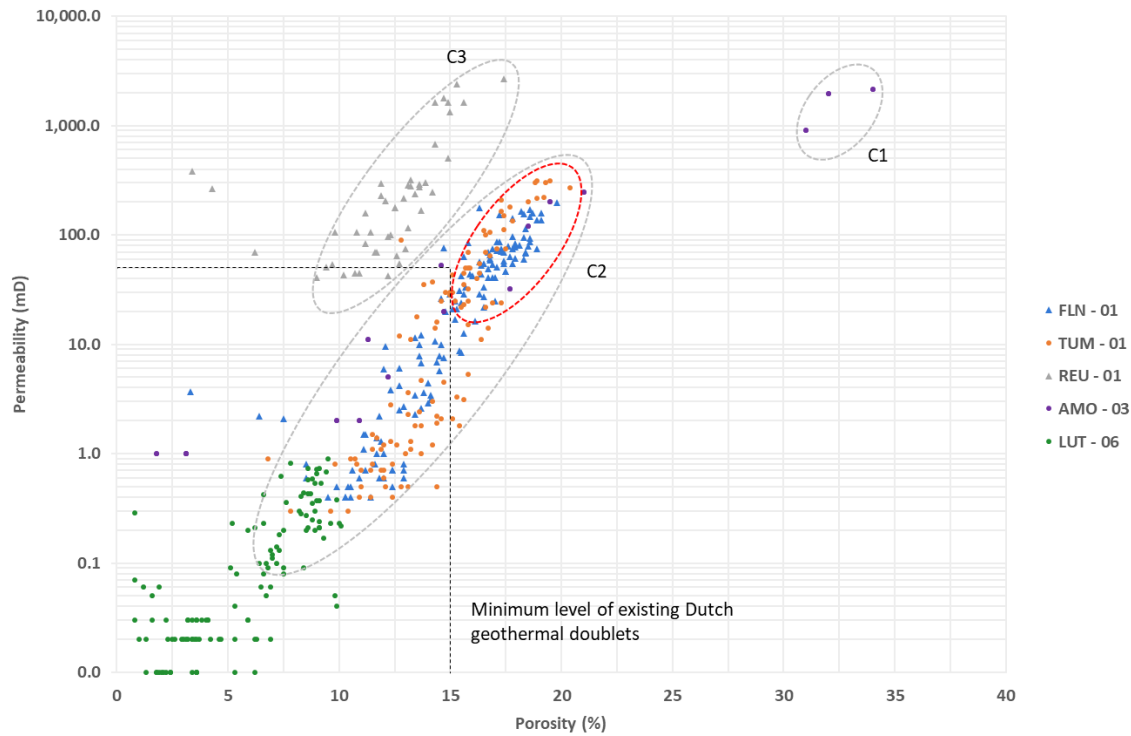


Figure 1.3: Porosity and permeability variation of *Tubbergen* sandstone in Twente from five drill holes: FLN – 01, TUM – 01, REU – 01, AMO – 03, and LUT – 06 (NLOG, 2023b). The *Tubbergen* formation is found at different levels between 1470 and 3193m depths. The sub-trend enclosed in a red ellipse shows the clean sandstone. REU-01 has higher permeabilities for lower porosities, and AMO-03 has high values for both porosity and permeability. C1, C2, and C3 clusters are demarcated to highlight the value variation. Modified after Veenstra et al. (2020).

## 1.2. Research Problem and Objectives

The strong poro-perm variations within historic plug measurements of the *Tubbergen* formation (Figure 1.3) pose a risk for geothermal realizations within the *Tubbergen* formation. Publicly available scientific information on the exact causes of poro-perm heterogeneity is scarce. Therefore, this research aims to reveal the mineralogical factors associated with the poro-perm variation in the *Tubbergen* formation by investigating historic core plugs with state-of-the-art imaging spectroscopy core scanning.

### 1.2.1. The main objective and the sub-objectives

To identify the mineralogical factors causing the porosity-permeability heterogeneity of the sandstone in the *Tubbergen* formation, using shortwave infrared hyperspectral spectroscopy.

- To identify the mineralogical factors that cause the porosity-permeability variation in *Tubbergen* sandstone core plugs.
- To identify the distribution patterns of mineralogy that affect the porosity-permeability in *Tubbergen* sandstone core plugs.

### 1.2.2. Research questions

- What mineralogical factors affect the porosity and permeability of sandstone from the *Tubbergen* formation?
- How does mineralogy distribution affect the porosity-permeability of the analyzed sandstone core plugs?
- What causes the higher permeability values in REU – 01 samples than FLN – 01 for the same porosity values?

## 2. RESEARCH DATA

Two types of data were used in the study. First is the porosity and permeability data of the *Tubbergen* formation from two drillholes. The second dataset is the SWIR data of the same drill core plugs on which the poro-perm was measured.

### 2.1. Porosity and Permeability Data

Poro-perm information is obtained from the two drill holes indicated in Figure 1.3, publicly available in NLOG (2023b). The two drill holes are FLN – 01 (FLN) and REU – 01 (REU), named after the region they were drilled. According to the details in Table 2.1, none of the drill holes penetrates the complete thickness of the *Tubbergen* formation. Even though the formation has more thickness in REU than in FLN, cored sections in REU are smaller than in FLN. Therefore, FLN has more core plugs with poro-perm values than REU. Additionally, on top of the *Tubbergen* formation in FLN, *De Lutte* formation is available with a 119m (1764 – 1883m) thickness where the whole section was cored, which the core-plugs also contain high poro-perm values, thus used in this research. The poro-perm analyses were compiled by the Dutch Petroleum Company (*Nederlandse Aardolie Maatschappij* - NAM).

Apart from the NAM’s poro-perm analysis, another poro-perm analysis report has been compiled by the Geological Laboratory of *C. Deilmann* mining company from Germany for a selected 61 FLN samples. The current study used only the data from the NAM report. The differences between the two datasets are given in chapter 4.1.

Table 2.1: A summary of the drill holes where the core plugs were obtained. The section that belongs to *De Lutte* formation is highlighted in grey.

Drill hole	Completion date	End depth (m)	Details of <i>Tubbergen</i> formation			Cored sections
			From (m)	To (m)	Thickness (m)	
FLN	21-Jan-1966	1968	1764	1883	117	All
			1883	1968	85	
REU	10-Apr-1970	2571	2213	2571	358	2250 - 2260 m
						2545 - 2555 m

### 2.2. SWIR Hyperspectral Data

To analyse the mineralogy of poro-perm variation using SWIR spectroscopy, the same samples used for measuring the poro-perm were obtained from the NAM core repository in *Assen*. 478 plugs are available for FLN. Most REU data points have two plugs representing each label; consequently, 209 plugs are available for 108 labels. All the plugs are cylindrical with a diameter of about 2.7cm (Figure 2.1). Several samples were distorted during the permeability measurements, as indicated in the original core analysis documents (NLOG, 2023b), and they only have porosity values. FLN plugs are about 1.5cm long, while REU plugs are slightly longer, about 1.9 cm. One face of the plugs is labelled for the respective data point. Therefore, unlabelled surfaces were scanned to avoid the spectra of label ink.

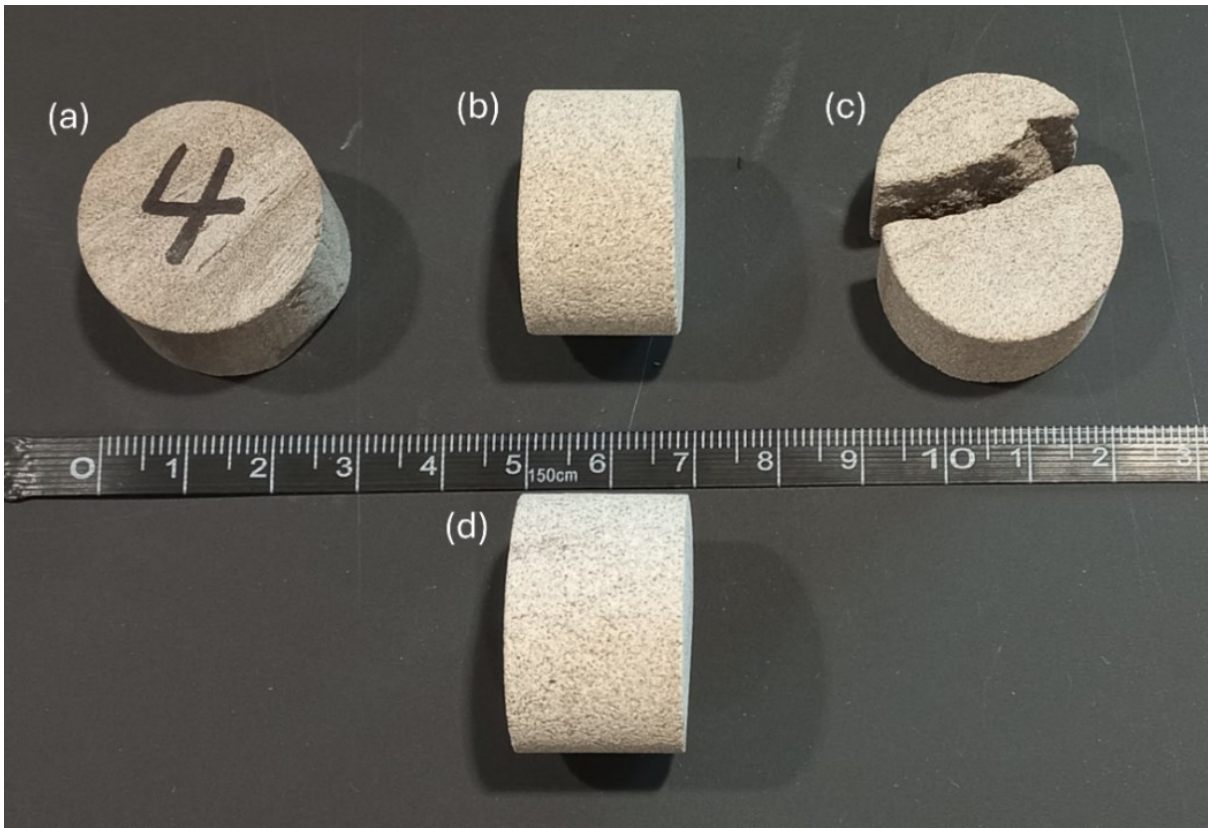


Figure 2.1: Four of the core plugs used in the research. (a) A plug from FLN on its vertical position with a labelled surface. (b) A plug from FLN on its horizontal position. (c) A disintegrated plug from FLN, which the permeability value is unavailable. (d) A plug from REU on its horizontal positions. Plugs from both drill holes are the same diameter, while the plug thickness of REU is higher than the FLN, as seen in (b) and (d).

### 3. RESEARCH METHODOLOGY

The chapter describes the procedures of arranging porosity-permeability data, SWIR data acquisition and preprocessing, and analysing the two data types to achieve the objectives. The analysis combined poro-perm data with SWIR spectral information to reveal the mineralogical factors affecting poro-perm variation.

#### 3.1. Porosity-Permeability Data Preparation

The poro-perm data from NAM are available as website text and as the scanned copy of the original report on NLOG (2023b). However, for the FLN, the website text only has 388 data points, whereas the scanned copy contains 478. The number of plugs physically available is 452, but labelling ended at 482, which means several samples are unavailable within the sequence. A reliable link between the samples and their respective poro-perm measurements is imperative for a valid result. Therefore, to avoid confusion, the poro-perm data table was sorted out by physically inspecting the plugs and comparing them with poro-perm values. Adjacent plugs with high and low permeability values were inspected with a hand lens to identify textural and mineralogical differences that can be related to corresponding values in the table. Also, plugs were visually compared with the slabbed drill-core photos (NLOG, 2023b) to check that the corresponding label and depth of plugs match the core slab's appearance (colour, textures) at the relevant depth. Also, disintegrated plugs should not have permeability values during the measurement, while they can have porosity values in the table. To check the labelling sequence, such plugs were compared against the data points indicated as "disintegrated samples" in the poro-perm table.

Additionally, poro-perm data from NAM and the German lab were compared to see if there are significant differences in all the values from two different measuring systems. Because direct

Also, it was indicated that the permeability of certain plugs was lower than the instrument's minimum measuring limit ( $<0.4$  mD). In reality, the permeability of such plugs can be varied between  $0 - 0.4$  mD. Thus, the mid value of the range, which is  $0.2$  mD, was used for the statistical analyses in the current study. Finally, the data table was modified to consider all the abovementioned differences to be used in the current research.

Poro-perm data of well REU did not have confusion with plug numbers and data points. It has labelled plugs from  $1 - 108$  without blanks. Similar to FLN, few disintegrated plugs during the permeability measurement have no permeability values and plugs with extremely low permeabilities are indicated as  $<0.4$  mD. Therefore, the only modification was assigning  $0.2$  mD to plugs with extremely low permeabilities. Since most of the REU data points have two plugs with the same label, both plugs were considered to have the same physical property value. Thus, both were considered for the study.

It is important to note that when comparing samples from the two datasets with similar poro-perm values, contrasting textural differences are seen, as in Figure 3.1. It is uncertain that the petrophysical properties were measured using the same techniques for several reasons (no mentions were found of the measuring techniques). Even though the poro-perm analyses used in the research were compiled by the NAM, the drill holes were made four years apart so that different techniques could have been used. If the same techniques have been used, various geological processes can cause different mineralogy/textures to produce similar poro-perm conditions. Therefore, FLN and REU data were analysed separately to avoid uncertainties.

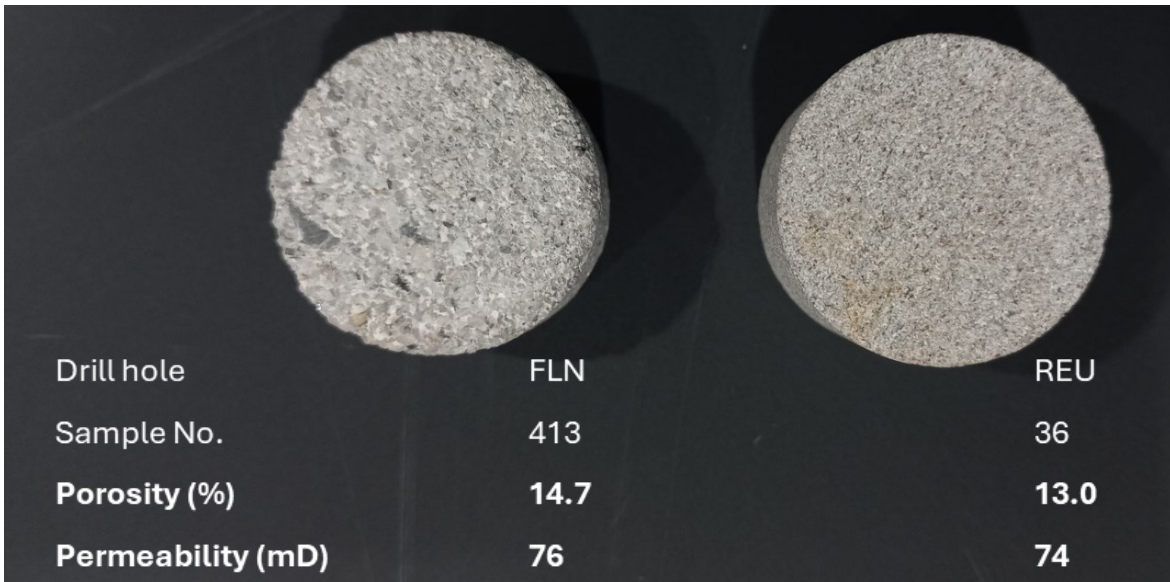


Figure 3.1: Textural comparison of two core plugs from FLN and REU with similar porosity and permeability. The FLN plug consists of loosely bound larger grains relative to the REU sample. REU consists of tightly arranged fine grains.

### 3.2. SWIR Imaging Spectroscopy of Drill Core Samples

In geology, the spectroscopy of minerals is studied using the visible to infrared (IR) wavelength range (0.4 - 14  $\mu\text{m}$ ) with a foundation laid by Hunt et al. (1970), where most minerals show diagnostic absorption and emission features in reflectance and emittance spectra, due to the different electron and molecular structure of the compounds (Hunt, 1977). Specific IR wavelength ranges are important when studying certain mineral groups. The main rock-forming minerals (detrital), such as quartz, feldspar, and micas, exhibit distinct characteristic features in the thermal IR (TIR) spectrum (Christensen et al., 2000). Similarly, clays and carbonates show features in the short-wave IR (SWIR) spectrum (Clark, 1999; Hunt, 1977). Minerals containing Fe display their unique features in the visible-near IR (VNIR) spectrum (Clark, 1999; Hunt, 1977). Since clays and carbonates are crucial mineralogies that affect sandstone porosity-permeability, SWIR spectroscopy was chosen to carry out the research.

Eventually, the spectroscopy method evolved to high-spectral resolution (hyperspectral) imaging (HSI) techniques. HSI is defined as image acquisition with hundreds (100 – 200) of contiguous and registered spectral bands where each image pixel has a radiance spectrum (Goetz et al., 1985; Lodhi et al., 2019). In other words, a 3D array (data cube) is generated by adding spectral information as a third dimension into a two-dimensional image. Consequently, HSI produces massive amounts of information, and the technique can be used in many subject domains, as in all remote sensing (RS) platforms, from spaceborne to laboratory scale. Mathieu et al. (2017) summarise the HSI applications in geology, particularly in analysing drill cores. Various instrumentation configurations have been developed to acquire data for rocks, drill cores, and chips at a laboratory scale (Okada, 2022). Additionally, many methods exist for the subsequent data processing (Asadzadeh & de Souza Filho, 2016).

Therefore, HSI is an ideal method for this research to analyse a large number of samples without any damage to archived samples such as drill core plugs.

#### 3.2.1. Acquisition of SWIR hyperspectral data

The drill core plugs were cleaned prior to scanning with compressed air to remove the dust and dirt. Cleaned samples were arranged on a plastic scanning tray, facing the labelled surface upwards. Plugs were placed into

two parallel columns beside the centre tray axis of the tray. Fragmented samples were put together at the fitting edges. A column is arranged in the ascending order of the sample label and photographed for future reference. Photographed plugs were flipped to face the unlabelled surface upwards without changing the relative position with each other, and a sample batch was ready to be scanned. Hyperspectral data of a prepared sample tray were acquired using the *Specim SisuROCK* VNIR & SWIR HSI system of ITC, University of Twente, with the instrument settings mentioned in Table 3.1. 14 scans were done to acquire the data for 691 plugs from both drill holes.

Table 3.1: Instrument configuration for HSI acquisition

Camera	VNIR	SWIR
Pixel size ( $\mu\text{m}$ )	128	258
Frame rate (Hz)	36.5	19.45
Exposure time (ms)	18	3.1
Scanning speed (mm/s)	5	
White ref. delay (mm/s)	10	7.5

### 3.2.2. Preprocessing of SWIR hyperspectral data

Acquired HS data was processed and analysed using the *Hyperspectral Python (HypPy)* package (Bakker, 2011) and *ENVI* software (Exelis Visual Information Solutions, Boulder, Colorado). SWIR raw data from the 14 scans were converted to 14 reflectance images, each with 288 spectral bands. Then, the images were left-right rotated/flipped because the sensor acquired the data as left-right flipped to the true appearance.

All the HS images were mosaiced together to create a single HS image. Noisy bands of the image mosaic, identified by the unrealistic reflectance values (reflectance below '0' or exceeding '1') in the image statistics, were removed from the edges of the spectral range by spectral sub-setting. Also, the statistics plot showed abrupt increases (spikes) on the "maximum" plot caused by the corrupt image pixels and needed to be removed before further processing. For convenient purposes, the statistics of individual images were examined for spikes, and few images had maximum plots with spikes, as in Figure 3.2. The band positions of the troughs and crests were noted, and the band math operator shown in Figure 3.2 was used to get the cumulative ratios between a crest and the associating trough. The band math operator generated a monochrome raster contrasting the corrupt pixels (bad pixels have higher values and are seen in brighter tones). The cumulative ratios enhance the effect of corrupt pixels rather than taking a single ratio. Identified corrupt pixels were masked on the relevant location on the image mosaic. Furthermore, the edges of the disintegrated samples and inked labels were also masked to prevent interferences with spectra analyses.

The reason for selecting a plastic tray as the background is because unique plastic absorption features (Figure 3.3) can be used to differentiate between the plugs and the tray with a band math operator. So, the background pixels can be removed conveniently. Four bands were selected empirically from the tray's plastic absorption features in reflectance spectra, and the band math operation was used to contrast the plastic and rocks (Figure 3.3) with a monochrome raster. Plastic pixels were highlighted using the threshold value 218 on the greyscale band and masked to preserve the rock pixels. An additional buffer zone of two pixels was removed inwards from existing sample boundaries to remove the remaining rock-plastic mixed pixels. At the end of the spatial sub-setting processes, the NaN (Not a Number) value was assigned to all the masked pixels. To complete the HS data preprocessing, the "Fast mean 1+5+1 neighbourhood" filter in HypPy was applied to smooth the image spectra.

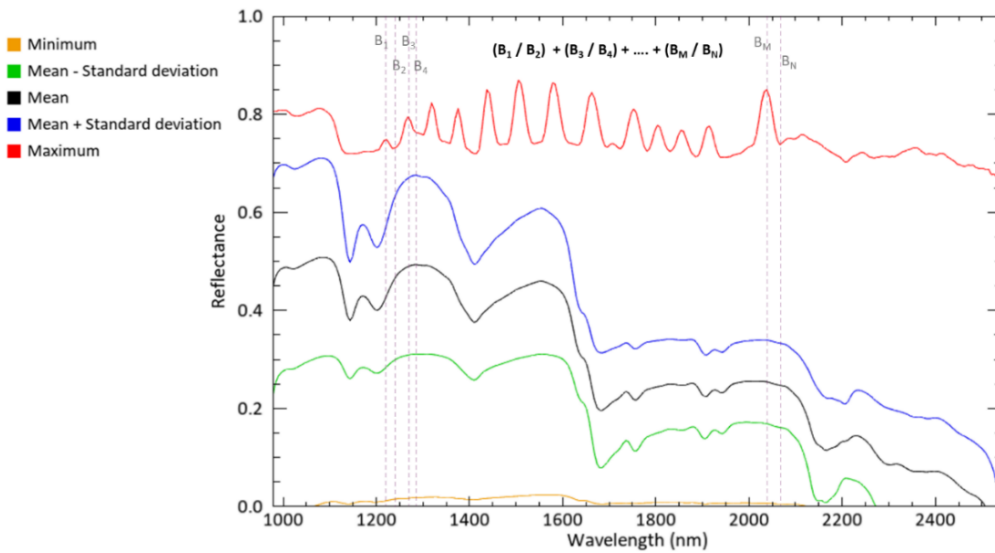


Figure 3.2: The statistics plot of a single reflectance image with corrupt pixels and the band math operator for highlighting the spike-causing pixels in the red-coloured "Maximum" plot. Wavelength positions of all the troughs and crests were included in the band math operation. The shape of the "Mean" resulted from the plastic spectra because plastic pixels are more abundant than rock pixels.

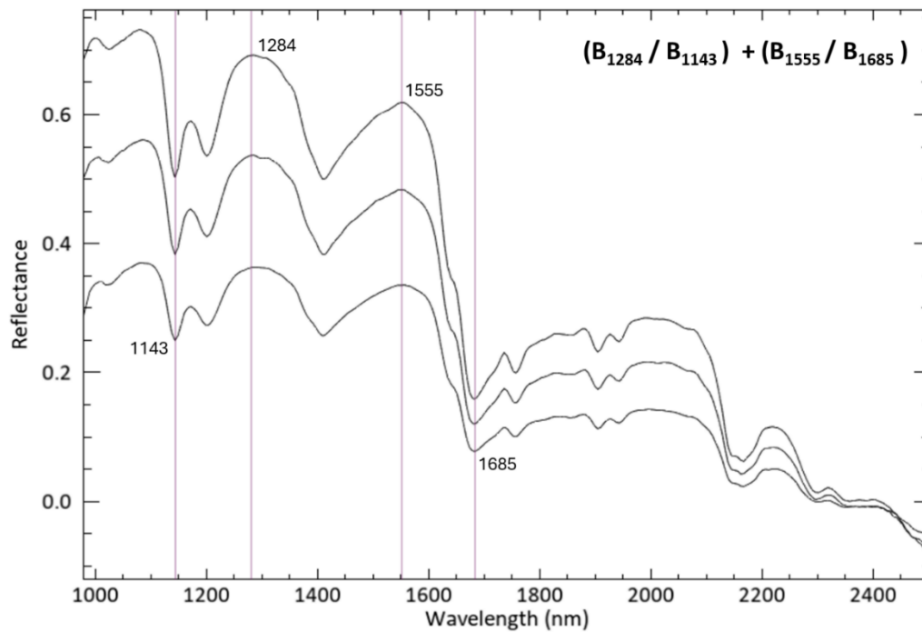


Figure 3.3: Three reflectance spectra of the plastic scanning tray and indicated wavelength positions for the band math operation highlighting plastic. The spectra with low reflectance are from the tray's plug shadows, and the highest albedo spectrum is from a tray pixel with no illumination barrier.

### 3.3. Identifying the Mineralogical Factors of Porosity-Permeability Variation

Principal Component Analysis (PCA) was used to derive spectral information of mineralogy from the hyperspectral image. Values of useful principal components were assigned to each sample and then used for statistical analysis with poro-perm data. PCA spectral indicators with clear relationships to poro-perm were explored empirically to recognize their mineralogy.

### 3.3.1. Principal component analysis of the SWIR hyperspectral image

PCA is a statistical method for transforming a larger number of correlated variables into a new set of uncorrelated variables called Principal Components (PCs) while retaining as much variation of the original data (Jolliffe, 1986). PCs are derived as linear combinations of the original variables (Ringnér, 2008) and are ordered so that the first few PCs retain most of the original variable variance (Hidalgo et al., 2021). In other words, PCs are obtained from the original data, where PC1 has the maximum variance from the original data, the next PC (PC2) has the maximum variance from the remaining data, and so on. Therefore, PCA is useful for dimensionality reduction in datasets with many interrelated variables.

HS images are also datasets with hundreds of correlated bands (Rodarmel & Shan, 2002), where the PCA becomes a useful data processing technique (Burger & Gowen, 2011) since certain bands do not contain useful information. PCA in HS images is used to obtain a new set of bands (PCs) where the first few PC bands contain sensible information. However, user input is required to define each piece of information (PC) meaningfully, such as mineralogy. The distinct absorption features and their characteristics are used to identify what contains each PC band that can be related to mineralogy (Asadzadeh & de Souza Filho, 2016).

PCA can compress the hyperspectral information from all pixels into fewer components (Hidalgo et al., 2021), where pixels with common spectral features can be identified as groups. The spectral and spatial behaviour of the groups can be analysed to understand the unique characteristics (spectral indicators) that define a group and how they are distributed across the samples. The individual spectral indicators (PCs) on samples can be obtained as a relative quantity for the considered PC and can be linked with its physical property values to find the correlation between mineralogy and poro-perm of sandstone plugs.

Two PCAs were done separately for the pre-processed image for FLN and REU core plugs. Because the two poro-perm datasets may not have been measured with similar techniques, and different geological processes may have influenced the two. Therefore, analysing both together can cause erroneous results.

The first PC bands from the two analysis results were empirically observed as greyscale/monochrome images to identify the decreased sensible information until the PC bands were seen as noisy images. The first 12 PC bands were decided to have useful spectral information. Then, RGB colour composites of different PC band combinations were created to visualise spectral patterns (compositional difference) on and across the samples.

### 3.3.2. Relationships between PC bands and porosity-permeability

As a preliminary qualitative analysis, different RGB colour composites of PC bands were compared with poro-perm values by placing them side-by-side to identify high-low zones of porosity and permeability in the colour composites. To make zones more evident, the samples of clearly identified colour groups in colour composites were indicated on the poro-perm scatterplots with similar representative colours, only using the plugs with homogenous colours.

Subsequently, a statistical approach was used to identify the connections between PCs and physical properties. The mean and standard deviation (SD) of PCs for each sample were calculated, and data tables were populated for every plug, including porosity, permeability, and PCs as attributes. The data tables were used to create scatterplots of PC mean SD against porosity permeability and to visualise the trends between physical properties and the individual PCs. Such trends can be interpreted to describe the relationships between physical properties and PC bands.

The samples with lower SD values (lowest 1/3) for a particular PC band were highlighted to extract more accurate insight from the scatterplots. Plugs with the lowest standard deviation for a given PC indicate the homogenous (low variability) samples for the PC, which can be considered as the representative for the PC. The poro-perm of such homogenous samples can be considered to correspond most closely to spectral indicators, showing the most accurate scatterplot trends.

PCs from the scatterplots that show interesting relationships (positive or negative trends) were further analysed. To identify the representative spectral information from a PC, spectra from the brightest and darkest pixels of PC band images were extracted. The two mean spectra of the 0.5 % brightest and darkest pixels from the monochrome PC image were compared against each other to identify the mineralogical information from a PC band. The pixels of the brightest 0.5% and the darkest 0.5% were obtained from the cumulative histogram of the PC pixel statistics.

The mean spectra were examined by focusing on absorption features in specific wavelength regions in the reflectance (and offset) and continuum-removed (and offset) spectra (Pontual et al., 1997c). The behaviour of the overall spectrum, shape, depth of the features, and reflectance were compared with USGS spectral library version 7 (Kokaly et al., 2017) to determine the mineralogy.

### 3.3.3. Relationships between band math-derived mineralogical components and porosity-permeability

A single PC band contains several spectral information, and different PC bands contain similar spectral features. Therefore, confusion may arise when determining the exact causes of poro-perm variations. Therefore, specific spectral mineralogical components observed in PC bands, such as albedo, Ferrous iron ( $\text{Fe}^{2+}$ ) response, mineral crystallinities and relative abundances, were separately calculated using band math operations (ratios and arithmetic operations of the reflectance values at defined wavelength bands) and absorption feature depth ratios to assess against porosity and permeability.

Albedo variation of the pixel spectra was visualised using the SWIR band 1600.72nm ( $B_{1600.72}$ ) because the wavelength position has the highest reflectance value due to the absence of absorption features on pixel spectra.

Kaolin-group minerals are 1:1 dioctahedral triclinic phyllosilicates (layer silicates) which are available in four polymorphs, namely halloysite, kaolinite, nacrite, and dickite. The polymorphs are ordered in the increasing structure of their crystal lattice. Differences in the crystal lattice are caused by the placement of vacant octahedral sites occupied by cations. The presence and absence of structural water change the interlayer spacing, causing variation in lattice order. The intensity of the kaolin-group mineral lattice is defined as the kaolinite crystallinity (KC) index. The KC variation is identified in SWIR spectroscopy by the intensity of the double absorption feature around 2200nm (Guatame-García et al., 2018; Pineau et al., 2022).

$\text{Fe}^{2+}$  response, which causes the tilt/drop/slope of the SWIR spectra observed within the wavelength range of 1300 – 1600nm, was determined using the  $R_{1600.72}/R_{1301.87}$  ratio (adopted from Pontual et al. (1997b)), where 'R' is the reflectance value of the mentioned wavelength positions.

Illite: kaolinite relative proportion was determined using the wavelength positions of the characteristic absorption feature of illite and kaolinite around 2200nm. An adopted band ratio of 2161.57nm and 2178.37nm wavelengths from Pontual et al. (1997b) was used to suit the relevant AIOH absorption feature positions from the dataset. The ratio is defined by dividing the shorter wavelength band (unique kandite group AIOH feature) by the longer wavelength band (common AIOH absorption of kandite and sericite).

Variation of illite : kaolinite relative proportion showed the presence of illite with clear absorption features. Therefore, illite spectral maturity (ISM) can also be a poro-perm influencing factor in *Tubbergen* sandstone. In SWIR spectroscopy, ISM variation is determined by the ratio between feature depths of AIOH around 2200nm and water around 1900nm (Zhou et al., 2022). Many published scientific literature used the term “illite crystallinity” (IC) for the depth ratio derived from reflectance spectroscopy. Doublier et al. (2010) discuss that the IC derived from reflectance spectra does not determine the actual crystallinity of the mineral and propose the term ISM instead. Therefore, the term ISM will be used instead of IC in this text. The ISM in image pixels were calculated by the feature depth ratio between the AIOH feature at 2206.38nm and the water feature at 1915.07nm, which was adopted from Pontual et al. (1997b) to suit the main AIOH

absorption feature position of illite in the dataset. Depths were calculated using continuum-removed spectra of the mosaic of pre-processed images.

Calculated parameter values for each sample were compared against porosity and permeability to reveal the relationships. The mean values of  $B_{1600.72}$ ,  $Fe^{2+}$  response, KC, illite : kaolinite relative proportions, and ISM were plotted against petrophysical properties, highlighting homogenous samples for the parameter (the lowest 1/3 after normalising the SD). This way, it can be visualized whether poro-perm has clearer relationships with the most representative samples for a considered spectral parameter, and it can be examined whether similar relationships to PC scatterplot are observed.

#### **3.3.4. Visualising the distribution of identified mineralogical parameters using linear spectral unmixing**

The spatial resolution limitations of sensors make it harder to identify very small individual objects such as mineral grains. Thus, an image pixel may cover multiple minerals at once, causing the pixel spectra to contain the spectral signatures of the minerals within its boundary. Therefore, the pixel must be “spectrally unmixed” to estimate the mineral constituents (all or some) in the pixel, which involves separating the pixels' spectrum into constituent spectra known as spectral endmembers and their fractional abundances per pixel. In linear spectral unmixing, it is assumed that the observed spectral signature of a pixel is a linear combination of the spectral signatures of the materials present in the considered pixel (Bioucas-Dias et al., 2012).

Identified mineral indicator spectra in PCA and band math operations for causing poro-perm variations were used as the endmembers to classify the SWIR image by linear unmixing. Unmixing results were shown as endmember colour composite to visualise their distribution across the analysed samples.

## 4. RESULTS

### 4.1. Rearranged Porosity-Permeability Data

The rearranged poro-perm data for FLN from the original Dutch report is given in Appendix 1. A comparison of values from the German and Dutch reports is shown in Figure 4.1. Two plots compare the porosity and permeability separately from both reports. The relative differences between the two sources can be seen with one-to-one reference lines in the plots. Values from the two reports are not identical in terms of both porosity and permeability. In the porosity plot, many values plotted below the one-to-one line indicate that the values from the Dutch report are higher than those from the German report. In the permeability plot, many values are plotted above the on-to-one line, indicating that many values from the Dutch report are lower than those from the German report. However, they are relatively comparable except for a few measurements that show a drastic variation from the trend.

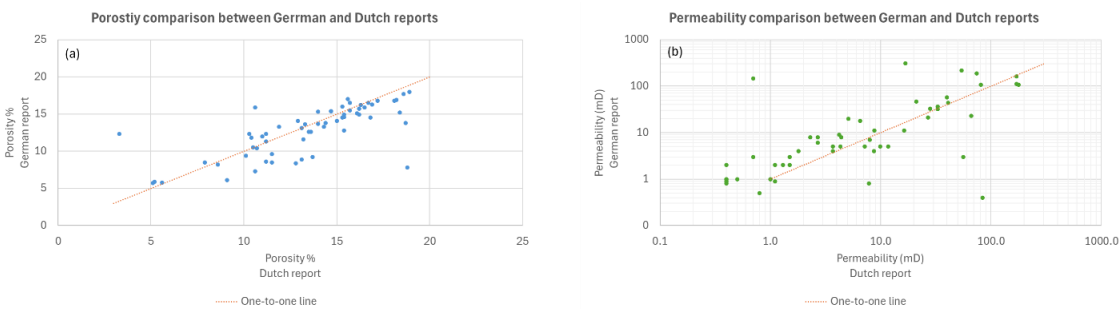


Figure 4.1: The comparison of two laboratory poro-perm analysis reports from Germany and the Netherlands for FLN. (a) Porosity comparison. (b) Permeability comparison. Tabular data for the two plots is given in Appendix 2

The poro-perm data for REU is given in Appendix 3.

### 4.2. Pre-processed SWIR Hyperspectral Data

Figure 4.2a shows an IR false colour composites of the raw reflectance HS data array. Removal of noise bands (Bands 1 – 8 and 283 – 288) reduced the original number of 288 bands to 274. The band math operator generated a monochrome image differentiating plastic and rock in light and dark pixels, respectively (Figure 4.2b). A cleaned image after removing all irrelevant pixels is shown in Figure 4.2c.

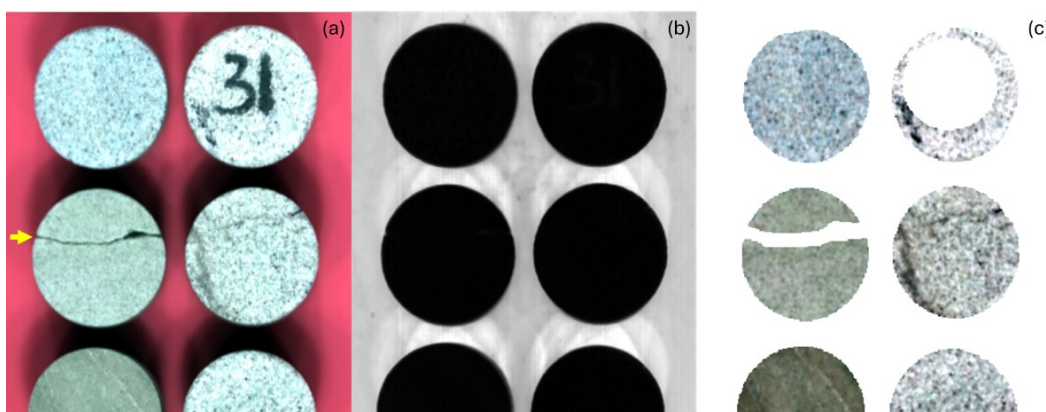


Figure 4.2: Preprocessing results of HS reflectance data (RGB of (a) and (c) are 1499.41 nm, 1752.41 nm, and 1943.09 nm). (a) Reflectance image from SWIR HS raw data. Yellow arrow indicates splitting of a core plug. The plastic is seen in reddish colour due to the false colour composite. (b) Monochrome image to differentiate plastic vs rocks. (c) Image after the preprocessing: pixels of plastic, labels, and splitting were removed.

The image statistics plot also shows no unusual spikes after completing preprocessing (Figure 4.3). Notable features are seen in the mean plots at 1400nm, 1900nm, and around 2200nm wavelengths, caused by the most abundant spectral features from all the remaining pre-processed image pixels (pixels of rock samples). The three features at the mentioned wavelength positions indicate the rich presence of hydroxyl (OH), water, and AlOH (Hunt, 1977; Hunt et al., 1970) molecules within the sample constituents.

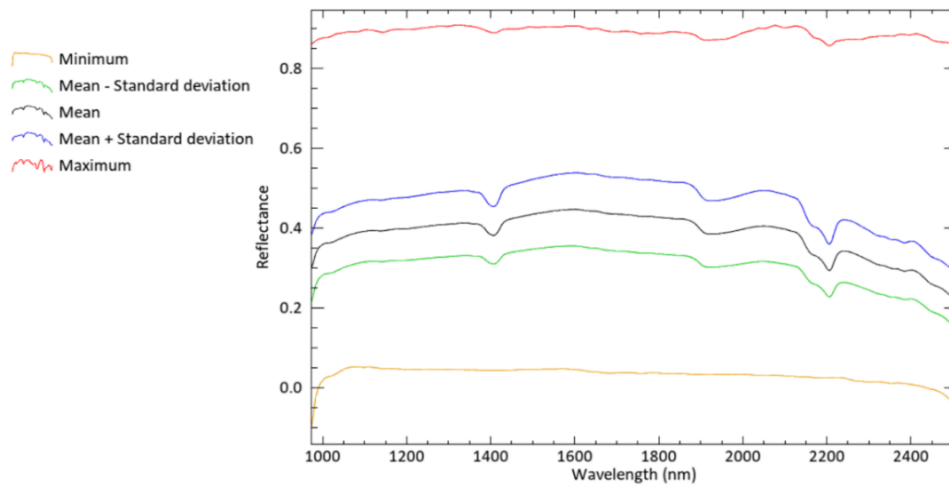


Figure 4.3: The statistics plot of the pre-processed HS image mosaic. Note the disappearances of spikes in the “max” plot and the shapes of plastic spectra after the preprocessing when compared with Figure 3.2. Absorption features from the dominant constituents from the rock pixels at 2200nm, 1900nm, and 1400nm wavelengths can be seen in mean plots.

After completing the basic image preprocessing, the image had to be further processed to remove the noise in pixel spectra, and the “Fast mean 1+5+1 neighbourhood filter” (in HypPy) was applied. Figure 4.4 shows filtering effects on an image pixel, suppressing the noise.

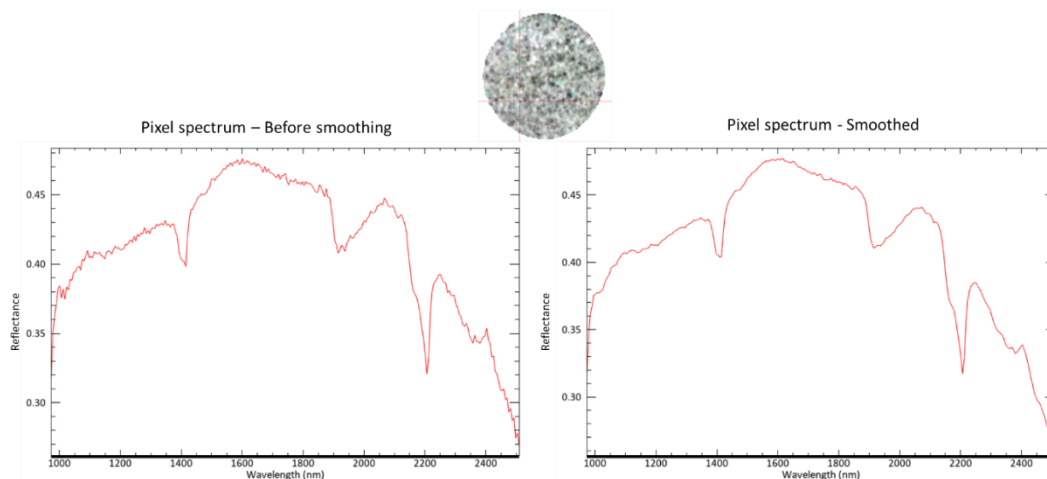


Figure 4.4: Comparison of two spectral profiles of the same rock pixel before and after the “Fast mean 1+5+1 neighbourhood” smoothing filter. Small wiggles in the left spectrum have disappeared in the right spectrum after filtering.

Several image pixels from clastic minerals, such as quartz and feldspar, show some of the plastic tray’s absorption features in their spectra, similar to Figure 4.5:.

The preliminary observation after the preprocessing shows that image pixels are heavily dominated by kaolinite features and, to a much lesser extent, with illite/sericite. Carbonate features and Fe<sup>2+</sup> reponse are also indicated in pixels. Example spectra observed in the image are shown in Figure 4.6.

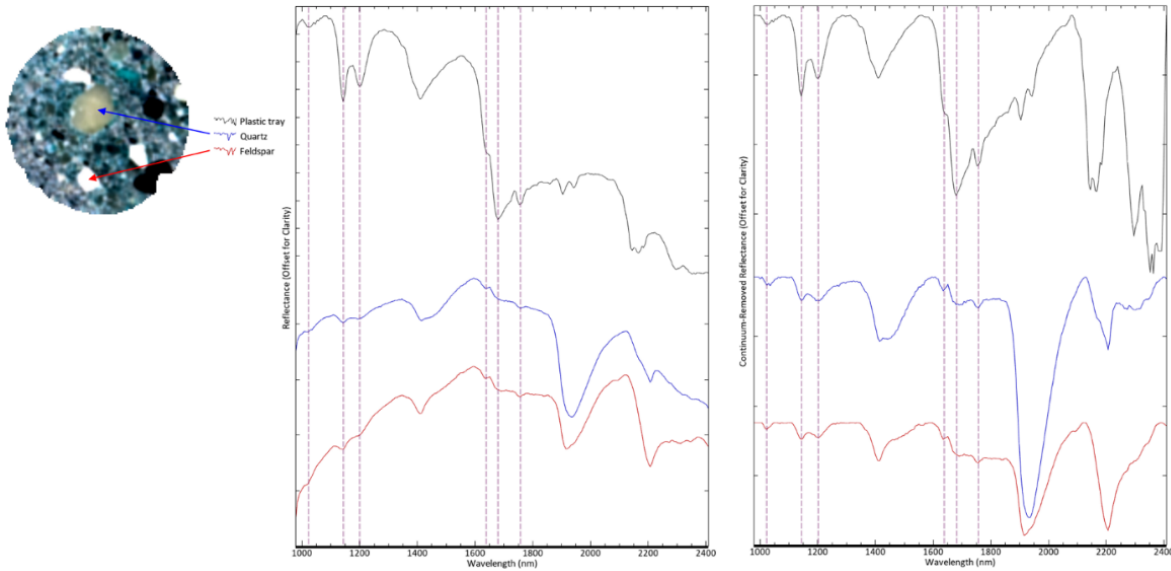


Figure 4.5: An example of pixel spectra from quartz (in blue) and feldspar (in orange) clasts containing absorption features similar to plastic trays. The plastic spectrum is indicated in black colour. Plastic absorption feature positions, seen in quartz and feldspar, are indicated by dashed lines.

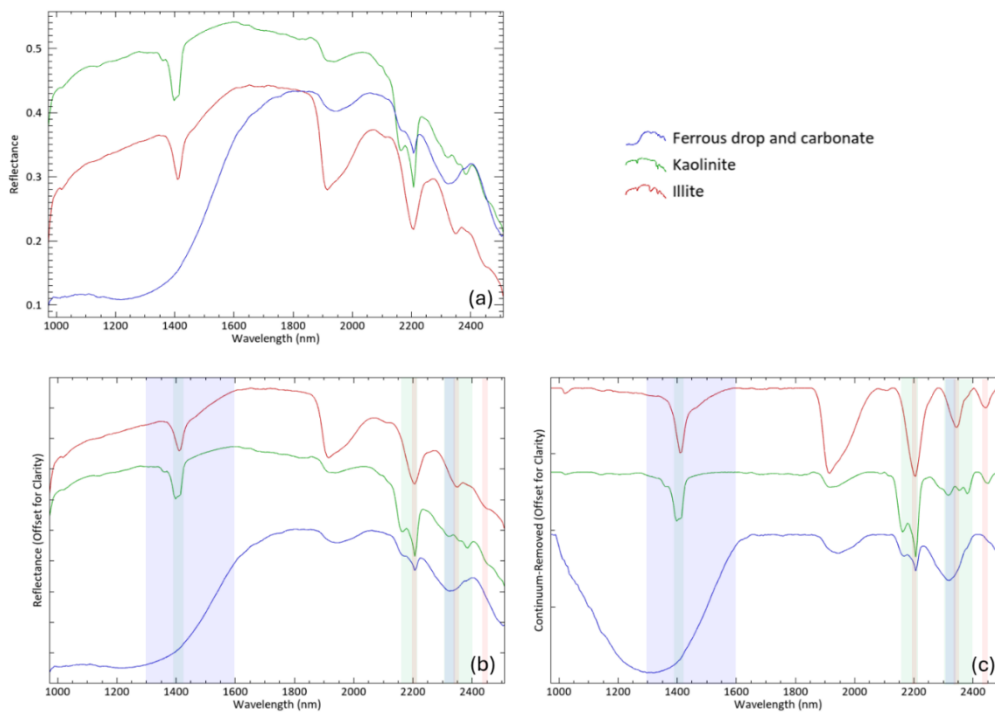


Figure 4.6: Example spectra from minerals observed in the SWIR image. Characteristic wavelength ranges are highlighted in the same colour as in mineral spectra on the offset profiles. (a) Reflectance spectral profiles. (b) Offset reflectance profiles. (c) Continuum-removed offset reflectance profiles. Note that the broad feature of ferrous drop (blue spectrum) on the continuum-removed profile is not an actual absorption feature but an effect of hull-removal of the spectrum (Pontual et al., 1997c).

### 4.3. PCA results of SWIR Image

PCA statistics of the first 13 principal components of FLN and REU are given in Table 4.1 and Table 4.2. Note that the first PC band from both sets consists of more than 93% of the total variance SWIR hyperspectral data. The first 3 PC bands possess over 99% of the total data variance in both sets.

Table 4.1: PCA Statistics of the first 12 principal components of FLN and the scree plot of eigen values.

PC band	Eigenvalue	Cum. %
1	1.71517	93.67%
2	0.068928	97.44%
3	0.041085	99.68%
4	0.002056	99.79%
5	0.001534	99.88%
6	0.000842	99.92%
7	0.000368	99.94%
8	0.000183	99.95%
9	0.000163	99.96%
10	0.000118	99.97%
11	0.000105	99.97%
12	0.000049	99.98%

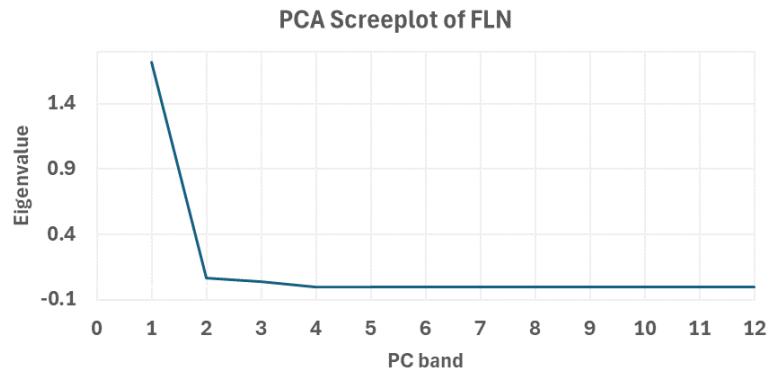
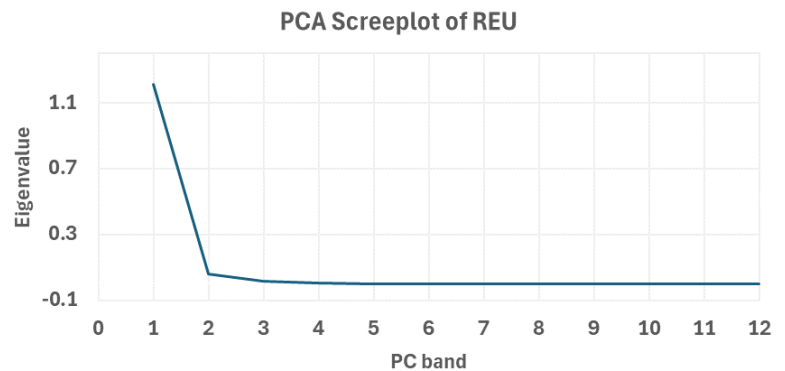


Table 4.2: PCA Statistics of the first 12 principal components of REU and the scree plot of eigen values.

PC band	Eigenvalue	Cum. %
1	1.213847	93.49%
2	0.06148	98.23%
3	0.017047	99.54%
4	0.002681	99.74%
5	0.00118	99.84%
6	0.000737	99.89%
7	0.000325	99.92%
8	0.000185	99.93%
9	0.000164	99.94%
10	0.000112	99.95%
11	0.000091	99.96%
12	0.000064	99.96%



The RGB colour composites of the first three PC bands from FLN and REU are shown in Figure 4.7 and Figure 4.8, respectively. For both datasets, PC3, PC2, and PC1 are assigned as red, green, and blue, respectively. The sample arrangement with labels is shown adjacent to each colour composite. The sample pixels exhibit the colours according to the proportions of constituent PCs. The relative proportions of constituent PCs of a sample pixel can be determined by referring to the pixel colour in the RGB legend. For an example, purple pixels resulted by the combination of blue (PC1) and red (PC2). Pink is seen if the red is more abundant than blue. If pixels seen in with a brightness close to white, they are most likely enriched with all the three PCs. Vice versa, pixels are seen in reduced brightness (black).

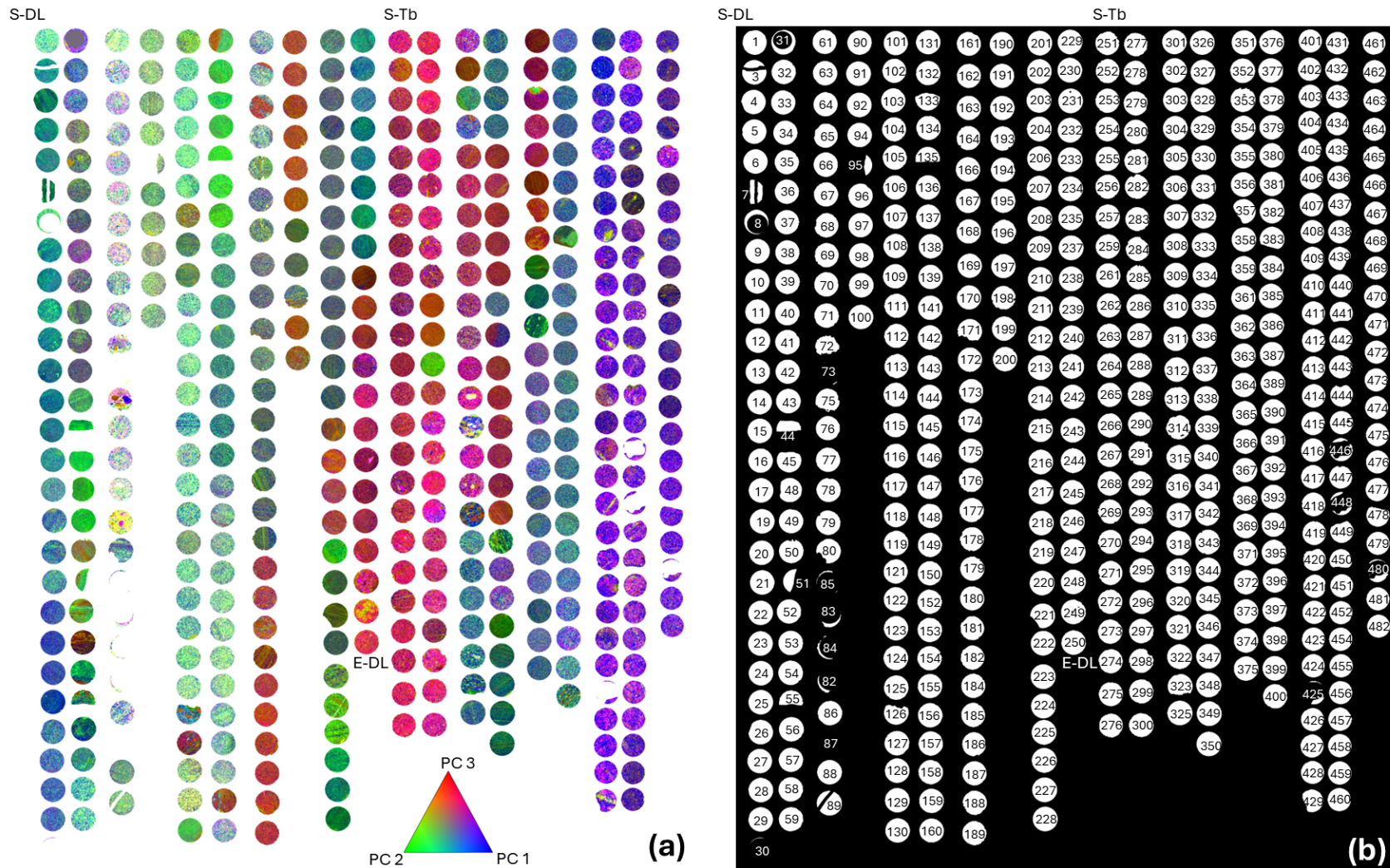


Figure 4.7: (a) RGB colour composite of the PC bands 3, 2, and 1 for FLN, showing the variations across the samples with the constituent PCs. (b) Labelled plugs in Figure 11a. The samples are organized in a downhole direction, going from top to bottom and then left to right. White areas are identical to the plugs in the left figure, and the black area is the masked pixels. Some plugs are incomplete (due to masking of sample number pen markings), so their labels are in white font. The Beginning of *De Lutte* formation is indicated as S-DL and the ending as E-DL. The beginning of the *Tubbergen* formation is indicated as S-Tb.

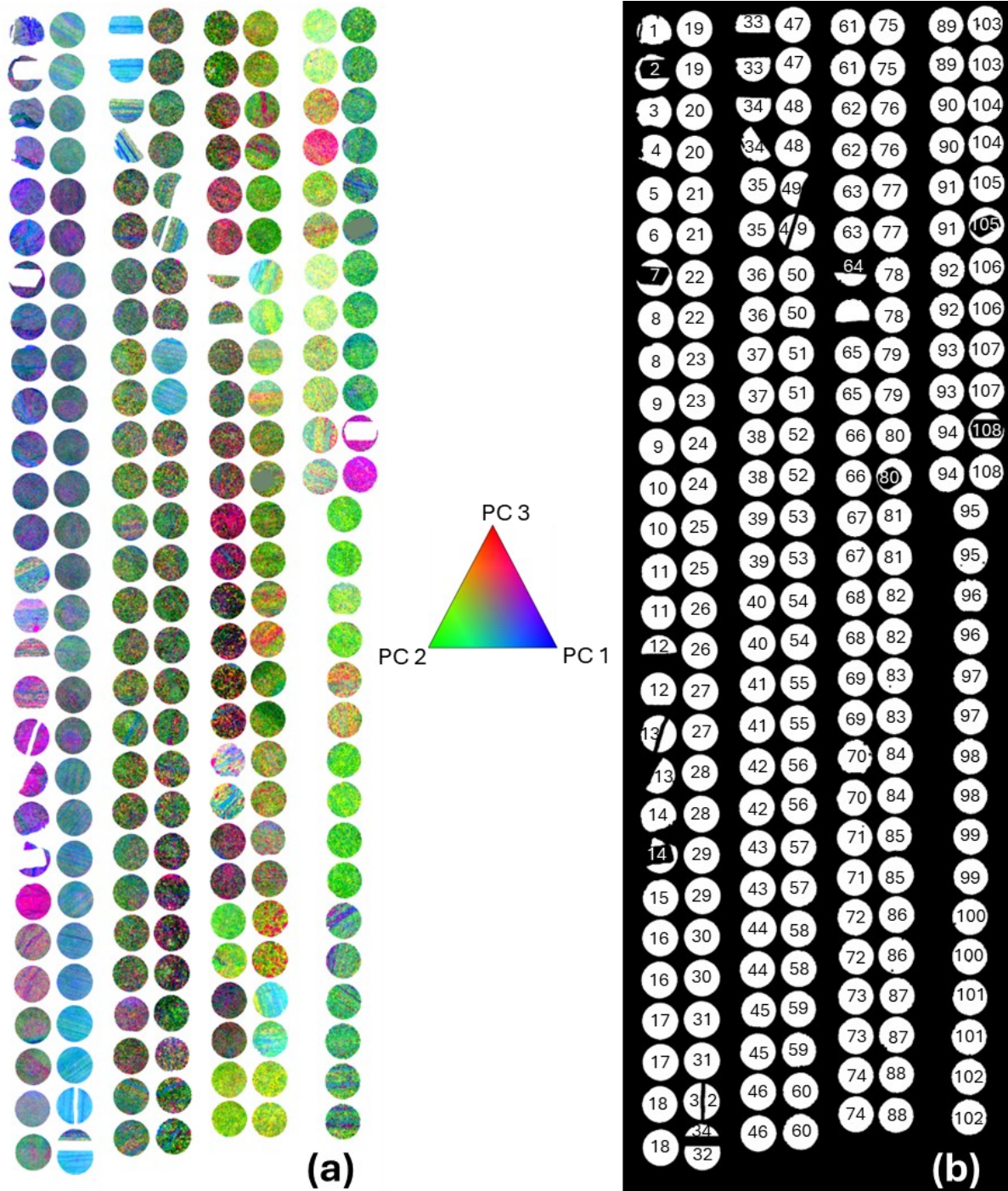


Figure 4.8: (a) RGB colour composite of the PC bands 3, 2, and 1 for REU, showing the variations across the samples with the constituent PCs. (b) Labelled plugs in Figure 12a. The samples are organized in a downhole direction, going from top to bottom and then left to right. White areas are identical to the plugs in the left figure, and the black area is the masked pixels. Some plugs are incomplete (due to masking of sample number pen markings), so their labels are in white font.

Figure 4.9 shows the coloured poro-perm plot of FLN by assigning similar representative colours to the samples from the PC colour composite in Figure 4.7. Data points are concentrated into three zones. Purple (blue/PC1 and red/PC2) and yellow (representing the samples with all three PCs) points occupy higher

poro-perm regions. The sharp bottom line consists of points with green varieties dominating PC2 (all the points in the line have a permeability value of 0.2mD). The data point group between the bottom line and high poro-perm group consists of all three PCs, orange, greenish, and dark purple, with varying proportions.

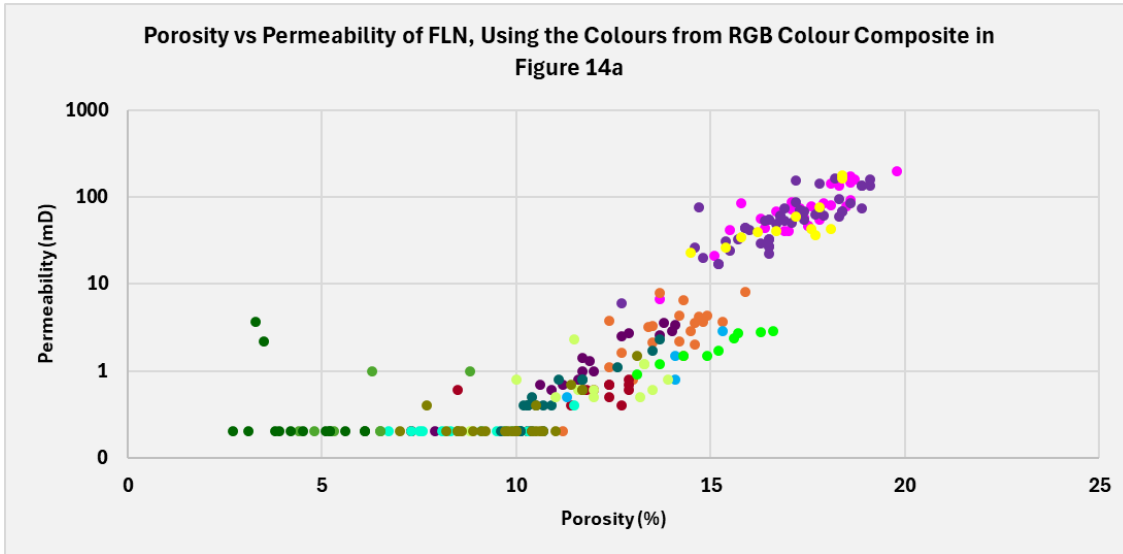


Figure 4.9: Porosity vs permeability plot of FLN with the colours from PCA colour composite in Figure 4.7, assigned to corresponding samples. Data point colours were chosen to represent the colours from PCA colour composite. Data points in the sharp horizontal bottom line are the 0.2 mD permeability samples (These samples do not have a permeability value in the original report since the minimum permeability measurement is 0.4 mD).

Figure 4.10 shows the coloured poro-perm plot of REU by assigning similar representative colours to the samples from the PC colour composite in Figure 4.8. Data points are mainly concentrated in two zones. Purple (blue/PC1 and red/PC2) points occupy higher poro-perm regions. The sharp bottom line consists of points with green (PC2) and blue varieties (all the points in the line have the permeability value of 0.2mD).

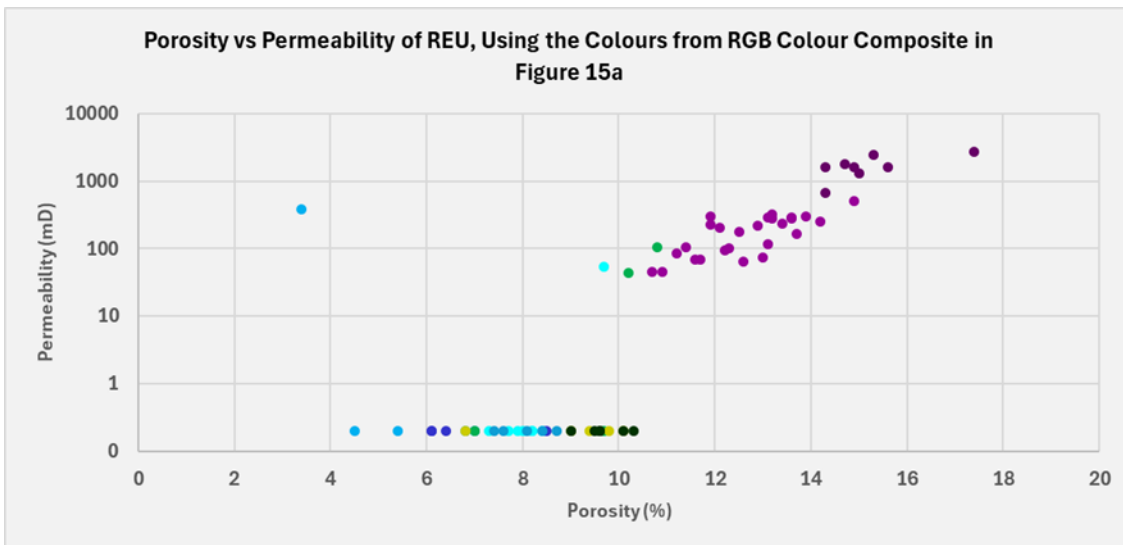


Figure 4.10: Porosity vs permeability plot of REU with the colours from PCA colour composite in Figure 4.8, assigned to corresponding samples. Data point colours were chosen to represent the colours from PCA colour composite. Data points in the sharp horizontal bottom line are the 0.2 mD permeability samples (These samples do not have a permeability value in the original report since the minimum permeability measurement is 0.4 mD).

#### 4.4. Relationships between PC Bands and Porosity-Permeability

A scatterplot series of the PC mean value of each plug against the porosity and permeability was created for the first twelve PC bands to identify the spectral indicators that change with porosity and permeability. For each plot, all the available data points are shown in blue, and the most homogenous samples (the sample with the lowest 1/3 SD for the PC) are shown in orange. The linear trend for the orange data points is also indicated in the same colour.

From the porosity vs mean PC plots of FLN in Figure 4.11, it can be identified that PC bands 1, 3, and 5 exhibit a positive relationship with porosity, while PC band 2 shows a negative trend. Permeability vs mean PC plots from FLN samples in Figure 4.12 do not show a clear relationship.

The REU plots of the porosity vs mean PC in Figure 4.13 show PC bands 1 and 2 exhibiting a negative relationship with porosity, while PC band 8 shows a positive trend. Similar to FLN, permeability does not show a clear relationship with mean PC values from any of the PC bands in Figure 4.14.

Additionally, another series of scatterplots were created with the PC standard deviation (SD) of each plug against the porosity and permeability to visualise the behaviour of physical properties with the spread of each PC band information. In the porosity vs PC SD plots of FLN (Appendix 4), a positive trend exists in every plot except for PC2, PC6, and PC7. The porosity shows clear positive curvilinear trends with PC1, PC3, PC8, PC9 and PC11, where the initial increase of SD leads to a rapid increase of porosity, which later stabilizes. PC5, PC10, and PC12 also show similar shape in trend but more intense.

Permeability vs PC SD plots of FLN (Appendix 5) shows clear positive trends with a weak correlation in PC1, PC3, PC8, PC9, PC10, PC11, and PC12. The rest of the PCs do not have an identifiable relationship with permeability.

All REU porosity and permeability plots with PC SD (Appendix 6 and Appendix 7) have recognisable positive trends. They all appear as linear trends with varying correlations.

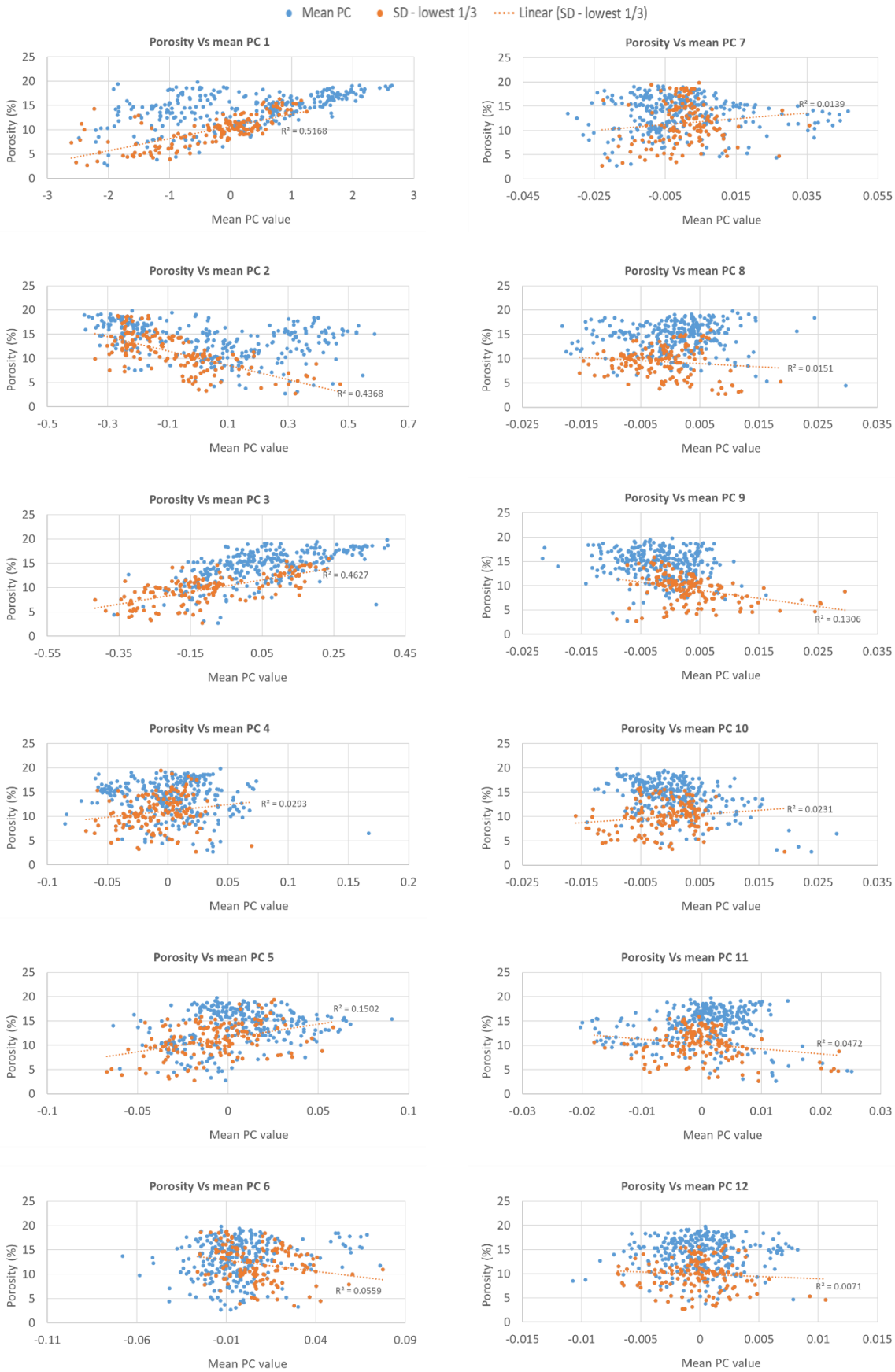


Figure 4.11: Scatterplots of mean PC vs porosity for the FLN - 01. Blue points represent the mean PC value of each core plug and their measured porosities. Orange points denote only the most homogenous samples for the PC (1/3 of core plugs with the lowest SD).

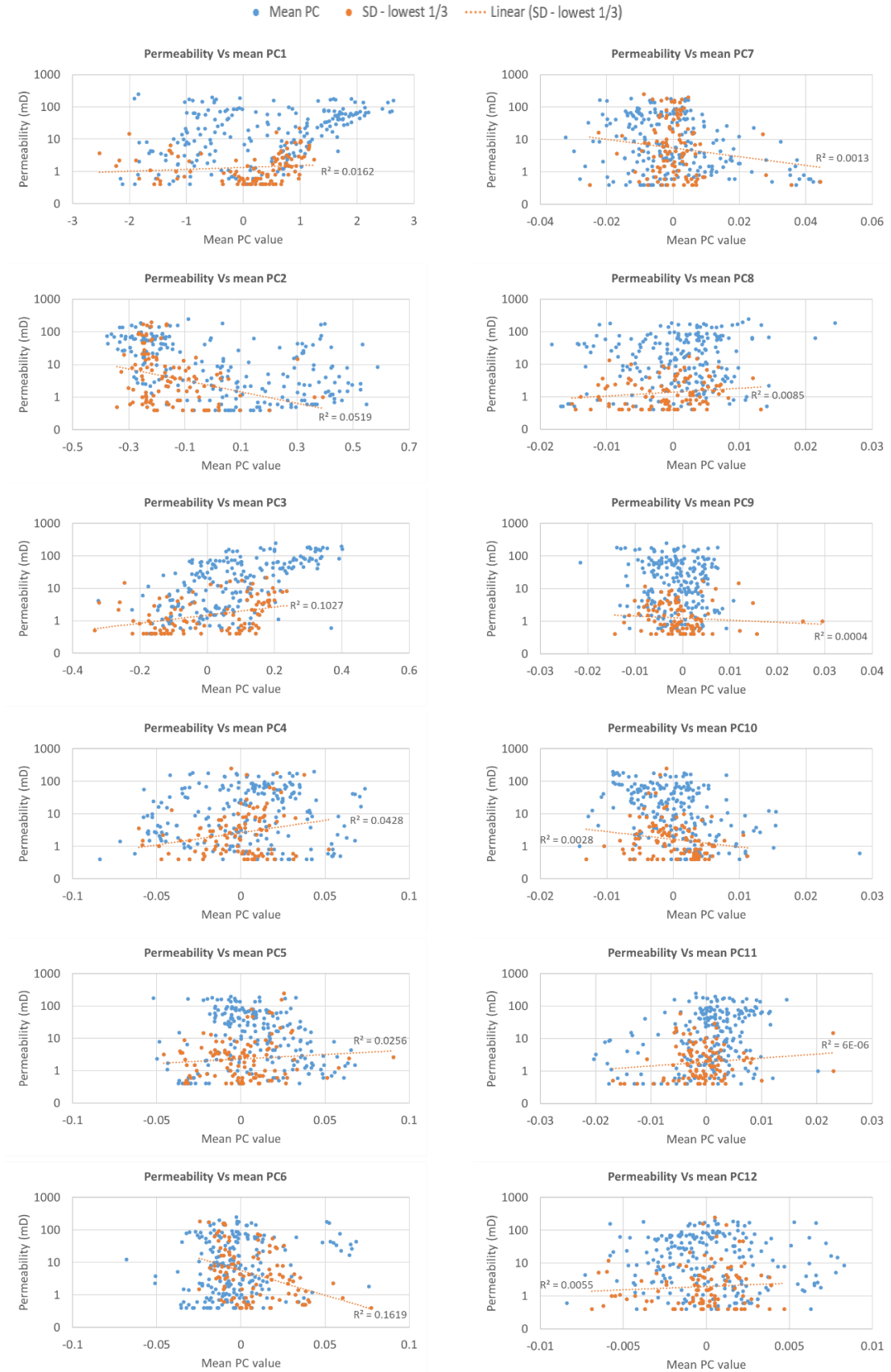


Figure 4.12: Scatterplots of mean PC vs permeability for the FLN - 01. Blue points represent the mean PC value of each core plug and their measured porosities. Orange points denote only the most homogenous samples for the PC (1/3 of core plugs with the lowest SD).

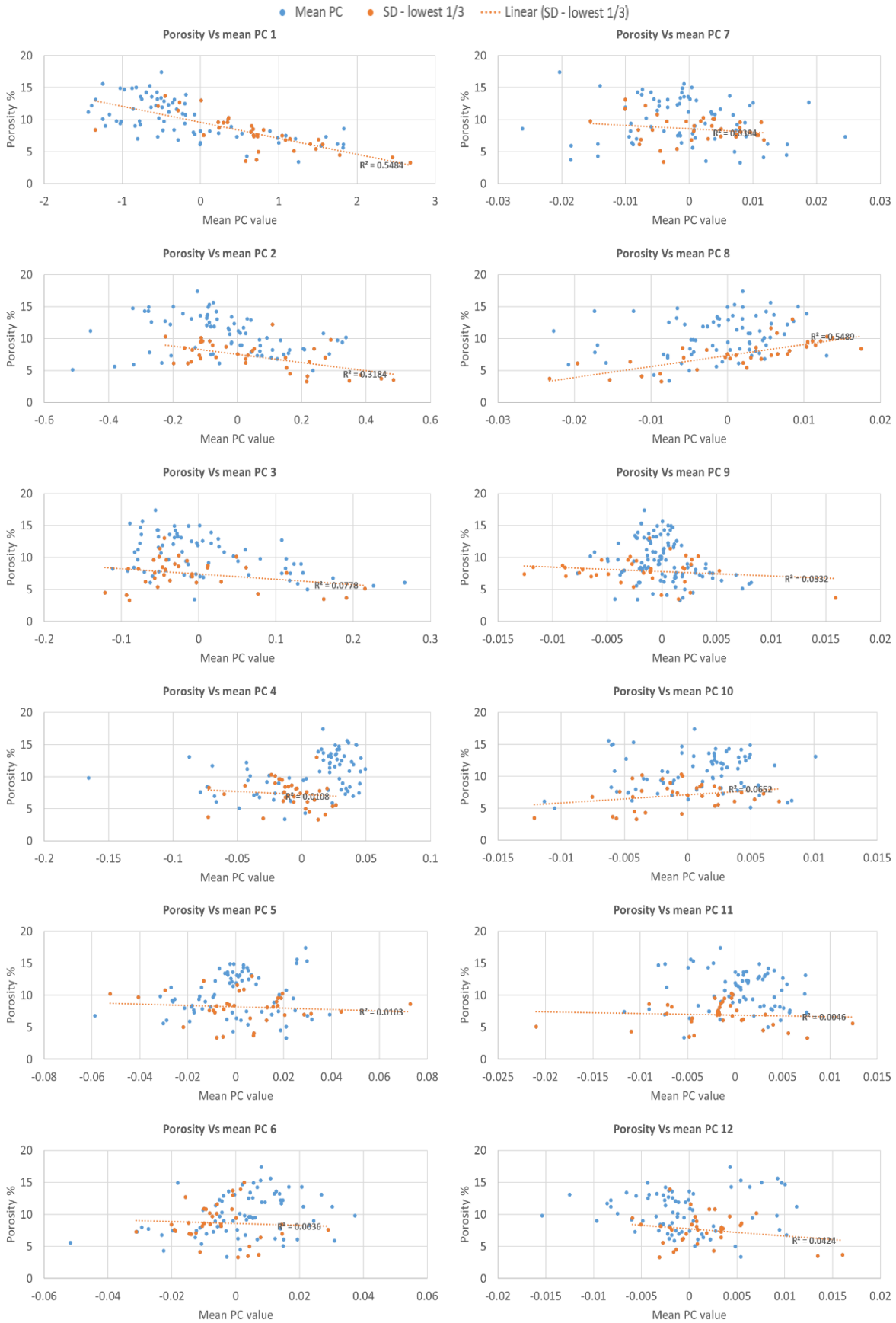


Figure 4.13: Scatterplots of mean PC vs porosity for the REU. Blue points represent the mean PC value of each core plug and their measured porosities. Orange points denote only the most homogenous samples for the PC (1/3 of core plugs with the lowest SD).

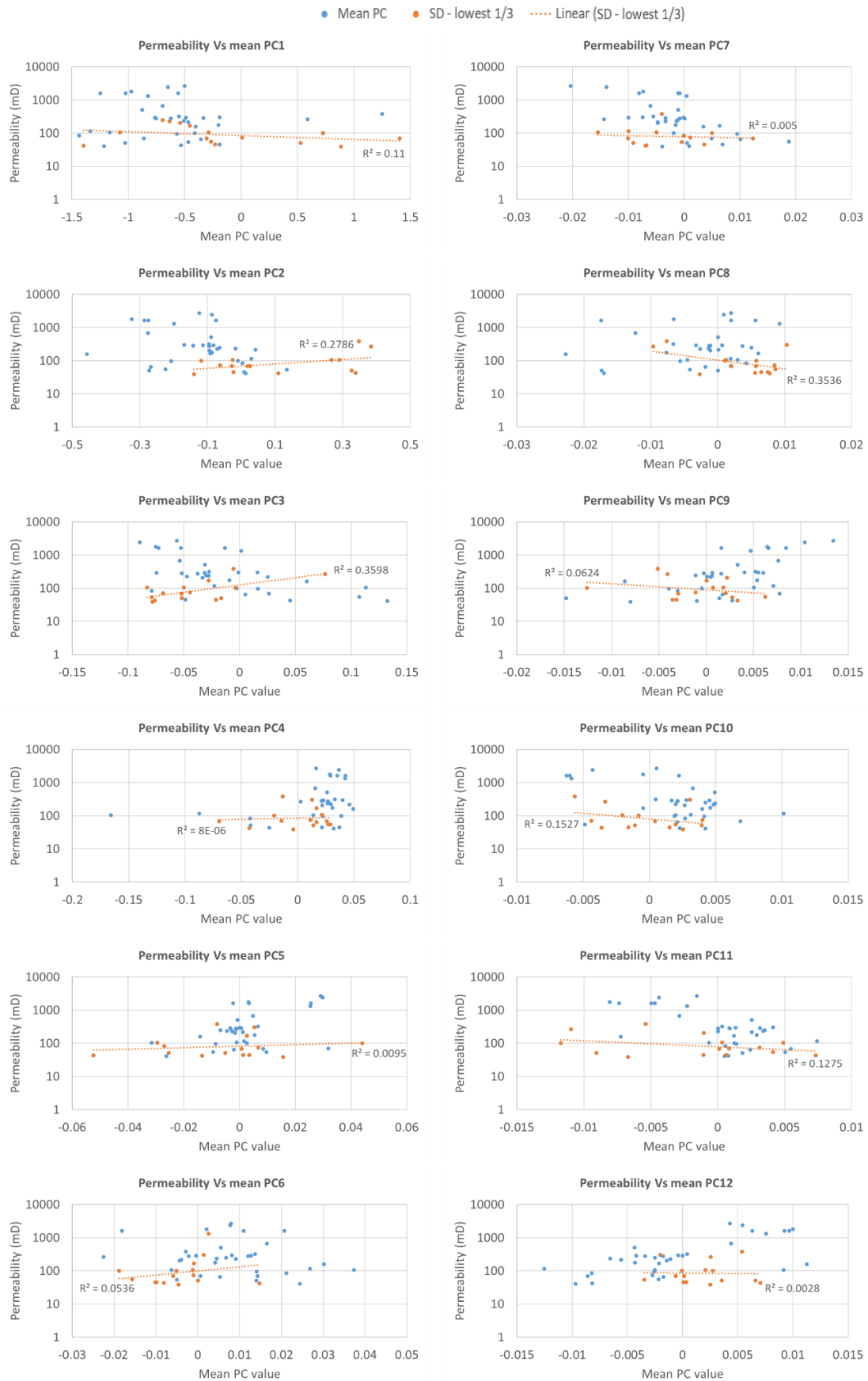


Figure 4.14: Scatterplots of mean PC vs permeability for the REU. Blue points represent the mean PC value of each core plug and their measured porosities. Orange points denote only the most homogenous samples for the PC (1/3 of core plugs with the lowest SD).

#### 4.5. Determining the Spectral Information of PC Bands

The distinctive spectral information from PC bands was identified by comparing the mean spectra of 0.5% of the brightest and the darkest pixels for a considered PC band. 0.5% of FLN pixels account for 17,303 pixels out of the 3,460,660 total pixels. From REU, it accounts for 7969 pixels out of the 1,593,864 total pixels.

##### 4.5.1. Analysis of FLN PC bands

Figure 4.15 shows the mean brightest and darkest spectra of FLN PC1. The two mean spectra have a contrasting difference in albedo, where the mean brightest spectrum shows the highest albedo, and the mean darkest spectrum shows the lowest albedo. Both spectra show characteristic kaolinite doublet features around 1400nm and 2200nm wavelengths.

Figure 4.16 shows the mean brightest and darkest spectra of FLN PC2. The two mean spectra have a contrasting difference in spectral profile slope before 1600nm wavelength, where the mean brightest spectrum does show a slope, while the mean darkest spectrum does not show slope. Other significant observations are dark spectrum shows clear characteristic kaolinite triple absorption features around 2350nm while the bright spectrum shows faded triple features with a single carbonate feature around 2323nm.

Figure 4.17 shows the mean brightest and darkest spectra of FLN PC3. The two mean spectra show contrasting differences in absorption feature depths and intensities. However, both spectra show characteristic kaolinite features. Mean brightest spectrum has shallow feature depths and low intensities relative to the mean darkest spectrum.

Figure 4.18 shows the mean brightest and darkest spectra of FLN PC5. The two mean spectra have a contrasting difference in absorption feature intensities. Both spectra show characteristic kaolinite features, while mean brightest spectrum shows clear strong absorption features relative to the mean darkest spectrum.

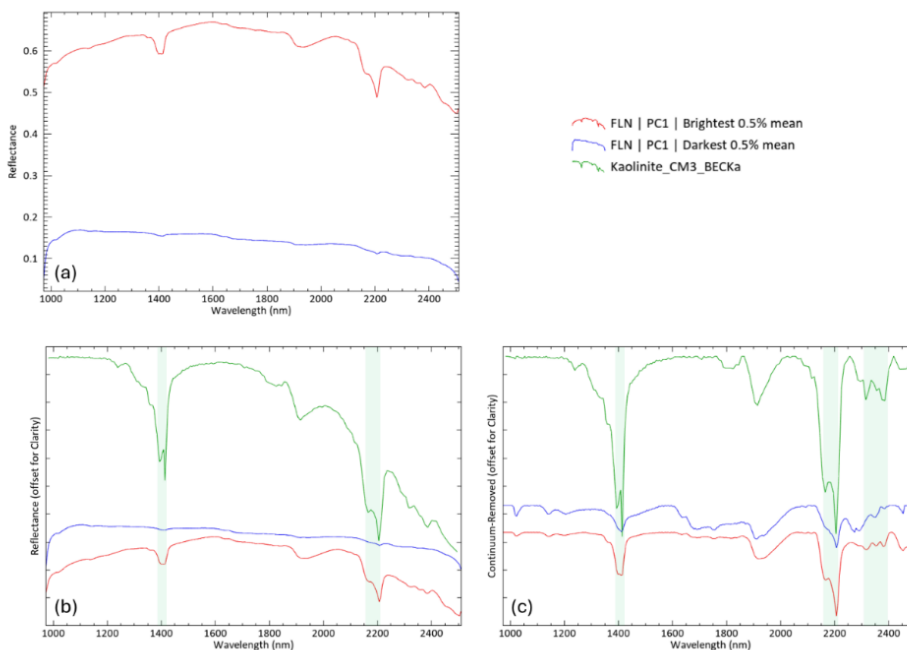


Figure 4.15: Comparing 0.5% of the brightest (red) and darkest (blue) mean spectra of the PC1 band from FLN. (a) Reflectance spectral profiles. (b) Offset reflectance spectral profiles. (c) Continuum-removed offset spectral profiles. Characteristic absorption wavelength ranges of the kaolinite reference spectrum (Kokaly et al., 2017) are indicated with the same profile colour on offset spectral plots to distinguish the feature position on mean spectra.

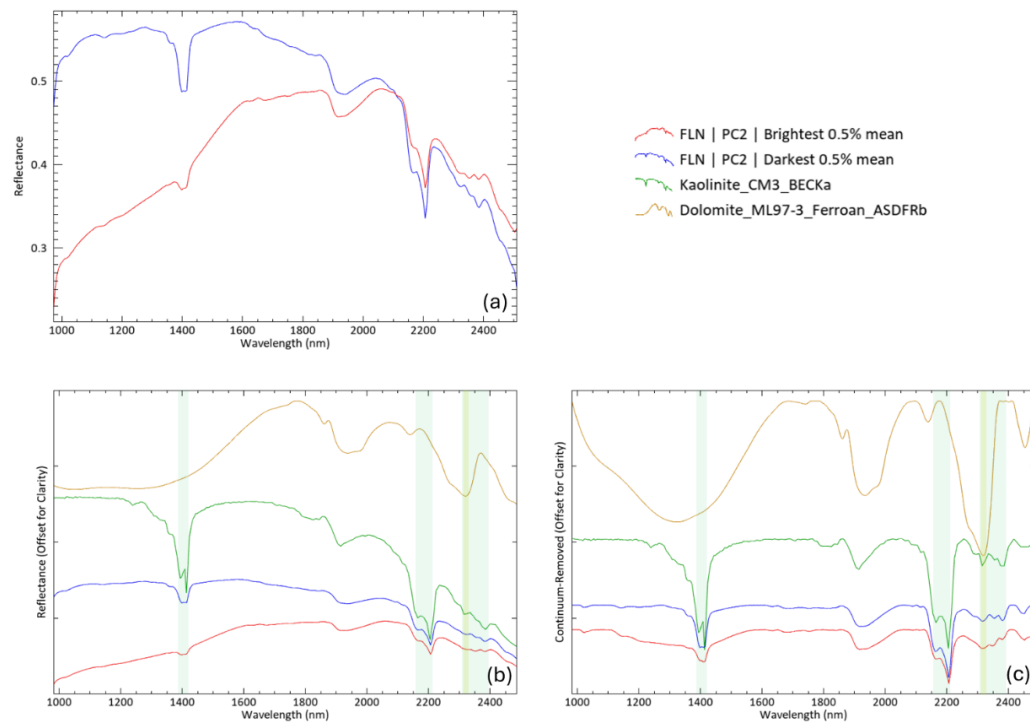


Figure 4.16: Comparing 0.5% of the brightest (red) and darkest (blue) mean spectra of the PC2 band from FLN. (a) Reflectance spectral profiles. (b) Offset reflectance spectral profiles. (c) Continuum-removed offset spectral profiles. Characteristic absorption wavelength ranges of the kaolinite reference spectrum (Kokaly et al., 2017) are indicated with the same profile colour on offset spectral plots to distinguish the feature position on mean spectra.

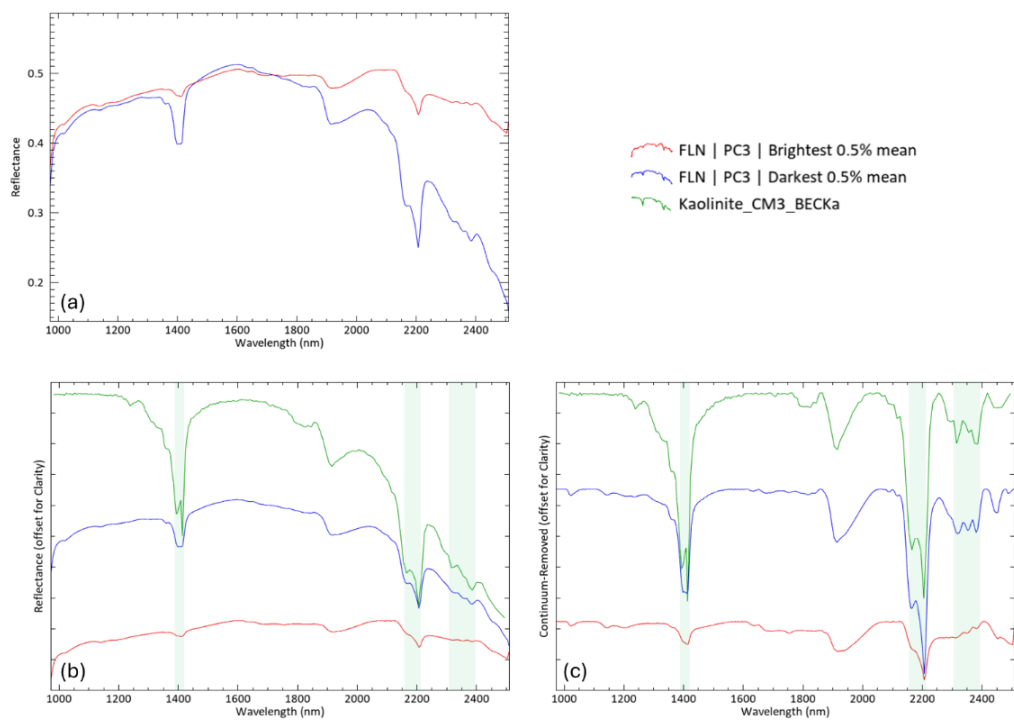


Figure 4.17: Comparing 0.5% of the brightest (red) and darkest (blue) mean spectra of the PC3 band from FLN. (a) Reflectance spectral profiles. (b) Offset reflectance spectral profiles. (c) Continuum-removed offset spectral profiles. Characteristic absorption wavelength ranges of the kaolinite reference spectrum (Kokaly et al., 2017) are indicated with the same profile colour on offset spectral plots to distinguish the feature position on mean spectra.

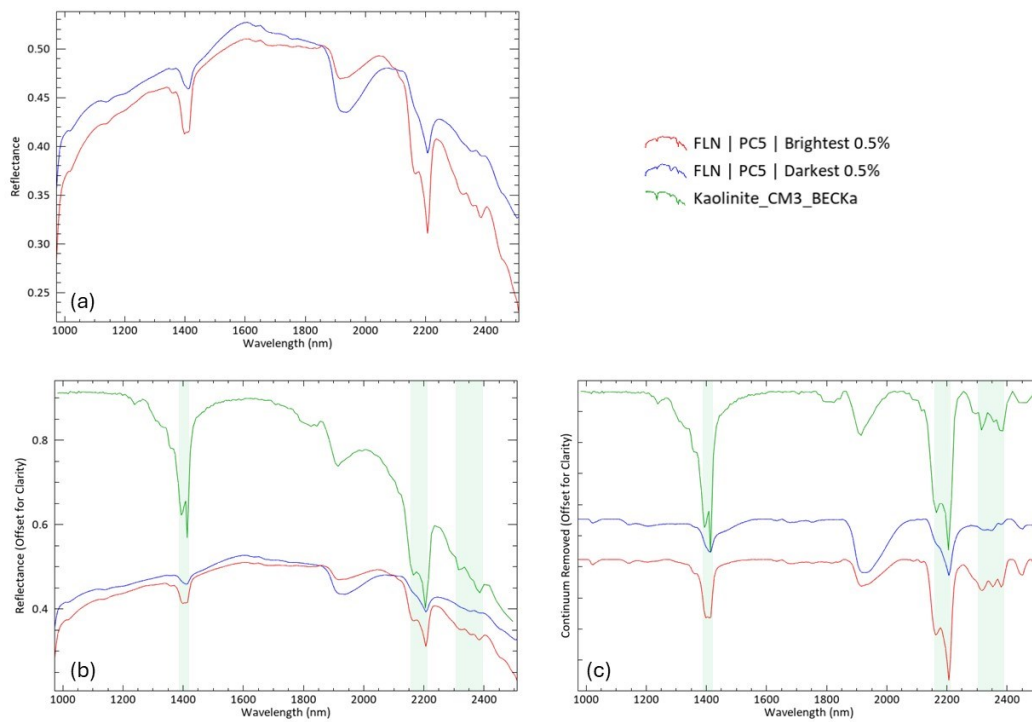


Figure 4.18: Comparing 0.5% of the brightest (red) and darkest (blue) mean spectra of the PC5 band from FLN. (a) Reflectance spectral profiles. (b) Offset reflectance spectral profiles. (c) Continuum-removed offset spectral profiles. Characteristic absorption wavelength ranges of the kaolinite reference spectrum (Kokaly et al., 2017) are indicated with the same profile colour on offset spectral plots to distinguish the feature position on mean spectra.

#### 4.5.2. Analysis of REU PC bands

The mean bright and dark spectra analysis of REU PC bands 1, 2, and 8 are shown in Figure 4.19 –Figure 4.21, respectively. Kaolinite, illite and ferroan dolomite reference spectra from the USGS spectral library (Kokaly et al., 2017) were included in mean spectra comparison plots to confirm the observed absorption features.

Figure 4.19 shows the mean brightest and darkest spectra of REU PC1. The two mean spectra have a contrasting difference in albedo, where the mean brightest spectrum shows the lowest albedo, and the mean darkest spectrum shows the highest albedo. Additionally, the darkest spectrum shows all the characteristic kaolinite absorption features, while the brightest spectrum shows an illite feature at 2350nm and the kaolinite features at other wavelengths.

Figure 4.20 shows the mean brightest and darkest spectra of REU PC2. The two mean spectra have a contrasting difference in spectral profile slope before 1600nm wavelength, where the mean brightest spectrum does not show a slope, while the mean darkest spectrum shows a slope. Other significant observations are that the bright spectrum shows clear characteristic kaolinite triple absorption features around 2350nm, while the dark spectrum shows faded triple features with a single carbonate feature around 2323nm.

Figure 4.21 shows the mean brightest and darkest spectra of REU PC8. The two mean spectra show contrasting differences in the absorption features around 2350nm wavelength apart from the other kaolinite features. The mean brightest spectrum shows characteristics of triple kaolinite features, while the mean darkest spectrum shows a carbonate feature.

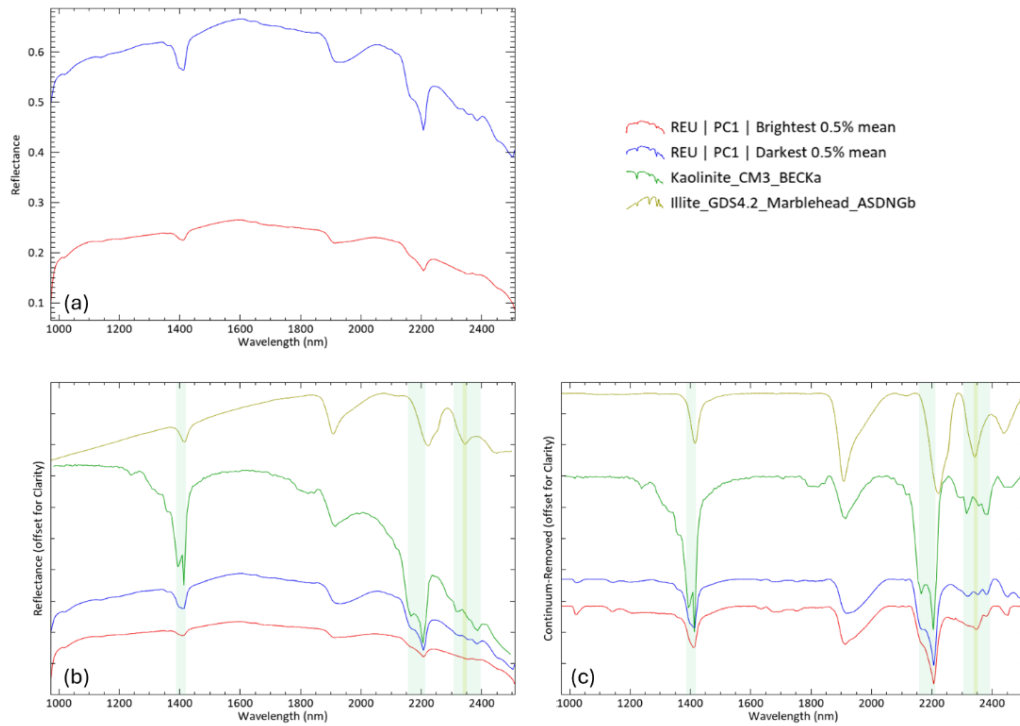


Figure 4.19: Comparing 0.5% of the brightest (red) and darkest (blue) mean spectra of the PC1 band from REU. (a) Reflectance spectral profiles. (b) Offset reflectance spectral profiles. (c) Continuum-removed offset spectral profiles. Characteristic absorption wavelength ranges of kaolinite and illite reference spectra (Kokaly et al., 2017) are indicated with the same profile colours on offset spectral plots to distinguish the feature position on mean spectra.

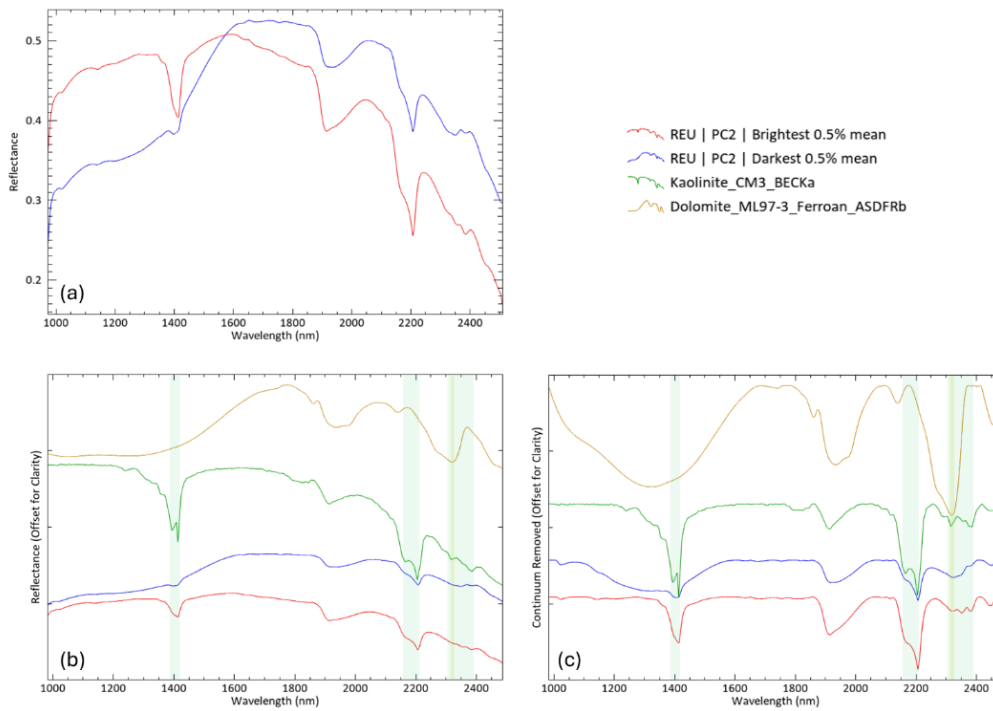


Figure 4.20: Comparing 0.5% of the brightest (red) and darkest (blue) mean spectra of the PC2 band from REU. (a) Reflectance spectral profiles. (b) Offset reflectance spectral profiles. (c) Continuum-removed offset spectral profiles. Characteristic absorption wavelength ranges of kaolinite and ferroan dolomite reference spectra (Kokaly et al., 2017) are indicated with the same profile colours on offset spectral plots to distinguish the feature position on mean spectra.

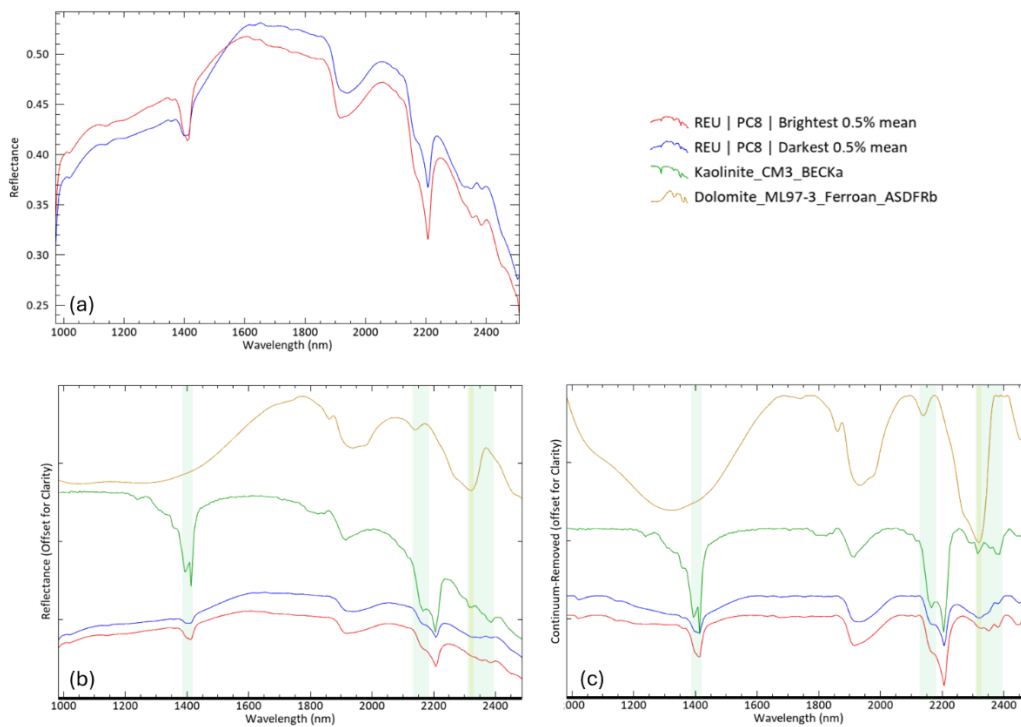


Figure 4.21: Comparing 0.5% of the brightest (red) and darkest (blue) mean spectra of the PC8 band from REU. (a) Reflectance spectral profiles. (b) Offset reflectance spectral profiles. (c) Continuum-removed offset spectral profiles. Characteristic absorption wavelength ranges of kaolinite and ferroan dolomite reference spectra (Kokaly et al., 2017) are indicated with the same profile colours on offset spectral plots to distinguish the feature position on mean spectra.

#### 4.6. Relationships between Band Math-Derived Mineralogical Components and Porosity-Permeability

The variation of spectral indicators identified in PC bands was created using band math operations for albedo, KC, ferrous response, illite/kaolinite ratio, and illite spectral maturity (ISM) as monochrome rasters. The mean values of each sample from a raster were compared against porosity and permeability in scatterplots for all the produced rasters.

##### 4.6.1. Albedo variation; using the reflectance value of SWIR band 1600.72nm

PC1 from both FLN and REU shows the reflectance variation of pixel spectra, and the  $B_{1600.72}$  has the highest reflectance in spectra due to the absence of absorption features. The monochrome images of FLN PC1 and  $B_{1600.72}$  are almost identical in visual comparison (Figure 4.22). Therefore, the mosaic  $B_{1600.72}$  was used to visualise the albedo variation on samples.

The mean values of  $B_{1600.72}$  of each sample were compared against the porosity and permeability of the two wells in scatterplots to identify if a relationship similar to PC scatterplots can be seen. Figure 4.23 and Figure 4.24 show the variation of mean  $B_{1600.72}$  with porosity-permeability in FLN and REU core plugs. Porosity values from both datasets show a positive relationship, while permeability does not show a clear link.

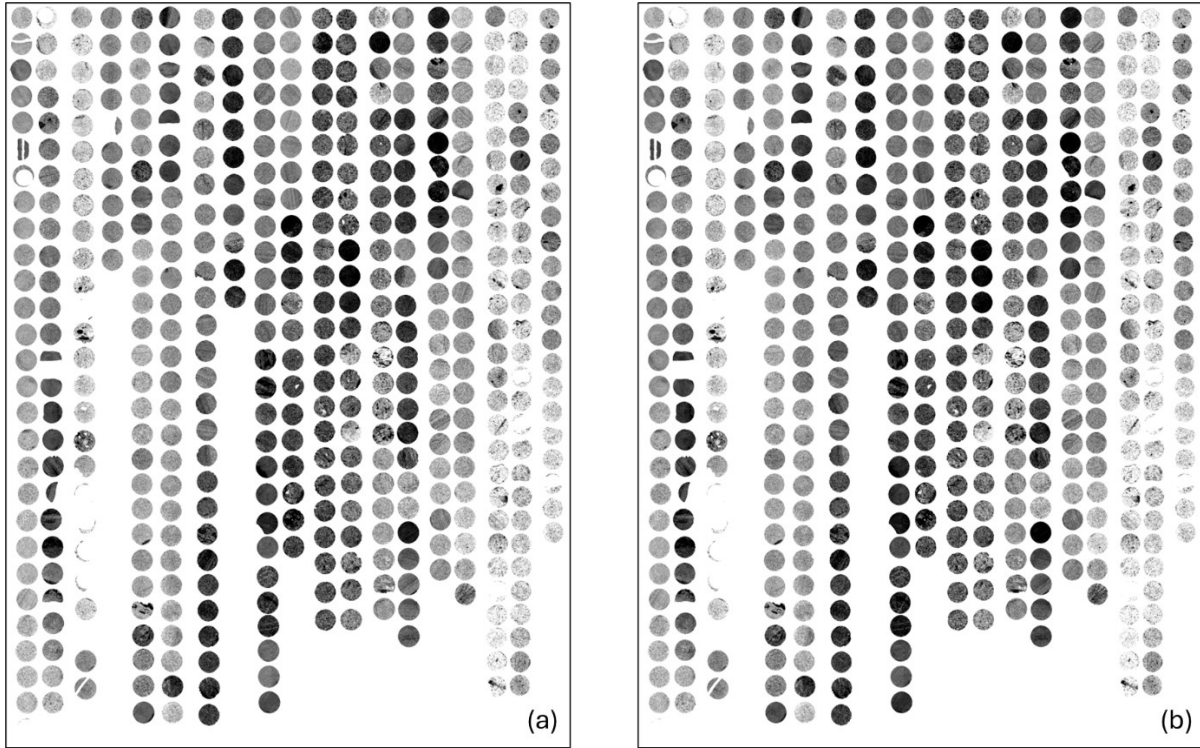


Figure 4.22: Comparison between the monochrome images of (a) Image mosaic 1600.72nm wavelength band and (b) FLN PC1 band.

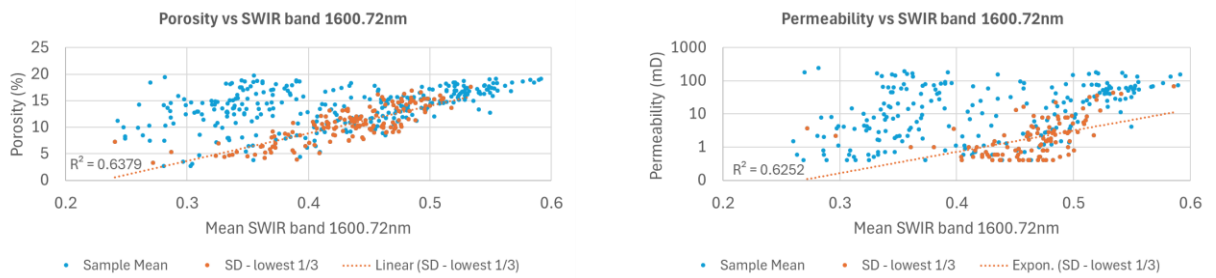


Figure 4.23: Scatterplots of mean 1600.72nm band value of FLN samples against porosity and permeability. The permeability plot has fewer data points than porosity due to samples with no values (disintegrated plugs) and values falling beyond the minimum measuring limits.

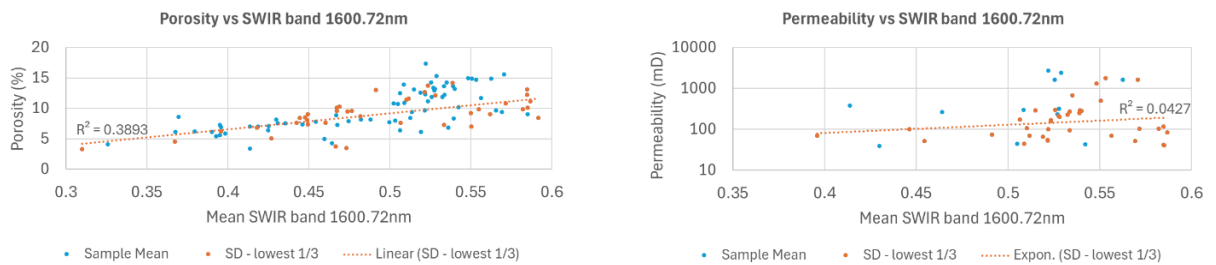


Figure 4.24: Scatterplots of mean 1600.72nm band value of REU samples against porosity and permeability. The permeability plot has fewer data points than porosity due to samples with no values (disintegrated plugs) and values falling beyond the minimum measuring limits.

#### 4.6.2. Variation of kaolinite crystallinity (KC)

The KC variation in SWIR data is shown in Figure 4.25 and was determined by the band math operation adopted from Pontual et al. (1997b) to suit the main characteristic ALOH doublet absorption feature around

2200nm of the image spectra. The calculated KC shows the intensity variation of the kaolinite doublet feature within the highlighted wavelength range, implying the presence of kaolinite in the samples with various crystallinity levels, which is also implied in several PC bands from both FLN and REU.

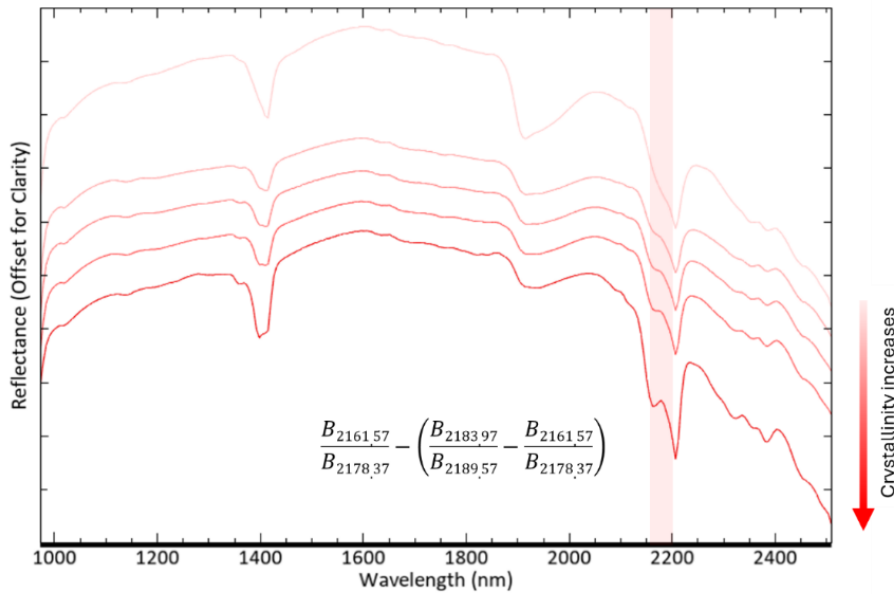


Figure 4.25: Kaolinite crystallinity variation in the dataset, calculated using the given band math operation to indicate the variation of the absorption feature intensity within the highlighted wavelength region. The colour intensity variation is proportional to the crystallinity intensity, where the highest crystallinity is shown in the strong red colour, and the weak crystallinity is shown in faded red.

The mean KC of each sample was compared against the porosity and permeability of FLN and REU wells in the scatterplots shown in Figure 4.26 and Figure 4.27, respectively. Porosity values from both datasets show a positive relationship, while permeability does not show a clear link.

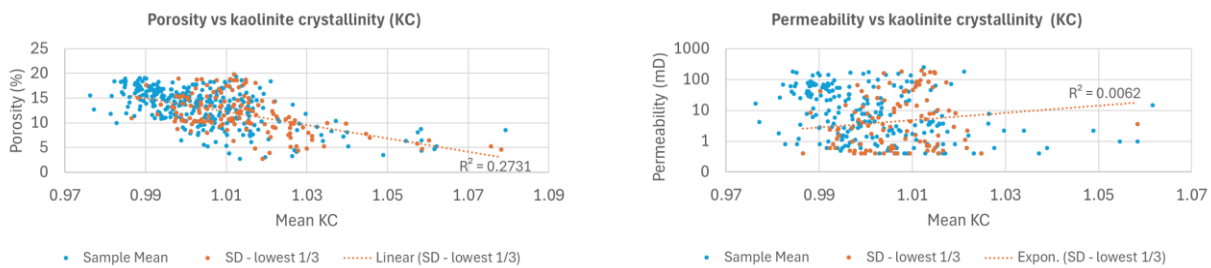


Figure 4.26: Scatterplots of mean KC of FLN samples against porosity and permeability. The permeability plot has fewer data points than porosity due to the samples with no values (disintegrated plugs) and values falling beyond the minimum measuring limits.

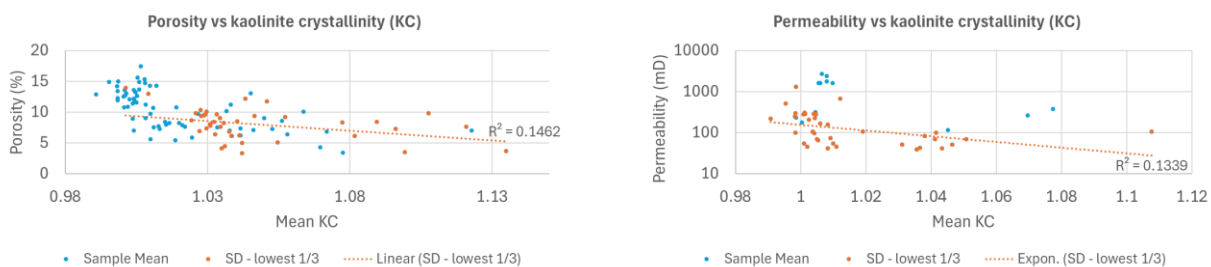


Figure 4.27: Scatterplots of mean KC of REU samples against porosity and permeability. The permeability plot has fewer data points than porosity due to samples with no values (disintegrated plugs) and values falling beyond the minimum measuring limits.

### 4.6.3. Variation of ferrous iron (Fe<sup>2+</sup>) response

The variation of the calculated Fe<sup>2+</sup> response in the image and the band math operation used for parameter calculation is shown in Figure 4.28. The variation is seen with the change of spectral profile within the highlighted wavelength range. It is noted that the spectra with stronger Fe<sup>2+</sup> response also show a carbonate feature around 2325nm, indicating the association of carbonates with the Fe<sup>2+</sup> response.

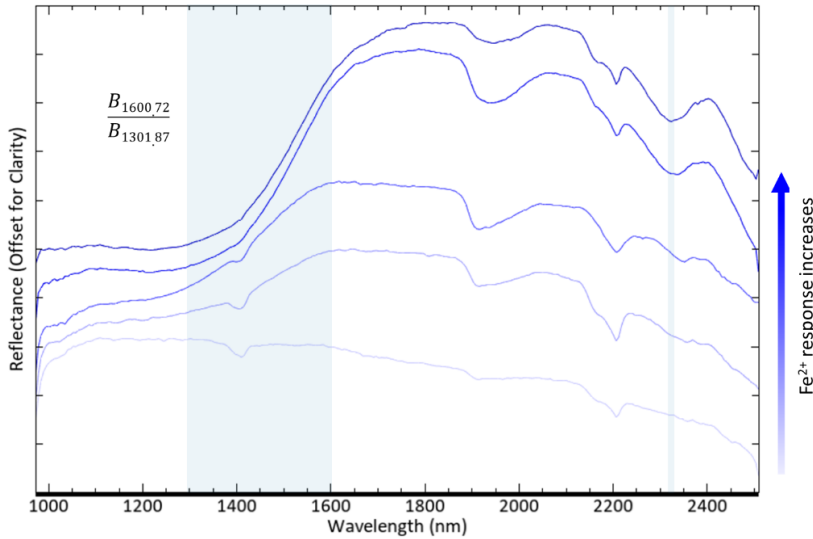


Figure 4.28: Fe<sup>2+</sup> response variation in the dataset, which was calculated using the given band ratio to indicate the variation of the presence of Fe<sup>2+</sup>. The colour intensity variation is proportional to the crystallinity intensity, where the highest response is shown in the strong red colour, and the weak response is shown in faded blue.

The mean Fe<sup>2+</sup> response value of each sample was compared against the porosity and permeability of FLN and REU wells in the scatterplots shown in Figure 4.29 and Figure 4.30, respectively. Both datasets do not show a clear link between the Fe<sup>2+</sup> response and poro-perm.

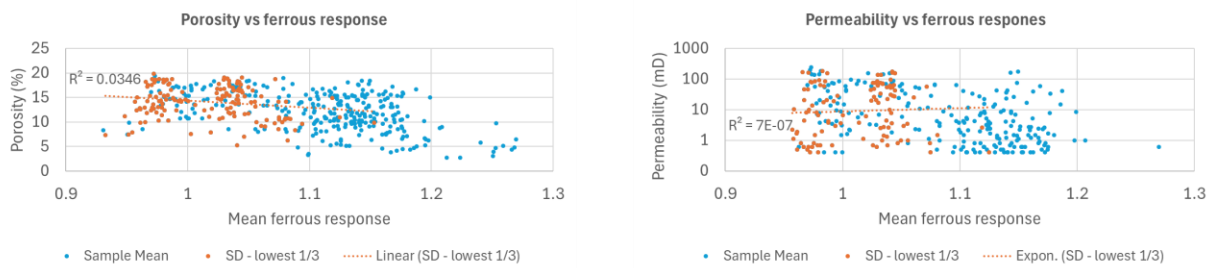


Figure 4.29: Scatterplots of mean Fe<sup>2+</sup> response of FLN samples against porosity and permeability. The permeability plot has fewer data points than porosity due to samples with no values (disintegrated plugs) and values falling beyond the minimum measuring limits.

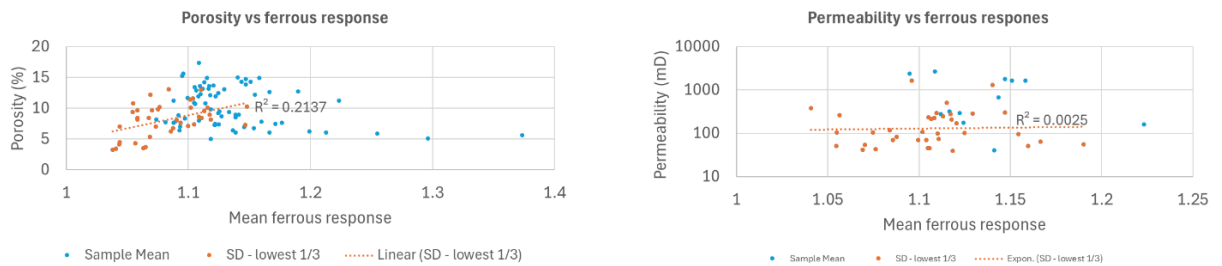


Figure 4.30: Scatterplots of mean Fe<sup>2+</sup> response of REU samples against porosity and permeability. The permeability plot has fewer data points than porosity due to samples with no values (disintegrated plugs) and values falling beyond the minimum measuring limits.

#### 4.6.4. Variation of illite : kaolinite relative proportion

The variation of illite : kaolinite relative proportion in the SWIR image and the band math operation used for parameter calculation is shown in Figure 4.31. The variation is seen with the change of absorption features at the indicated wavelengths. Extreme ends of the variation show clear illite and kaolinite spectra, respectively, indicating illite within the kaolinite-dominated pixel spectra.

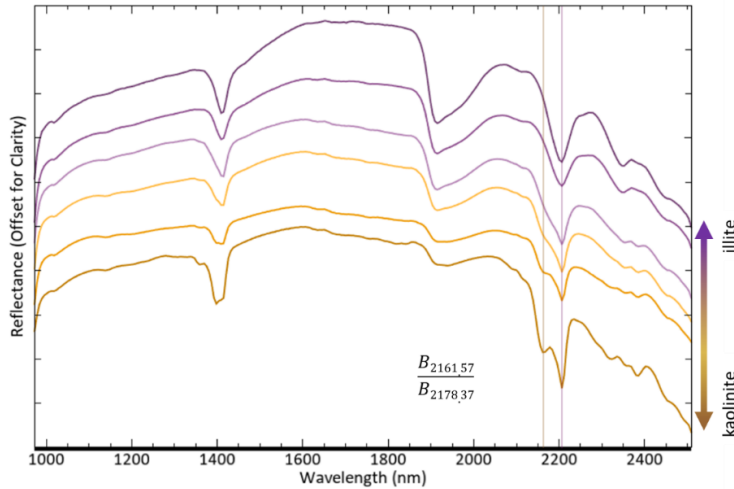


Figure 4.31: The variation of illite : kaolinite relative proportion in the dataset, which was calculated using the given band ratio. The colour intensity variation is proportional to the relative proportion, where 100% illite (0% kaolinite) is indicated with a strong purple colour, and 100% kaolinite (0% illite) is indicated with a strong tan colour.

The mean value of each sample was compared against the porosity and permeability of FLN and REU wells in the scatterplots shown in Figure 4.32 and Figure 4.33, respectively. Both datasets show a negative relationship in porosity scatterplots. Also, a negative trend is seen in the FLN permeability plot, but it does not show a trend with REU permeability.

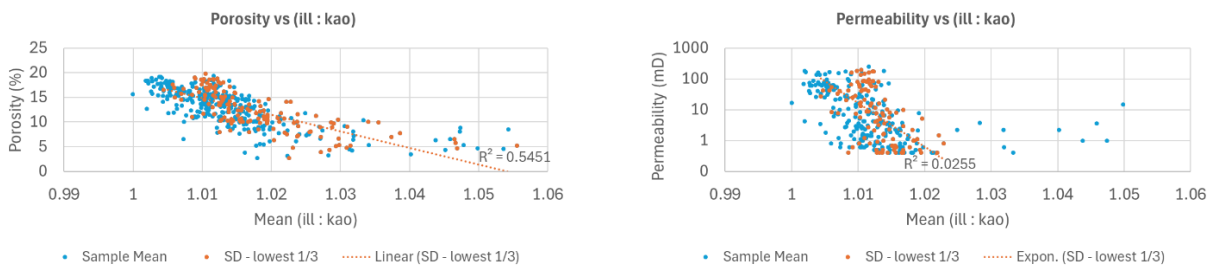


Figure 4.32: Scatterplots of mean illite : kaolinite of FLN samples against porosity and permeability. The permeability plot has fewer data points than porosity due to samples with no values (disintegrated plugs) and values falling beyond the minimum measuring limits.

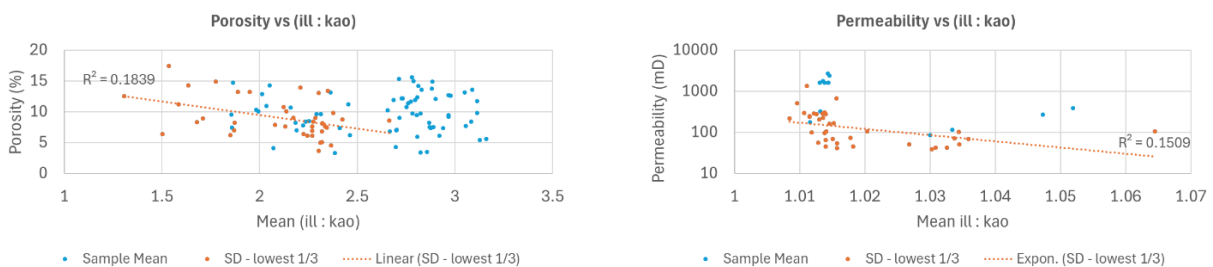


Figure 4.33: Scatterplots of mean illite : kaolinite of REU samples against porosity and permeability. The permeability plot has fewer data points than porosity due to samples with no values (disintegrated plugs) and values falling beyond the minimum measuring limits.

#### 4.6.5. Variation of illite spectral maturity (ISM)

The variation of ISM in the SWIR image and the feature depth ratio used for parameter calculation are shown in Figure 4.34. The top two spectral profiles are the pure illite spectra found in the SWIR dataset, and the calculated ISM variation is shown in purple colour spectra. Spectra showing higher calculated ISM do not show pure illite features at the indicated wavelength due to the influence of kaolinite features.

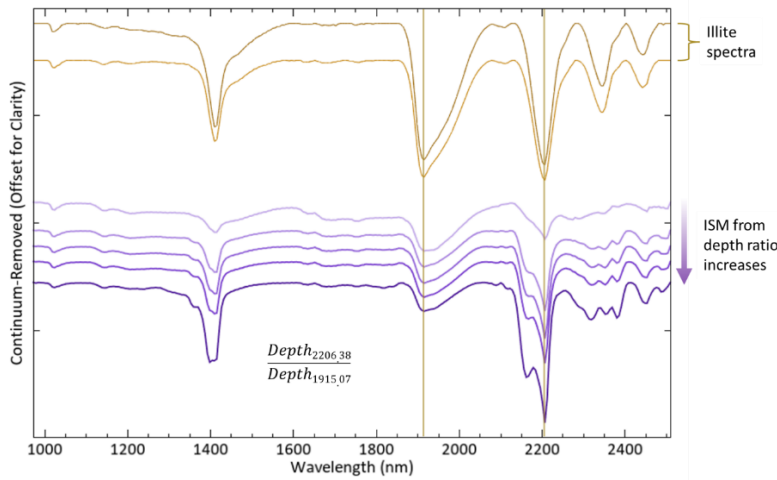


Figure 4.34: The ISM variation in the dataset, which was calculated using the given depth ratio, where the depths were calculated on continuum-removed spectra. Pure illite spectra from the dataset are shown in dark yellow, and ISM variation is shown in purple. The colour intensity variation is proportional to the calculated intensity, where the highest ISM is shown in the strong purple, and the weak crystallinity is shown in faded purple.

The mean parameter value of each sample was compared against the porosity and permeability of FLN and REU wells in the scatterplots shown in Figure 4.35 and 43, respectively. Porosity and permeability do not show a clear relationship with the ISM from both datasets.

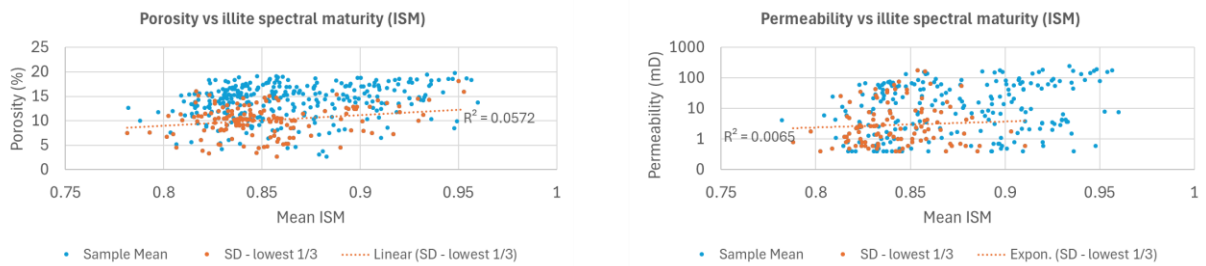


Figure 4.35: Scatterplots of mean IC of FLN samples against porosity and permeability. The permeability plot has fewer data points than porosity due to samples with no values (disintegrated plugs) and values falling beyond the minimum measuring limit.

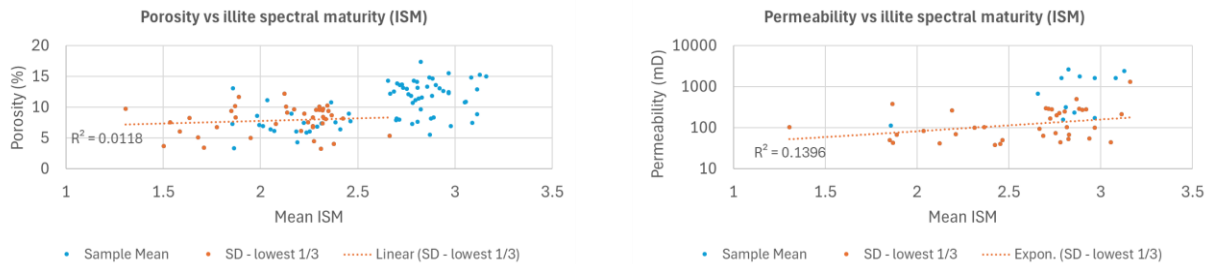


Figure 4.36: Scatterplots of mean IC of REU samples against porosity and permeability. The permeability plot has fewer data points than porosity due to samples with no values (disintegrated plugs) and values falling beyond the minimum measuring limits.

#### 4.7. Visualising the Mineralogy Distribution Causing the Porosity-Permeability Variation

The scatterplots of PC bands and band math-derived spectral indicators identified several positive and negative mineralogical effects on petrophysical properties (porosity has more factors than permeability). SWIR albedo in the studied sandstone should represent feldspar-quartz abundance because they do not have absorbances in the SWIR range. Table 4.3 summarizes all the identified mineralogical factors from SWIR data for causing poro-perm variation.

Table 4.3: Summary of the mineralogy identified as causing poor-perm heterogeneity

Mineralogy	Causing the variation of		Relationship to the poro-perm
	Porosity	Permeability	
Albedo; feldspar-quartz rich	√	√	Positive
Fe <sup>2+</sup> carbonate; dolomite/siderite	√	-	Negative
Illite	√	√	Negative
Highly crystalline kaolinite	√	-	Negative
Weakly crystalline kaolinite	√	-	Positive

Except for the albedo variation, the rest of the four mineralogy were classified by the linear spectral unmixing method. The four endmember spectra were selected from the SWIR dataset to represent the four mineralogical constituents, which are shown in Figure 4.37.

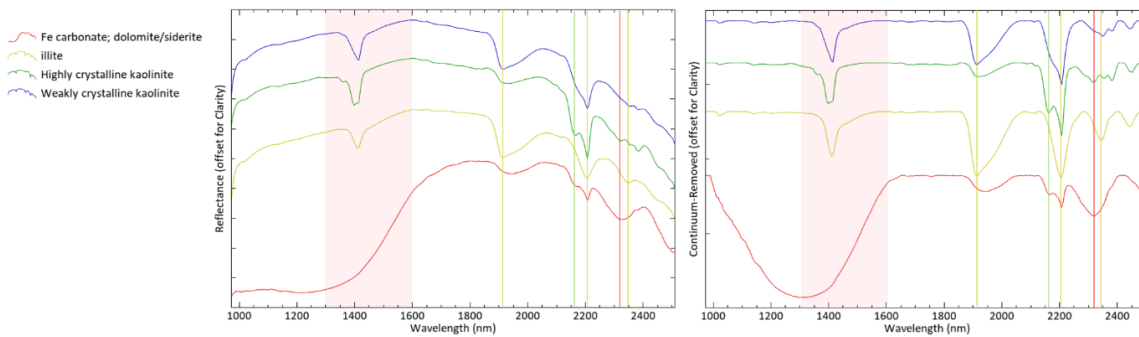


Figure 4.37: Spectral profiles of endmember spectra extracted from the SWIR data for the linear unmixing classification.

The distribution of the four endmembers across the samples is shown in Figure 4.38 with two RGB colour composites. Each colour composite contains all the analysed samples from both FLN and REU wells. The beginnings and ending of *De Lutte* and *Tubbergen* are indicated in both colour composites. Highly crystalline kaolinite and weakly crystalline kaolinite are assigned green and blue in both the colour composites. The red represents siderite and illite in Figure 4.38a and Figure 4.38b, respectively.

In Figure 4.38a, green represents samples with high KC, while pink/purple (blue and red) represents samples with low KC and Fe<sup>2+</sup> carbonate. The brightest green samples are seen in FLN and are relatively more abundant in *De Lutte* than in the *Tubbergen* samples. Pink/purple are more abundant in *Tubbergen* than in *De Lutte*. In REU, samples seen in green are less bright than in FLN, indicating the lesser abundance of highly crystalline kaolinite. Green is generally not mixed with red, indicating an absence of Fe<sup>2+</sup> with illite.

In Figure 4.38b, yellow represents samples with high KC and illite, while blue represents weakly crystalline kaolinite. Bright yellow samples are seen in FLN and are relatively more abundant in *De Lutte* than in the *Tubbergen* samples. Blue are more abundant in *Tubbergen* than in *De Lutte*. In REU, samples seen in yellow are less bright than in FLN, indicating the lesser abundance of illite and highly crystalline kaolinite. In general, blue is not mixed with red, which indicates the absence of weakly crystalline kaolinite with illite.

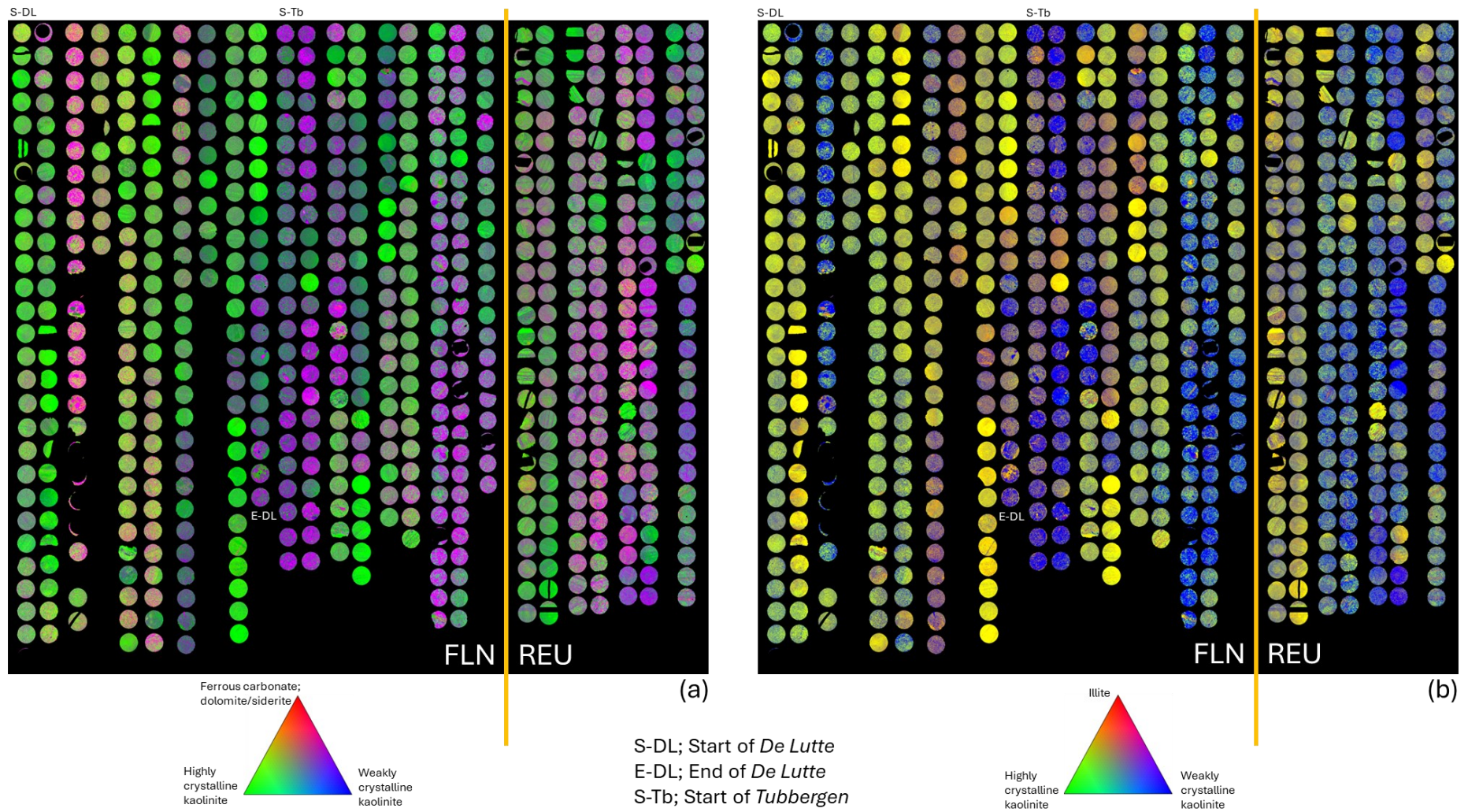


Figure 4.38: Endmember RGB colour composites of linear spectral unmixing of the mosaic image. A colour composite consists of both FLN and REU datasets and the boundary between the two datasets is demarcated with a line. The beginning and end of the *De Lutte* samples are indicated in the FLN section as in the legend. Both colour composites have the same endmember/mineralogy for green and blue colours for convenience comparisons.

## 5. DISCUSSION

### 5.1. Datasets

#### 5.1.1. Porosity and Permeability Datasets

The FLN poro-perm data used in the current research also contains a part of the *De Lutte* formation (From label 1 to 230 in Figure 4.7b) because of having samples with high poro-perm values. As shown in Figure 5.1, certain *De Lutte* samples have a higher value than the *Tubbergen* formation samples. However, the number of higher-value samples is less than the *Tubbergen* formation. Additionally, a clear boundary between the two formations cannot be defined (Kombrink et al., 2007) due to the inherited similar characteristics. Hence, including the *De Lutte* samples for the research analysis was useful.

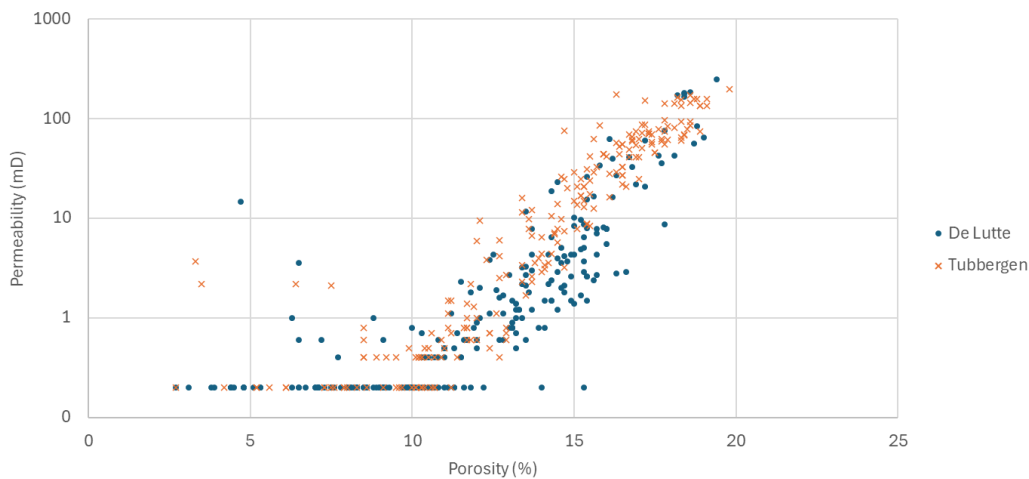


Figure 5.1: Porosity and permeability distribution of the samples from *De Lutte* formation relative to the *Tubbergen* formation values. *De Lutte* samples cover the complete poro-perm range of the *Tubbergen* samples.

#### 5.1.2. SWIR Hyperspectral Data

Some of the reflectance image pixels, especially the clastic pixels from quartz and feldspar, contain the plastic absorption features in the spectra. This cannot be caused by the rock-plastic mixed pixels at the plug boundaries because mixed pixels were masked with adequate buffer to the sample edges. The source of the plastic features should be the scanning tray, most probably caused by multiple reflectances between the plastic tray, minerals (from the highly reflective grains such as quartz and cleavage surfaces of feldspars) and the sensor. Therefore, using a spectrally inactive background for data acquisition is crucial.

### 5.2. Data Analysis

#### 5.2.1. PC band colour composites

PC band colour composites show the distributions of their spectral indicators across the samples, visualising patterns and zones at different depth levels. Different colours represent the dominance/absence of contributing PCs to pixels, where plugs with similar colours can be categorised together for having similar components (characteristics). Different colours at various depths can have implications for different mineralogy. However, connecting samples of the same colour directly to a poro-perm value range has proven challenging.

The identified distinguishable colours from the Colour composites were plotted on the porosity vs permeability plots (Figure 4.9 and Figure 4.10) to reveal if the colours represent different ranges of physical

properties. Only the samples with homogenous colour appearance were chosen to be included in the scatterplots because inhomogeneous colours may not relate to their petrophysical properties. Hence, some samples are incompatible with any colour category and were not included in scatterplots. It can be observed that the samples with the same colour occur concentrated together, emphasising different poro-perm zones on the plots.

The coloured poro-perm plot of FLN in Figure 4.9 shows the concentration of data points of the same colour together, except for very few numbers of plugs. Samples rich in certain colours are abundant with the information represented by corresponding PC bands and lack the constituent of other PCs. Pink, purple and yellow colour groups occupy the same region in the high poro-perm zone. The colour groups with greenish varieties and maroon are zoned in low to very low regions. The orange and dark purple (decreased blue/PC1 and red/PC3) samples are seen between the high and low regions of the plot. Thus, it can be confirmed that samples abundant with PC2 (green) have low poro-perm values, and samples rich with PCs 3 and 1 (light purple; bluer and some red) are prone to have higher poro-perm values. Another important observation is that lighter purple points (more blue/PC1) are in the high-value zone within the purple varieties, while dark purple (less blue/PC1) points are in the lower-middle zone, implying that as PC1 increases, poro-perm values also increased.

The coloured REU poro-perm plot in Figure 4.10 also shows the concentration of data points with similar colours. However, a few distinct colour groups could be identified in the REU PCA colour composite (Figure 4.8) due to the heterogeneous colour distribution on the samples. Poro-perm values in purple variances are at a higher value range, while greenish and orange groups are in lower zones. Therefore, it can be concluded that the samples abundant with PC2 (green) possessed reduced poro-perm values. On purple varieties, dark purple (less blue/PC1) points are in the higher values zone, while light purple (more blue/PC1) points are zoned slightly below the darker group. Strong blue samples are located in the low poro-perm zone, indicating the poro-perm values decrease as the (blue) PC1 increases.

Similarities are noticed in both coloured poro-perm plots, such as purple colours occupying the higher value regions and greenish colours occupying the lower value regions. A sharp horizontal bottom line in the lower value zone is caused by the assigned permeability value of 0.2 mD to the samples indicated as the permeability is  $< 0.4$  mD in the original poro-perm reports.

The interpretation of coloured poro-perm plots is qualitative and subjective due to the selection of colour groups and the nature of categorising samples, which depends on the analyst's perspective.

### 5.2.2. Relationships between PC bands and porosity-permeability

The subsequent analysis of comparing PC mean values of plugs with poro-perm values reveals several clear links in the plots with porosity. FLN plots of porosity vs mean PC (Figure 4.11) showed linear trends with PC bands 1, 2, 3, and 5. PC1 and PC3 have positive relationships, while PC2 shows a negative trend. Data points of the other plots do not show clear relationships to porosity. However, clear relationships cannot be seen between permeability and the PC mean values in the scatterplots (Figure 4.12).

The REU plots of porosity vs mean PC (Figure 4.13) show clear linear trends in PC1, PC2, and PC8. The first two PCs have a negative relationship with porosity, while PC8 shows a positive trend. The rest of the PCs do not display a distinguishable relationship with porosity. Like FLN, REU permeability also does not show clear links with any PCs (Figure 4.14).

It is important to mention that permeability vs mean PC scatterplots for both datasets do not contain the 0.2 mD assigned permeability for the plugs, which were indicated as permeability  $< 0.4$  mD in the original report, because many data points with 0.2 mD show a sharp bottom line in the scatterplots, as in Figure 4.9 and Figure 4.10. This could lead to incorrect interpretations. Notably, the number of data points for the

REU permeability scatterplots is decreased due to fewer samples with values above the detection limit (< 0.4 mD).

All the plots of mean PC against the poro-perm show the most homogenous sample for each PC band, showing the samples with the lowest 1/3 of SD. This was done by sorting the data points in ascending order of the SD. Better results could have been achieved if SD values had been normalised before the sorting because SD would have become high if the mean value had also been high. The standard normalisation (dividing the SD by the mean value) is not accurate to use for PC values since PC values are derived on an “interval scale”, where the values do not have a meaningful “zero” (ratio scale).

### 5.2.3. PC band spectra analysis of FLN

The mean spectra comparison of PC1 from FLN (Figure 4.15) gives the albedo as the main spectral difference. This means PC1 bright pixels highlight the image pixels with the highest reflectance, and dark pixels highlight the pixels with the lowest reflectance. The continuum-removed profile shows that both spectra contain the AlOH, water, and hydroxyl absorption features, and their wavelength positions match the kaolinite spectrum. Also, kaolinite doublet features around 2200nm and 1400nm are weaker in the dark mean spectrum, indicating decreased crystallinity. An uncertainty is implied about the crystallinity variation within mean spectra since absorption features may not be seen accurately in spectra with very low reflectance. Additionally, features from the plastic tray are seen in the continuum-removed profiles. Therefore, it can be concluded that the PC1 represent the albedo from the SWIR data.

The difference in mean spectra of PC2 from FLN (Figure 4.16) is the bright spectrum tilt within the wavelength range of 1600 – 1100nm, likely caused by the presence of Fe<sup>2+</sup>. All the other absorption features from both spectra are similar to kaolinite features. Additionally, the characteristic kaolinite doublet feature around 2200nm is less intense in the bright spectrum than the dark spectrum, implying that the bright highlights the weakly crystalline kaolinite, which is also observed in the PC1 dark spectrum. Also, the characteristics of triple kaolinite feature around 2350nm in the bright spectrum are less intense due to two possibilities. The first is the poor kaolinite crystallinity, and the second is the influence of a ferrous carbonate feature. Therefore, it can be concluded that the possible interpretation of the PC2 spectral information is the presence of Fe<sup>2+</sup> and carbonates vs kaolinite crystallinity.

The difference in mean spectra of PC3 from FLN (Figure 4.17) is the feature depth around 2200nm. The characteristic kaolinite doublet in the dark spectrum is deeper than in the bright spectrum, highlighting the mineral abundance (Haest et al., 2012). Also, the dark spectrum shows a higher intensity in the doublet feature than the bright spectrum, indicating the variation in kaolinite crystallinity. Therefore, it can be concluded that the complete interpretation of the spectral information of the PC3 is the abundance of weakly crystalline kaolinite.

The difference in mean spectra of PC5 from FLN (Figure 4.17) is the intensity variation of characteristic kaolinite absorption features. The bright spectrum shows more strong features than the dark spectrum. In the dark spectrum, the doublet feature around 2200nm and triple features around 2350nm become weaker, and the OH feature at 1900nm is deeper than the bright spectrum. The transition of features from bright to dark spectra can be caused by the increasing illite relative to kaolinite. Therefore, it can be concluded that the FLN PC5 band represent the kaolinite : illite relative proportion.

### 5.2.4. PC band spectra analysis of REU

The mean spectra comparison of PC1 from REU (Figure 4.19) gives the albedo the main spectral difference similar to the PC1 from FLN. The dark spectrum has the highest reflectance and shows a very weak kaolinite feature (the feature at the shorter wavelength of the doublet has almost disappeared) around 2200nm. The

continuum-removed profiles show that the dark spectrum's AlOH, water, and hydroxyl absorption features are matched with kaolinite. However, the bright spectrum has low reflectance, and the characteristic kaolinite features are mixed with illite features. The kaolinite doublet features around 1400nm and 2200nm have almost disappeared, while the unique triple feature around 2350nm is mixed with the illite/sericite feature. Therefore, it can be concluded that the complete interpretation of the spectral information of the PC1 as the illite : kaolinite and the low albedo.

PC2 analysis of REU shows several differences between the mean spectra (Figure 4.20). The most notable feature is the dark spectrum tilt between the 1100 – 1600nm wavelength range. Also, a carbonate feature appears at 2324nm (the wavelength position is common to siderite and ferroan dolomite). Hence, the dark spectrum shows the presence of Fe<sup>2+</sup> and carbonate, possibly caused by a ferrous-bearing carbonate such as siderite and Fe-dolomite. The bright spectrum contains the typical weakly crystalline kaolinite features. Also, the bright spectrum becomes deeper after 1600nm than the dark spectrum, implying a greater abundance of kaolinite. Therefore, it can be concluded that the complete interpretation of the spectral information of the PC2 as kaolinite abundances vs Fe<sup>2+</sup> bearing carbonate.

PC8 analysis of REU (Figure 4.21) shows the tilt between the 1100 – 1600nm wavelength range in both mean spectra caused by Fe<sup>2+</sup>. The dark spectrum has a stronger tilt than the bright profile. Both mean spectra show features similar to weakly crystalline kaolinite around 2200nm. The rest of the bright spectrum features at higher wavelengths are similar to kaolinite. Thus, the bright spectrum should indicate the weakly crystalline kaolinite due to Fe<sup>2+</sup> in the crystal structure. The dark spectrum has the carbonate feature at 2318nm. Therefore, it can be concluded that the complete interpretation of the spectral information of the PC8 is the presence of weakly crystalline kaolinite vs. ferrous-bearing carbonate.

Table 5.1 gives the summary of the spectral information from PC bands.

Table 5.1: Summary of PC band spectral information from PCA of FLN and REU, with clear trends in Porosity vs mean PC scatterplots.

<b>Dataset</b>	<b>PC band</b>	<b>Spectral information</b>	<b>Observed trend: mean PC vs Porosity</b>
FLN	1	High albedo	Positive
	2	Contents of Fe <sup>2+</sup> and carbonates vs kaolinite	Negative
	3	Weakly crystalline kaolinite	Positive
	5	Kaolinite : illite relative proportion	Positive
REU	1	illite : kaolinite and low albedo	Negative
	2	Contents of kaolinite vs Fe <sup>2+</sup> bearing carbonate	Negative
	8	Contents of weakly crystalline kaolinite vs Fe <sup>2+</sup> bearing carbonate	Positive

It is important to highlight that the PC1 from both the REU and FLN have mainly the reflectance information but have inversed/swapped between mean bright and dark spectra (the bright spectrum of PC1 from FLN has the high reflectance values, while the dark spectrum of PC1 from REU has the high reflectance). Consequently, PC1 from FLN shows a positive trend with porosity, while PC1 of REU shows a negative relationship.

Spectral information on the PC bands from FLN and REU is not identical. However, a few common properties, such as kaolinite crystallinity and abundance, Fe<sup>2+</sup> response, carbonate presence, and illite :

kaolinite, can be identified. The analysis results of the influence on porosity and permeability of these factors are individually discussed in section 5.3.

### **5.2.5. Comparison of PCA colour composite results and porosity scatterplots**

After revealing the spectral mineral information from the PC bands, it is possible to interpret the colours of poro-perm plots shown in Figure 4.9 and Figure 4.10. In section 4.2.1, It is described that FLN coloured poro-perm plot in Figure 4.9, the purple colour varieties from PC1 and PC3 are zoned in the high poro-perm region while green colours from PC2 are concentrated in the low poro-perm zone. The observations tally with the porosity vs mean PC plots where the mean values of PC1 and PC3 have positive trends with porosity, while mean PC2 has a negative trend. This implies that the sample with high SWIR albedo (PC1) and weakly crystalline kaolinite (PC3) have higher poro-perm and Fe<sup>2+</sup> bearing carbonates (PC2) caused to have low poro-perm.

Similarly, in the REU coloured poro-perm plot in Figure 4.10, samples rich in green and blue from PC2 and PC1 are zoned in the low poro-perm region, indicating their negative relationship with porosity. This implies that the relative illite content, low albedo (PC1), and Fe<sup>2+</sup> bearing carbonates (PC2) cause low poro-perm in samples.

## **5.3. The Effects of Identified Mineralogical Variants to the Sandstone Porosity-Permeability**

The following sections describe the individual comparisons of identified spectral mineralogical terms from PC bands against the porosity and permeability. The assessments were done separately for the two sets due to the uncertainty of poro-perm measuring methods used for the two drill holes. Unlike the PCA for the two datasets, applying spectral mineralogical terms has the same impact on the two datasets since band math operations are used with the same wavelengths.

Trends in FLN scatterplots are more apparent than in REU plots, possibly for two reasons. First, if the number of data points in REU is considerably lower than the FLN, they are insufficient to show contrast on plots. Second, the mineralogical effects within the two datasets can be different due to different geological processes.

### **5.3.1. The effect of SWIR albedo on porosity and permeability**

Analysis of albedo of reflectance spectra is challenging due to factors such as mineralogy, particle size, grain separation, and surface roughness (Le Bras & Erard, 2003). PC1 from both FLN and REU shows that SWIR albedo has a positive relationship with porosity. From the SWIR spectra of the dataset, it is observed that the B<sub>1600.72</sub> has the highest reflectance and does not show any absorption features. When examining the FLN PC band 1 and B<sub>1600.72</sub> in greyscale, feldspar and quartz-dominated (sandstone) plugs are seen in brighter tones, while fine-grained (claystone/mudstone) plugs appear in darker tones, as shown in Figure 5.2. This is seen in the samples with clasts, where feldspar appears as the brightest (white), followed by quartz in FLN PC band 1 and B<sub>1600.72</sub> in Figure 5.3.

The observations and the behaviour can be explained as follows. Feldspar and quartz, which are dominant in sandstone, do not have absorbance in the SWIR range; thus, the pixels containing them reflect more. However, the SWIR spectra of feldspar-quartz consist of the absorption features of another mineral from the samples because the produced clay minerals kaolinite/illite can retain on feldspar-quartz.

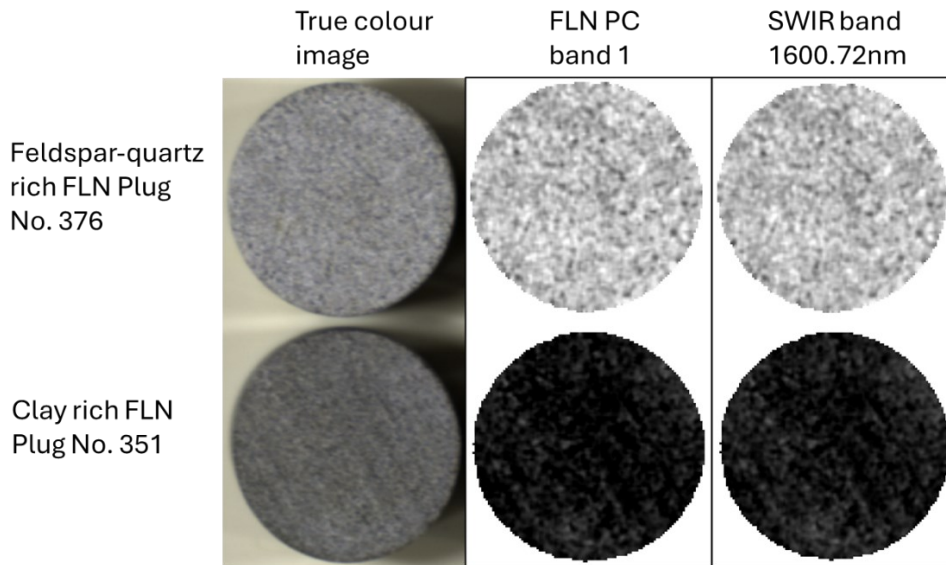


Figure 5.2: Comparison of feldspar-quartz-rich and clay-rich samples using true colour, PC band 1, and SWIR band 1600.72nm. Variation of mineral enrichments is seen in different colour tones.

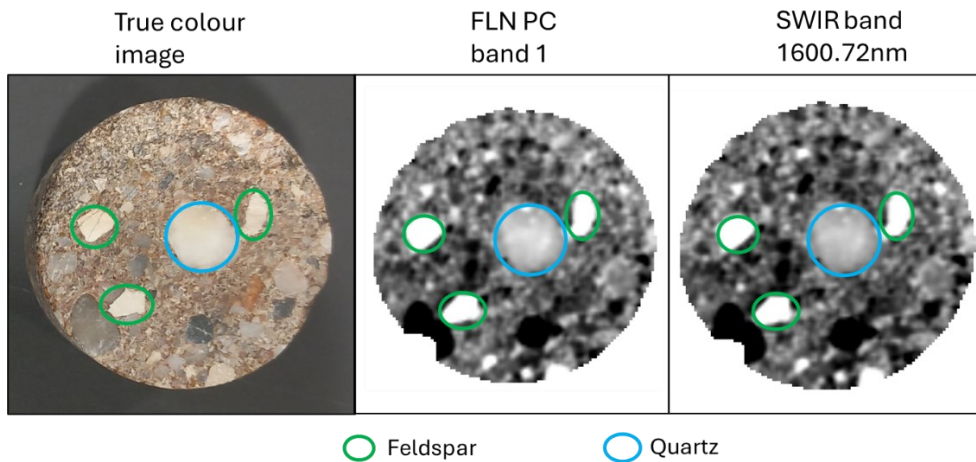


Figure 5.3: Comparison of albedo variation in a core plug with feldspar and quartz clasts between the PC band 1 and SWIR band 1600.72. Feldspar clasts are encircled in green, and quartz is encircled in blue in the three images.

The scatterplots of mean  $B_{1600.72}$  show a positive trend with both porosity and permeability on FLN samples. REU porosity also shows a positive trend with porosity. However, permeability does not show a clear link. Therefore, it can be argued that  $B_{1600.72}$  can be used for albedo variation of the SWIR dataset, distinguishing the feldspar-quartz-rich locations from the clay-rich zones. This can be supported by the fact that sandstone rich with quartz-feldspar usually possesses higher reservoir quality than clay-rich rocks.

### 5.3.2. The effect of kaolinite crystallinity on porosity and permeability

KC shows a negative trend with porosities from both drill holes. The negative trend is distinctly seen in FLN data and slightly seen in REU data. The data points in the FLN permeability plot do not show an identifiable trend. However, the REU permeability plot shows a weak negative trend with low SD samples. Reasons for the weak trends in REU could be the low number of data points or the varied kaolinite crystallinity effect due to the sample mineralogy.

Worden & Morad (1999) describe the negative relationship between KC and the poro-perm as follows. During the diagenesis of sediments, low crystalline kaolinite is mineralised at the expense of feldspar

(plagioclase). As diagenesis progresses with the increasing temperature, high KC dickite growth happens from the kaolinite, which acquires more space reducing porosity and permeability.

The band math operation used to measure the kaolinite crystallinity is influenced by other AIOH minerals, specifically by the confirmed presence of illite in the samples because the two minerals have a common absorption feature position at 2178nm, which considers illite as poorly crystalline kaolinite affecting the parameter results. However, it is observed that kaolinite has a dominant presence over illite. Thus, the illite may not drastically impact the parameter calculation, which is still useful for the analysis.

### 5.3.3. The effect of Fe<sup>2+</sup> response on porosity and permeability

Fe<sup>2+</sup> response is the tilt/drop/slope of the SWIR spectra observed within the wavelength range of 1300 – 1600nm, caused by the presence of Fe<sup>2+</sup> (Pontual et al., 1997a). This tilt becomes stronger as its presence increases and disappears as the abundance diminishes.

Fe<sup>2+</sup> response alone does not show a clear relationship with both physical properties from drill holes. Several sources can cause Fe<sup>2+</sup> response. Strong Fe<sup>2+</sup> response (concave shaped drop in spectra) can be produced by ferrous bearing carbonates such as ferroan dolomite and siderite (Ankerite also a Fe carbonate. However, PC bands that include carbonate features which show trends with porosity, do not have features at the wavelength position of ankerite 2330 – 2340nm). It is challenging to decide the carbonate feature as ferroan dolomite or siderite because the subjective carbonate feature in both minerals can vary within a common wavelength range (dolomite; 2320 – 2338nm, siderite; 2320 – 2350nm) depending on the proportion of Mg and Mn substitutions (Pontual et al., 1997c). However, the presence of siderite within the *Tubbergen* formation has been reported by Post (2021) and Kombrink et al. (2007).

A moderate response can be seen in some kaolinite and illite spectra, where Fe<sup>2+</sup> is available within the mineral structure. Especially weakly crystalline kaolinite may contain Fe<sup>2+</sup> within the natural crystal structure (Herbillon et al., 1976; Mestdagh et al., 1980). Also, the parameter can be altered by the spectra with low albedo, which do not display the slope well (Pontual et al., 1997b).

Carbonate variation cannot be shown using band arithmetic operation because the dominant presence of kaolinite and illite in the dataset affects the carbonate features in the SWIR range. The only carbonate features that persist in mixed spectra are found within the 2300 – 2350nm range (Pontual et al., 1997b). However, kaolinite and illite also have diagnostic absorption features within the same range, which hampers differentiating carbonates effectively unless the carbonate presence is strong.

### 5.3.4. The effect of illite : kaolinite relative proportion on porosity and permeability

Illite : kaolinite relative proportion shows clear negative relationships with porosity and permeability in FLN data. Also, the negative relationship is seen in REU but less evident than in FLN due to similar reasons as in kaolinite crystallinity, which is a smaller number of data points, and the parameter has less effect on the samples. Porosity and permeability both decreased as the parameter increased.

After the early diagenesis of sediments, kaolinite reacts with K-feldspar, forming fibrous illite and quartz overgrowth (Bjorkum & Gjelsvik, 1988). Fibrous illite severely deteriorates permeability due to bridging pores, with no significant effect on porosity (Morad et al., 2010). However, quartz overgrowth can reduce the porosity. Thus, permeability and porosity are reduced as the illite content increases relative to the kaolinite.

### 5.3.5. The effect of illite spectral maturity on porosity and permeability

ISM does not show a recognisable relationship with porosity and permeability in the scatterplots. Notably, Figure 4.34 shows that the increasing ISM shows a strong kaolinite feature due to the band ratio effect.

Specifically, as the ISM is increased, kaolinite features also become stronger, and the intensity of the main kaolinite doublet increases (indicating higher KC). The reason is that the parameter calculation method is influenced by other AlOH minerals (Pontual et al., 1997b), specifically by the abundant kaolinite in the samples, since the two minerals have the 2200nm absorption feature in common, which modifies the ISM unnecessarily. Therefore, the determined ISM parameter may not reveal the relationship between porosity and permeability.

#### **5.4. Visualising the Distribution of Poro-Perm Controlling Mineralogy with Linear Spectral Unmixing**

Among the identified spectral mineralogical factors for poro-perm variation, feldspar-quartz abundance given by albedo cannot be used as an endmember for linear spectral unmixing because the feldspar and quartz do not have absorption features in the SWIR range. Therefore, the image spectra were unmixed using Fe<sup>2+</sup> carbonate, illite, highly crystalline kaolinite, and weakly crystalline kaolinite as endmember spectra from the SWIR dataset.

The two RGB colour composites of linear spectral unmixing (Figure 4.38) show *De Lutte* more abundant with highly crystalline kaolinite and illite, while weakly crystalline kaolinite and siderite are more dominant in the *Tubbergen*. Weakly crystalline kaolinite and siderite dominance become more apparent in REU samples. The abundance of illite in FLN relative to REU can be why FLN shows a poro-perm trend with lower permeability to REU in Figure 1.3 since the increase of illite reduces permeability.

#### **5.5. Limitations in the Research**

The porosity and permeability of drill cores are measured by obtaining plugs at desired depth levels. Mineralogy observed on the circular surface of a cylindrical plug may not represent the complete mineralogy of the plug if the sample is inhomogeneous. Therefore, the mineralogy derived from SWIR images is accurate only for the homogenous plugs.

The highly dynamic depositional environment of the *Tubbergen* formation can cause unique mineralogical assemblages at different depth levels and laterally within the formation. Also, the two drillholes from which the research data originate do not penetrate the *Tubbergen* formation's complete thickness. Therefore, this study's results should not be treated as the complete representation of poro-perm controlling mineralogy for the *Tubbergen* formation.

## 6. CONCLUSIONS AND RECOMMENDATIONS

### 6.1. Main Findings of the Research

SWIR image analysis on available drill core plugs from FLN and REU of the *Tubbergen* sandstones revealed that the samples are rich in kaolinite, while illite and ferrous carbonates are presented in minor amounts.

PCA is a useful method for analysing SWIR hyperspectral images. Mean PC band values for each sample can be compared with petrophysical properties such as porosity and permeability. However, the interpretation of what mineralogy drives a particular PC component must be carefully considered since several PC bands can represent similar sample information.

Identifying carbonates in the SWIR image becomes challenging in kaolinite-dominated conditions.

The albedo of SWIR reflectance spectra can distinguish between feldspar-quartz and clay-rich zones from the hyperspectral dataset. However, more research is required to understand the complete behaviour of albedo variation.

SWIR HS image analysis of the sandstone core plugs from FLN and REU drill holes reveals the following mineralogical factors that affect the porosity-permeability of the *Tubbergen* sandstone.

- **Enrichment of clay relative to feldspar and quartz reduces the porosity and permeability of *Tubbergen* sandstone.**
- **Siderite diminishes the porosity of the *Tubbergen* sandstone.**
- **Kaolinite crystallinity negatively affects the porosity of *Tubbergen* sandstone.** The porosity is reduced as the abundance of highly crystalline kaolinite increases.
- **Illite : kaolinite relative proportion negatively affects the porosity and permeability of *Tubbergen* sandstone.** When the illite content increases relative to kaolinite in rocks, porosity and permeability are degraded.

The lack of illite causes the poro-perm trend of REU with higher permeability compared to the FLN in Figure 1.3.

### 6.2. Further Refinements for the Current Research

For SWIR data acquisition, it is recommended to use a sample background with no spectral signatures (e.g. a cloth treated with spectrally neutral paint) to avoid the inclusion of unwanted spectral signatures in the samples.

The current research methodology can be refined by identifying different depositional facies using the slabbed drill cores and analysing plugs from each facies separately. In this way, there is a possibility of narrowing down the characteristic mineralogy for different facies and determining the unique causes of porosity-permeability variation for facies. Additionally, an attempt can be made to analyse textures on samples along with mineralogy and incorporate them with poro-perm analyses.

When using the samples from different drillholes, it is important to confirm the techniques used for poro-perm analysis. If the techniques are different and contrasting poro-perm differences are observed among similar plugs, normalize the data to be compatible for analysis.

### 6.3. Future Research Potential

In addition to the SWIR data, analysing and incorporating LWIR and VNIR data will reveal extra mineralogical components that are not seen and challenging to identify in SWIR (e.g. apart from analysing

quartz and feldspar with LWIR, it is also useful for identifying carbonates, which is difficult to identify in SWIR at the presence of minerals such as illite, kaolinite, and muscovite).

The dynamic depositional environment may have caused different mineralogy to affect porosity-permeability. Therefore, analysing core plugs from different regions containing *Tubbergen* sandstone may reveal additional insight into the complete *Tubbergen* sandstone mineralogy.

The analysis procedure can be extrapolated to the drill core IR images to demarcate high and low porosity-permeability depth regions. Identified depth zones for high-low poro-perm can be compared with existing seismic data to demarcate poro-perm variation within the seismic survey results. Ultimately, the model can be used to analyse the seismic data from the regions with no drill holes available to demarcate regions and depths with high porosity-permeability.



## LIST OF REFERENCES

---

- Asadzadeh, S., & de Souza Filho, C. R. (2016). A review on spectral processing methods for geological remote sensing. *International Journal of Applied Earth Observation and Geoinformation*, 47, 69–90. <https://doi.org/10.1016/j.jag.2015.12.004>
- Bakker, W. (2011). *HypPy User Manual*. <http://hyppy.is-great.org/index.html#download>
- Bioucas-Dias, J. M., Plaza, A., Dobigeon, N., Parente, M., Du, Q., Gader, P., & Chanussot, J. (2012). Hyperspectral Unmixing Overview: Geometrical, Statistical, and Sparse Regression-Based Approaches. *IEEE Journal of Selected Topics in Applied Earth Observations and Remote Sensing*, 5(2), 354–379. <https://doi.org/10.1109/JSTARS.2012.2194696>
- Bjorkum, P. A., & Gjelsvik, N. (1988). An Isochemical Model for Formation of Authigenic Kaolinite, K-Feldspar and Illite in Sediments. *SEPM Journal of Sedimentary Research*, Vol. 58. <https://doi.org/10.1306/212F8DD2-2B24-11D7-8648000102C1865D>
- Boggs, S. (2009). *Petrology of Sedimentary Rocks* (2nd ed.). Cambridge University Press.
- Bonté, D., van Wees, J.-D., & Verweij, J. M. (2012). Subsurface temperature of the onshore Netherlands: new temperature dataset and modelling. *Netherlands Journal of Geosciences - Geologie En Mijnbouw*, 91(4), 491–515. <https://doi.org/10.1017/S0016774600000354>
- Buijze, L., Veldkamp, H., & Wassing, B. (2023). Comparison of hydrocarbon and geothermal energy production in the Netherlands: reservoir characteristics, pressure and temperature changes, and implications for fault reactivation. *Netherlands Journal of Geosciences*, 102(3), e7. <https://doi.org/10.1017/njg.2023.6>
- Burger, J., & Gowen, A. (2011). Data handling in hyperspectral image analysis. *Chemometrics and Intelligent Laboratory Systems*, 108(1), 13–22. <https://doi.org/10.1016/j.chemolab.2011.04.001>
- Christensen, P. R., Bandfield, J. L., Hamilton, V. E., Howard, D. A., Lane, M. D., Piatek, J. L., Ruff, S. W., & Stefanov, W. L. (2000). A thermal emission spectral library of rock-forming minerals. *Journal of Geophysical Research: Planets*, 105(E4), 9735–9739. <https://doi.org/10.1029/1998JE000624>
- Clark, R. N. (1999). *Spectroscopy of rocks and minerals and principles of spectroscopy* (A. Rencz, Ed.). John Wiley and Sons.
- Doublier, M. P., Potel, S., Roache, A., & Geological Survey of Western Australia. (2010). *Application of SWIR spectroscopy in very low-grade metamorphic environments : a comparison with XRD methods*. Geological Survey of Western Australia.
- Duin, E. J. T., Doornenbal, J. C., Rijkers, R. H. B., Verbeek, J. W., & Wong, Th. E. (2006). Subsurface structure of the Netherlands - results of recent onshore and offshore mapping. *Netherlands Journal of Geosciences - Geologie En Mijnbouw*, 85(4), 245–276. <https://doi.org/10.1017/S0016774600023064>
- Dutch Oil and Gas Portal (NLOG). (2023a). *Geothermal map of the Netherlands*. <https://www.nlog.nl/en/geothermal-map-netherlands>
- Dutch Oil and Gas Portal (NLOG). (2023b). *NLOG on Map*. <https://www.nlog.nl/en/map-boreholes>
- Dutch Oil and Gas Portal (NLOG). (2023c). *The drilling*. <https://www.nlog.nl/datacenter/brh-overview>
- Dutch Oil and Gas Portal (NLOG). (2024). *International correlation*. Stratigraphic Nomenclature. [https://www.dinoloket.nl/sites/default/files/nomenclator/internationale\\_correlatie/01\\_SPBA\\_correlation\\_Carboniferous\\_A3.pdf](https://www.dinoloket.nl/sites/default/files/nomenclator/internationale_correlatie/01_SPBA_correlation_Carboniferous_A3.pdf)
- Goetz, A. F. H., Vane, G., Solomon, J. E., & Rock, B. N. (1985). Imaging Spectrometry for Earth Remote Sensing. *Science*, 228(4704), 1147–1153. <https://doi.org/10.1126/science.228.4704.1147>

- Goldstein, B., Hiriart, G., Bertani, R., Bromley, C., Gutiérrez-Negrín, L., Huenges, E., Muraoka, H., Ragnarsson, A., Tester, J., Zui, V., Blackwell, D., Demayo, T., Heath, G., Lee, A., Lund, J. W., Mongillo, M., Newell, D., Sanyal, S., Williamson, K. H., ... Wratt, D. (2011). Geothermal Energy. In *Renewable Energy Sources and Climate Change Mitigation* (pp. 401–436). Cambridge University Press. <https://doi.org/10.1017/CBO9781139151153.008>
- Guatame-García, A., Buxton, M., Deon, F., Lievens, C., & Hecker, C. (2018). Toward an on-line characterization of kaolin calcination process using short-wave infrared spectroscopy. *Mineral Processing and Extractive Metallurgy Review*, 39(6), 420–431. <https://doi.org/10.1080/08827508.2018.1459617>
- Haest, M., Cudahy, T., Laukamp, C., & Gregory, S. (2012). Quantitative Mineralogy from Infrared Spectroscopic Data. I. Validation of Mineral Abundance and Composition Scripts at the Rocklea Channel Iron Deposit in Western Australia. *Economic Geology*, 107(2), 209–228. <https://doi.org/10.2113/econgeo.107.2.209>
- Hannan, M. A., Al-Shetwi, A. Q., Ker, P. J., Begum, R. A., Mansor, M., Rahman, S. A., Dong, Z. Y., Tiong, S. K., Mahlia, T. M. I., & Muttaqi, K. M. (2021). Impact of renewable energy utilization and artificial intelligence in achieving sustainable development goals. *Energy Reports*, 7, 5359–5373. <https://doi.org/10.1016/j.egy.2021.08.172>
- Herbillon, A. J., Mestdagh, M. M., Vielvoye, L., & Derouane, E. G. (1976). Iron in kaolinite with special reference to kaolinite from tropical soils. *Clay Minerals*, 11(3), 201–220. <https://doi.org/10.1180/claymin.1976.011.3.03>
- Hunt, G. R. (1977). Spectral Signatures of Particulate Minerals in the Visible and Near Infrared. *Geophysics*, 42(3), 501–513. <https://doi.org/10.1190/1.1440721>
- Hunt, G. R., Salisbury, J. W., & And, G. (1970). Visible and near-infrared spectra of minerals and rocks: I silicate minerals. In *Modern Geology* (Vol. 1).
- Jolliffe, I. T. (1986). *Principal Component Analysis*. Springer New York. <https://doi.org/10.1007/978-1-4757-1904-8>
- Kokaly, R. F., Clark, R. N., Swayze, G. A., Livo, K. E., Hoefen, T. M., Pearson, N. C., Wise, R. A., Benzel, W. M., Lowers, H. A., Driscoll, R. L., & Klein, A. J. (2017). *USGS Spectral Library Version 7*. <https://doi.org/https://doi.org/10.3133/ds1035>
- Kombrink, H., Bridge, J. S., & Stouthamer, E. (2007). The alluvial architecture of the Coevorden Field (Upper Carboniferous), the Netherlands. *Netherlands Journal of Geosciences - Geologie En Mijnbouw*, 86(1), 3–14. <https://doi.org/10.1017/S0016774600021284>
- Le Bras, A., & Erard, S. (2003). Reflectance spectra of regolith analogs in the mid-infrared: effects of grain size. *Planetary and Space Science*, 51(4–5), 281–294. [https://doi.org/10.1016/S0032-0633\(03\)00017-5](https://doi.org/10.1016/S0032-0633(03)00017-5)
- Lodhi, V., Chakravarty, D., & Mitra, P. (2019). Hyperspectral Imaging System: Development Aspects and Recent Trends. *Sensing and Imaging*, 20(1), 35. <https://doi.org/10.1007/s11220-019-0257-8>
- Mathieu, M., Roy, R., Launeau, P., Cathelineau, M., & Quirt, D. (2017). Alteration mapping on drill cores using a HySpex SWIR-320m hyperspectral camera: Application to the exploration of an unconformity-related uranium deposit (Saskatchewan, Canada). *Journal of Geochemical Exploration*, 172, 71–88. <https://doi.org/10.1016/j.gexplo.2016.09.008>
- Mestdagh, M. M., Vielvoye, L., & Herbillon, A. J. (1980). Iron in kaolinite: II. The relationship between kaolinite crystallinity and iron content. *Clay Minerals*, 15(1), 1–13. <https://doi.org/10.1180/claymin.1980.015.1.01>

- Mijnlieff, H. F. (2020). Introduction to the geothermal play and reservoir geology of the Netherlands. *Netherlands Journal of Geosciences*, 99, e2. <https://doi.org/10.1017/njg.2020.2>
- Ministry of Economic Affairs and Climate Policy (MEA). (2017). *Natural resources and geothermal energy in the Netherlands*. <https://www.nlog.nl/sites/default/files/yearbook%202017-%20englishversion.pdf>
- Morad, S., Al-Ramadan, K., Ketzer, J. M., & De Ros, L. F. (2010). The impact of diagenesis on the heterogeneity of sandstone reservoirs: A review of the role of depositional facies and sequence stratigraphy. *AAPG Bulletin*, 94(8), 1267–1309. <https://doi.org/10.1306/04211009178>
- Okada, K. (2022). Breakthrough technologies for mineral exploration. *Mineral Economics*, 35(3–4), 429–454. <https://doi.org/10.1007/s13563-022-00317-3>
- Pineau, M., Mathian, M., Baron, F., Rondeau, B., Le Deit, L., Allard, T., & Mangold, N. (2022). Estimating kaolinite crystallinity using near-infrared spectroscopy: Implications for its geology on Earth and Mars. *American Mineralogist*, 107(8), 1453–1469. <https://doi.org/10.2138/am-2022-8025>
- Pontual, S., Merry, N., & Gamson, P. (1997a). *Archean Greenstone Gold, G-MEX*. AusSpec International.
- Pontual, S., Merry, N., & Gamson, P. (1997b). Practical Applications Handbook, G-MEX. In *Spectral Analysis guides for mineral exploration*. AusSpec International.
- Pontual, S., Merry, N., & Gamson, P. (1997c). Spectral Interpretation Field Manual, G-MEX. In *Spectral Analysis guides for mineral exploration*. AusSpec International.
- Post, F. R. (2021). *Deep Geothermal Potential of the Tubbergen Fm in the Twente area*. VU University of Amsterdam & TNO.
- Ringnér, M. (2008). What is principal component analysis? *Nature Biotechnology*, 26(3), 303–304. <https://doi.org/10.1038/nbt0308-303>
- Rodarmel, C., & Shan, J. (2002). Principal Component Analysis for Hyperspectral Image Classification. *Surv Land Inf Syst*, 62.
- Ruiz Hidalgo, D., Bacca Cortés, B., & Caicedo Bravo, E. (2021). Dimensionality reduction of hyperspectral images of vegetation and crops based on self-organized maps. *Information Processing in Agriculture*, 8(2), 310–327. <https://doi.org/10.1016/j.inpa.2020.07.002>
- Schmidt, V., McDonald, D. A., & Platt, R. L. (1977). Pore Geometry and Reservoir Aspects of Secondary Porosity in Sandstones. *Bulletin of Canadian Petroleum Geology*, 25(2), 271–290. <https://doi.org/10.35767/gscpgbull.25.2.271>
- Statistics Netherlands (CBS). (2023a). *How much of the energy we consume is renewable?*
- Statistics Netherlands (CBS). (2023b). *Renewable energy; consumption by energy source, technology and application*.
- TNO-GDN. (2024). *Tubbergen Formation*. DINOluket | Data and Information on the Dutch Subsurface.
- Tucker, M. E. (2001). *Sedimentary Petrology* (3rd ed.). Blackwell Science.
- Veenstra, E., de Groot, P., de Lange, J., Mol, A., & van den Heuvel, P. (2020). Geothermal potential of the Tubbergen Formation in the Twente region of east Netherlands. *Interpretation*, 8(4), SQ93–SQ103. <https://doi.org/10.1190/INT-2019-0277.1>
- Walker, T. R., Waugh, B., & Grone, A. J. (1978). Diagenesis in first-cycle desert alluvium of Cenozoic age, southwestern United States and northwestern Mexico. *Geological Society of America Bulletin*, 89(1), 19. [https://doi.org/10.1130/0016-7606\(1978\)89<19:DIFDAO>2.0.CO;2](https://doi.org/10.1130/0016-7606(1978)89<19:DIFDAO>2.0.CO;2)
- Whetten, J. T., & Hawkins, J. W. (1972). Diagenetic origin of greywacke matrix minerals. *Sedimentology*, 19(1–2), 144–146. <https://doi.org/10.1111/j.1365-3091.1972.tb00242.x>

- Wolela, A. M., & Gierlowski-Kordesch, E. H. (2007). Diagenetic history of fluvial and lacustrine sandstones of the Hartford Basin (Triassic–Jurassic), Newark Supergroup, USA. *Sedimentary Geology*, 197(1–2), 99–126. <https://doi.org/10.1016/j.sedgeo.2006.09.006>
- Worden, R. H., Armitage, P. J., Butcher, A. R., Churchill, J. M., Csoma, A. E., Hollis, C., Lander, R. H., & Omma, J. E. (2018). Petroleum reservoir quality prediction: overview and contrasting approaches from sandstone and carbonate communities. *Geological Society, London, Special Publications*, 435(1), 1–31. <https://doi.org/10.1144/SP435.21>
- Worden, R. H., & Morad, S. (1999). Clay Minerals in Sandstones: Controls on Formation, Distribution and Evolution. In *Clay Mineral Cements in Sandstones* (pp. 1–41). Wiley. <https://doi.org/10.1002/9781444304336.ch1>
- Zhou, Y., Wang, T., Fan, F., Chen, S., Guo, W., Xing, G., Sun, J., & Xiao, F. (2022). Advances on Exploration Indicators of Mineral VNIR-SWIR Spectroscopy and Chemistry: A Review. *Minerals*, 12(8), 958. <https://doi.org/10.3390/min12080958>

## APPENDICES

**Appendix 1:** Porosity-Permeability data of FLN - 01. \* indicates the disintegrated plugs, which do not have permeability values. Data were obtained from the core analysis report compiled by NAM (Kernanalyse | NAM 370.08.19 | Fleringen 1 (NLOG, 2023b)). The original report does not contain sample numbers. Permeability values indicated as “< 0.4 mD” were replaced with 0.2 mD.

Plug label	Depth (m)	Porosity (%)	Hor. Perm. (mD)	Plug label	Depth (m)	Porosity (%)	Hor. Perm. (mD)
1	1760.9	15.4	2.6	40	1776.3	11.0	0.5
3	1761.5	10.5	*	41	1776.6	12.1	1.0
4	1765.0	6.5	3.6	42	1776.9	13.2	1.0
5	1765.3	7.8	0.2	43	1777.2	7.1	0.2
6	1765.6	9.9	0.2	44	1777.5	5.2	*
7	1765.9	8.1	*	45	1779.2	5.8	*
8	1766.2	9.8	0.2	48	1784.7	4.6	*
9	1766.5	10.0	0.2	49	1785.0	5.3	0.2
10	1766.8	9.7	0.2	50	1785.3	8.0	0.2
11	1767.1	9.0	0.2	51	1785.6	6.6	*
12	1767.4	9.1	0.2	52	1785.9	7.2	0.6
13	1767.7	9.0	0.2	53	1788.8	7.5	0.2
14	1768.0	9.1	0.2	54	1789.1	4.4	0.2
15	1768.3	9.9	0.2	55	1789.4	8.5	*
16	1768.6	11.3	0.2	56	1789.8	5.3	0.2
17	1768.9	14.6	5.1	57	1790.1	10.4	0.4
19	1769.2	13.2	1.2	58	1790.4	12.8	0.6
20	1769.8	13.5	2.7	59	1790.7	13.2	1.4
21	1770.1	13.0	2.7	61	1791.3	15.0	8.4
22	1770.4	15.3	2.9	63	1791.9	17.2	60.0
23	1770.7	14.1	0.8	64	1792.2	17.6	43.0
24	1771.0	14.1	1.5	65	1792.5	17.7	36.0
25	1771.3	11.3	0.5	66	1792.8	18.1	43.0
26	1771.6	13.7	3.0	67	1793.1	17.8	76.0
27	1771.9	15.3	6.5	68	1793.4	18.4	178.0
28	1772.2	15.2	4.9	69	1793.7	18.4	165.0
29	1772.5	16.0	5.5	70	1794.0	15.4	26.0
30	1772.8	18.7	56.0	71	1794.3	14.5	23.0
31	1773.1	19.0	65.0	72	1794.6	15.3	0.2
32	1773.4	13.7	4.3	75	1795.5	14.0	0.2
33	1773.7	16.3	27.0	76	1795.8	15.8	34.0
34	1774.5	13.5	11.7	77	1796.1	16.2	40.0
35	1774.8	12.5	4.3	78	1796.4	16.7	41.0
36	1775.1	12.0	0.9	79	1796.7	6.5	0.6
37	1775.4	13.4	2.2	80	1797.0	11.8	1.8
38	1775.7	16.2	16.3	86	1799.5	15.6	16.7
39	1776.0	17.8	8.7	88	1800.1	11.0	0.4

Plug label	Depth (m)	Porosity (%)	Hor. Perm. (mD)
89	1800.6	11.5	2.3
90	1800.9	11.6	0.6
91	1801.2	12.0	0.6
92	1801.5	11.0	0.5
94	1802.1	13.3	1.2
95	1802.4	11.4	*
96	1802.7	10.0	0.8
97	1803.0	12.0	0.5
98	1803.3	13.2	0.5
99	1803.6	13.5	0.6
100	1803.9	13.9	0.8
101	1804.2	8.8	0.2
102	1804.5	13.7	1.2
103	1804.8	14.3	1.5
104	1805.1	15.6	2.4
105	1805.4	15.2	1.7
106	1805.7	13.1	0.9
107	1806.0	8.0	0.2
108	1806.3	10.8	0.2
109	1806.6	8.3	0.2
111	1807.2	16.6	2.9
112	1807.5	14.9	1.5
113	1807.8	16.3	2.8
114	1808.1	15.7	2.7
115	1808.4	13.4	1.0
116	1808.7	15.7	7.0
117	1809.0	16.0	7.8
118	1809.3	11.9	0.8
119	1810.3	12.7	0.6
121	1810.9	15.4	1.5
122	1811.2	15.0	1.4
123	1811.5	14.5	1.2
124	1811.8	13.2	0.7
125	1812.1	13.1	0.8
126	1812.4	12.3	*
127	1812.7	10.8	*
128	1813.0	10.8	0.6
129	1813.3	11.2	1.1
130	1816.2	7.0	0.2
131	1816.5	8.1	0.2
132	1816.8	6.3	1.0
133	1817.1	8.8	1.0
134	1817.4	6.5	0.2

Plug label	Depth (m)	Porosity (%)	Hor. Perm. (mD)
135	1817.7	4.7	*
136	1818.0	4.8	0.2
137	1822.7	4.4	0.2
138	1823.0	10.2	0.2
139	1823.3	11.5	0.4
141	1823.9	11.6	0.2
142	1824.2	11.8	0.2
143	1824.5	11.1	0.2
144	1824.8	12.2	0.2
145	1825.1	11.3	0.2
146	1825.4	9.3	0.2
147	1825.7	14.7	1.8
148	1826.0	14.7	2.1
149	1826.3	14.9	2.6
150	1826.6	14.3	2.4
152	1827.2	15.7	7.8
153	1827.5	14.5	4.0
154	1827.6	15.0	4.3
155	1827.9	15.3	8.7
156	1828.2	15.2	9.7
157	1828.5	15.4	15.6
158	1828.8	16.9	22.0
159	1829.1	10.8	0.4
160	1829.4	16.8	33.0
161	1829.7	15.3	5.1
162	1830.0	15.7	4.3
163	1830.3	13.6	1.8
164	1830.6	16.0	7.8
166	1831.4	9.1	0.6
167	1831.7	12.1	2.0
168	1832.0	10.3	0.7
169	1832.3	13.1	1.5
170	1832.6	11.7	0.6
171	1832.9	9.6	*
172	1833.2	11.4	0.7
173	1833.5	9.9	0.2
174	1833.8	8.6	0.2
175	1834.1	10.0	0.2
176	1834.4	7.7	0.4
177	1834.7	8.9	0.2
178	1835.0	8.2	0.2
179	1835.3	13.5	2.1
180	1835.6	13.5	3.3

Plug label	Depth (m)	Porosity (%)	Hor. Perm. (mD)
181	1835.9	13.4	3.2
182	1836.2	10.3	0.2
184	1836.8	14.5	2.9
185	1837.1	15.9	8.1
186	1837.4	14.7	4.2
187	1837.7	14.9	4.3
188	1838.0	15.3	3.7
189	1838.3	14.8	3.7
190	1838.6	14.6	3.6
191	1838.9	14.3	6.5
192	1839.2	13.0	0.8
193	1839.5	14.6	2.0
194	1839.8	14.2	4.3
195	1840.1	14.3	1.5
196	1840.4	7.0	0.2
197	1840.7	9.2	0.2
198	1841.0	12.8	1.1
199	1841.3	10.3	0.4
200	1841.6	8.6	0.2
201	1841.9	8.5	0.2
202	1842.2	9.7	0.2
203	1842.5	10.0	0.2
204	1842.8	10.0	0.2
206	1843.4	10.6	0.2
207	1843.7	10.7	0.2
208	1844.0	11.0	0.2
209	1844.3	10.5	0.4
210	1844.6	10.5	0.2
211	1844.9	10.4	0.2
212	1845.2	9.8	0.2
213	1845.5	9.1	0.2
214	1845.8	8.5	0.2
215	1846.1	10.7	0.4
216	1846.4	13.7	7.8
217	1846.7	12.4	3.8
218	1847.0	12.7	1.6
219	1861.6	4.7	14.7
220	1869.6	4.8	0.2
221	1869.9	5.3	*
222	1870.2	6.3	0.2
223	1870.5	3.8	0.2
224	1870.8	2.7	0.2
225	1871.1	3.1	0.2

Plug label	Depth (m)	Porosity (%)	Hor. Perm. (mD)
226	1874.2	3.9	0.2
227	1874.5	5.1	0.2
228	1875.7	4.5	0.2
229	1876.0	8.1	0.2
230	1876.3	9.9	0.2
231	1876.6	11.5	0.4
232	1876.8	7.6	0.2
233	1877.1	10.1	0.2
234	1877.4	7.5	0.2
235	1877.7	6.7	0.2
237	1878.3	7.3	0.2
238	1878.6	8.3	0.2
239	1878.9	14.2	2.2
240	1879.2	12.4	1.1
241	1879.5	14.3	18.7
242	1879.8	18.8	84.0
243	1880.1	17.2	21.0
244	1880.4	12.6	1.9
245	1880.7	12.8	1.7
246	1881.0	15.4	8.0
247	1881.3	15.0	10.2
248	1881.6	16.1	63.0
249	1881.9	18.4	182.0
250	1882.2	18.2	171.0
251	1882.5	18.6	184.0
252	1882.8	19.4	247.0
253	1883.1	18.8	158.0
254	1883.4	15.5	17.4
255	1883.7	14.5	14.0
256	1884.0	16.1	28.0
257	1884.3	17.0	63.0
259	1884.9	13.4	16.1
261	1885.5	16.6	21.0
262	1885.8	15.3	15.0
263	1886.1	14.4	7.2
264	1886.4	14.3	4.4
265	1886.7	17.7	59.0
266	1887.0	18.3	65.0
267	1887.3	15.1	13.8
268	1887.6	14.7	25.0
269	1887.9	18.1	141.0
270	1888.2	18.3	136.0
271	1888.5	17.5	46.0

Plug label	Depth (m)	Porosity (%)	Hor. Perm. (mD)
272	1888.8	15.1	21.0
273	1889.1	17.5	46.0
274	1889.4	16.3	57.0
275	1889.7	18.5	79.0
276	1890.0	18.6	171.0
277	1890.3	18.6	146.0
278	1890.6	18.7	159.0
279	1890.9	19.8	197.0
280	1891.2	13.7	6.7
281	1891.5	18.6	93.0
282	1891.8	17.0	41.0
283	1892.1	17.9	84.0
284	1892.4	17.3	74.0
285	1892.7	12.1	9.5
286	1893.0	11.2	0.2
287	1893.3	10.0	0.2
288	1893.6	2.7	0.2
289	1893.9	13.6	7.8
290	1894.2	17.1	87.0
291	1894.5	17.1	72.0
292	1894.8	18.1	81.0
293	1895.1	17.6	79.0
294	1895.4	16.9	41.0
295	1895.7	16.4	44.0
296	1896.0	16.7	69.0
297	1896.3	11.1	1.5
298	1896.6	15.8	85.0
299	1896.9	17.8	55.0
300	1897.2	17.4	58.0
301	1897.5	15.5	42.0
302	1897.5	7.9	0.2
303	1898.1	8.0	0.2
304	1899.0	12.3	3.8
305	1899.3	14.1	3.1
306	1899.6	16.1	16.3
307	1899.9	15.4	8.7
308	1900.2	14.5	5.7
309	1900.8	14.7	7.5
310	1901.1	14.4	6.9
311	1901.4	14.3	10.6
312	1901.7	17.0	25.0
313	1902.0	18.3	156.0
314	1902.3	15.6	63.0

Plug label	Depth (m)	Porosity (%)	Hor. Perm. (mD)
315	1902.6	17.8	97.0
316	1902.9	15.6	29.0
317	1903.2	8.5	0.8
318	1903.5	10.5	0.5
319	1903.8	8.9	0.4
320	1904.1	10.1	0.4
321	1904.4	9.2	0.4
322	1904.7	8.5	0.4
323	1905.0	9.2	*
325	1905.6	9.5	0.2
326	1905.9	9.7	0.2
327	1906.2	8.3	0.2
328	1906.5	9.1	0.2
329	1906.8	10.3	0.2
330	1907.1	12.7	0.4
331	1907.4	12.4	0.7
332	1907.7	12.9	0.6
333	1908.0	10.3	0.2
334	1908.3	12.4	0.5
335	1908.6	10.3	0.2
336	1908.9	10.7	0.2
337	1909.2	11.4	0.4
338	1909.5	12.9	0.8
339	1909.8	12.9	0.7
340	1910.1	12.4	0.7
341	1910.4	12.0	0.6
342	1910.7	11.8	0.6
343	1912.0	6.4	2.2
344	1912.3	13.4	2.3
345	1912.6	13.7	12.2
346	1912.9	3.3	3.7
347	1913.2	6.1	0.2
348	1913.5	6.1	0.2
349	1913.8	5.6	0.2
350	1914.1	5.2	0.2
351	1914.4	7.5	0.2
352	1914.7	9.9	0.5
353	1915.0	11.8	2.2
354	1915.3	13.4	3.4
355	1915.6	13.6	9.9
356	1916.0	7.3	0.2
357	1916.3	9.9	*
358	1916.6	8.5	0.6

Plug label	Depth (m)	Porosity (%)	Hor. Perm. (mD)
359	1916.9	3.5	2.2
361	1917.5	5.2	0.2
362	1917.8	4.2	0.2
363	1924.0	15.3	13.1
364	1924.3	14.2	3.6
365	1924.6	14.0	6.5
366	1924.9	13.9	4.0
367	1925.2	15.0	15.0
368	1925.5	10.2	0.4
369	1925.8	11.0	0.5
371	1926.4	15.1	7.8
372	1926.7	15.4	8.8
373	1927.0	8.6	0.2
374	1927.3	14.7	3.2
375	1927.6	10.6	0.2
376	1927.9	13.7	2.3
377	1928.2	9.6	0.2
378	1928.5	10.9	0.4
379	1928.8	10.7	0.4
380	1929.1	10.2	0.4
381	1929.4	11.1	0.8
382	1929.7	11.7	0.8
383	1930.0	5.4	*
384	1930.3	13.5	1.7
385	1930.6	12.6	1.1
386	1930.9	11.7	0.6
387	1931.2	10.7	0.2
389	1931.8	10.1	0.2
390	1932.1	10.4	0.2
391	1932.4	10.1	0.2
392	1932.7	10.3	0.4
393	1933.0	10.3	0.4
394	1933.3	10.5	0.4
395	1933.6	10.4	0.5
396	1933.9	15.5	8.4
397	1934.2	15.6	12.6
398	1934.5	16.7	41.0
399	1934.8	11.2	1.5
400	1935.1	7.5	2.1
401	1940.0	9.5	0.4
402	1940.3	12.7	4.2
403	1940.6	13.4	11.5

Plug label	Depth (m)	Porosity (%)	Hor. Perm. (mD)
404	1940.9	15.0	29.0
405	1941.2	16.8	66.0
406	1941.5	15.2	25.0
407	1941.8	12.0	5.9
408	1942.1	15.5	24.0
409	1942.4	14.6	26.0
410	1942.7	16.8	61.0
411	1943.0	14.8	20.0
412	1943.3	17.4	69.0
413	1943.6	14.7	76.0
414	1943.9	15.7	33.0
415	1944.2	12.7	6.0
416	1944.5	16.8	59.0
417	1944.8	17.8	74.0
418	1945.1	17.8	141.0
419	1945.4	15.9	44.0
420	1945.7	17.8	*
421	1946.0	15.9	*
422	1946.3	16.7	49.0
423	1946.6	15.4	31.0
424	1946.9	19.1	136.0
425	1947.2	18.4	69.0
426	1947.5	18.6	86.0
427	1947.8	18.9	74.0
428	1948.1	18.9	136.0
429	1948.4	17.8	*
431	1949.0	19.1	158.0
432	1949.3	18.2	164.0
433	1949.6	18.4	68.0
434	1949.9	18.3	60.0
435	1950.2	14.0	4.4
436	1950.5	11.1	1.1
437	1950.8	7.6	0.2
438	1951.1	15.3	21.0
439	1951.4	15.3	*
440	1951.7	15.2	16.9
441	1952.0	17.0	*
442	1952.3	16.5	22.0
443	1952.6	16.5	55.0
444	1952.9	16.9	*
445	1953.2	17.9	61.0
446	1953.5	16.9	54.0

Plug label	Depth (m)	Porosity (%)	Hor. Perm. (mD)
447	1953.8	16.4	53.0
448	1954.1	17.3	71.0
449	1954.4	16.2	*
450	1954.7	17.1	*
451	1955.0	17.2	153.0
452	1955.3	16.9	74.0
454	1955.9	16.0	42.0
455	1956.2	17.7	63.0
456	1956.5	17.2	87.0
457	1956.8	18.3	94.0
458	1957.1	14.6	9.9
459	1957.4	12.7	2.5
460	1957.7	12.9	2.7
461	1958.0	14.0	2.9
462	1958.3	11.7	1.4
463	1958.6	13.7	2.6
464	1958.9	11.9	1.3
465	1959.2	16.3	176.0
466	1959.5	10.6	0.7
467	1959.8	13.8	3.6
468	1960.1	14.1	3.4
469	1960.4	12.0	1.0
470	1960.7	7.9	0.2
471	1961.0	11.7	1.0
472	1961.3	11.6	0.8
473	1961.6	11.2	0.7
474	1961.9	10.9	0.6
475	1962.2	14.5	7.8
476	1962.5	16.3	29.0
477	1962.8	16.5	27.0
478	1963.1	17.1	*
479	1963.4	16.5	33.0
480	1963.7	15.2	*
481	1964.0	17.4	55.0
482	1964.3	17.1	51.0

**Appendix 2:** Porosity-permeability analyses of 61 FLN samples from two laboratories: *C. Deilmann* Mining Company (Germany) and *NAM* (Netherlands). A 0.05 – 0.1m difference is seen in the mentioned depths between the two reports, possibly caused by the measurement scale.

German			Dutch		
Depth (m)	durdilässigkeit / Permissibility (mD)	nutzporosität / Usefulporosity (%)	Depth (m)	Permeability (mD)	Porosity (%)
1772.75	3.0	13.8	1772.8	56.0	18.7
1773.75	21.0	16.2	1773.7	27.0	16.3
1774.5	5.0	12.6	1774.5	11.7	13.5
1775.8	11.0	14.9	1775.7	16.3	16.2
1777.0	1.0	11.6	1776.9	1.0	13.2
1790.2	2.0	11.8	1790.1	0.4	10.4
1791.1	8.0	13.6	1791.0	2.3	13.3
1793.5	108.0	15.2	1793.4	178.0	18.4
1796.1	57.0	15.7	1796.1	40.0	16.2
1799.0	306.0	17.0	1799.5	16.7	15.6
1801.6	1.0	12.0	1801.5	0.5	11
1804.9	2.0	13.3	1804.8	1.5	14.3
1808.0	6.0	16.5	1808.1	2.7	15.7
1812.0	0.5	8.9	1812.1	0.8	13.1
1813.9	2.0	12.3	1813.3	1.1	11.2
1823.2	1.0	9.6	1823.3	0.4	11.5
1825.7	4.0	15.4	1825.7	1.8	14.7
1827.6	5.0	14.1	1827.6	4.3	15
1829.8	20.0	16.0	1829.7	5.1	15.3
1832.3	3.0	13.1	1832.3	1.5	13.1
1833.9	0.6	8.2	1833.8	<0.4	8.6
1837.3	9.0	15.4	1837.4	4.2	14.7
1838.1	4.0	14.5	1838.0	3.7	15.3
1841.0	0.9	8.4	1841.0	1.1	12.8
1843.3	0.7	7.3	1843.4	<0.4	10.6
1844.2	0.8	10.5	1844.3	0.4	10.5
1846.3	0.8	9.2	1846.4	7.8	13.7
1874.4	0.7	5.7	1874.5	<0.4	5.1
1876.5	0.9	8.5	1876.6	0.4	11.5
1879.8	0.4	7.8	1879.8	84.0	18.8
1880.0	47.0	16.8	1880.1	21.0	17.20
1880.9	7.0	14.9	1881.0	8.0	15.4
1882.2	111.0	16.9	1882.2	171.0	18.2
1884.1	33.0	15.1	1884.0	28.0	16.1
1886.2	5.0	13.8	1886.1	7.2	14.4
1890.1	161.0	17.7	1890.0	171.0	18.6
1893.1	0.7	8.6	1893.0	<0.4	11.2
1894.8	106.0	16.8	1894.8	81.0	18.1
1897.8	0.6	8.5	1897.8	<0.4	7.9

German			Dutch		
Depth (m)	durdilässigkeit / Permissibility (mD)	nutzporosität / Usefulporosity (%)	Depth (m)	Permeability (mD)	Porosity (%)
1899.9	4.0	12.8	1899.9	8.7	15.4
1904.1	1.0	9.4	1904.1	0.4	10.1
1906.5	0.4	6.1	1906.5	<0.4	9.1
1908.1	2.0	12.3	1908.0	<0.4	10.3
1912.8	5.0	12.3	1912.9	3.7	3.3
1913.8	0.3	5.8	1913.8	<0.4	5.6
1915.7	5.0	12.6	1915.6	9.9	13.6
1917.5	0.2	5.9	1917.5	<0.4	5.2
1924.5	18.0	15.3	1924.6	6.5	14
1926.6	11.0	14.6	1926.7	8.8	15.4
1931.2	2.0	10.4	1931.2	<0.4	10.7
1934.4	44.0	16.5	1934.5	41.0	16.7
1941.3	23.0	14.5	1941.2	66.0	16.8
1944.0	36.0	15.5	1943.9	33.0	15.7
1947.8	189.0	18.0	1947.8	74.0	18.9
1950.1	8.0	13.7	1950.2	4.4	14
1953.4	218.0	16.3	1953.5	54.0	16.9
1957.6	8.0	14.1	1957.7	2.7	12.9
1959.0	2.0	13.3	1958.9	1.3	11.9
1959.5	146.0	15.9	1959.5	0.7	10.6
1961.6	3.0	11.3	1961.6	0.7	11.2
1963.4	32.0	15.9	1963.4	33.0	16.5

**Appendix 3:** Porosity-Permeability data of REU - 01. \* Indicates the disintegrated plugs which do not have permeability values. Data were obtained from the core analysis report compiled by NAM (Core Analysis, Reutum 1 (NLOG, 2023b)). Permeability values indicated as “< 0.4 mD” were replaced with 0.2 mD.

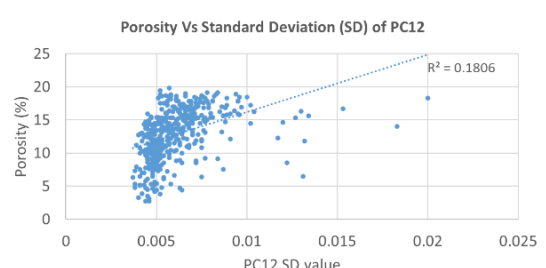
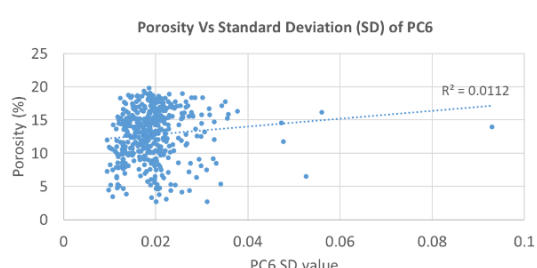
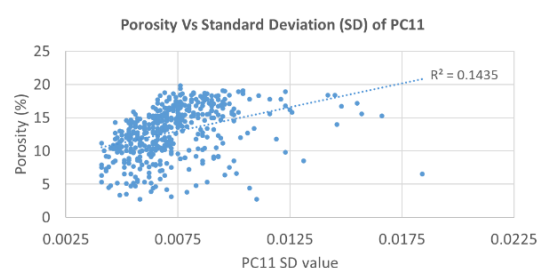
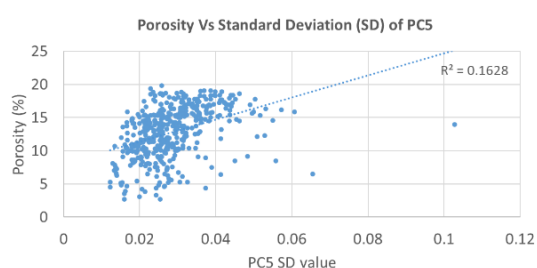
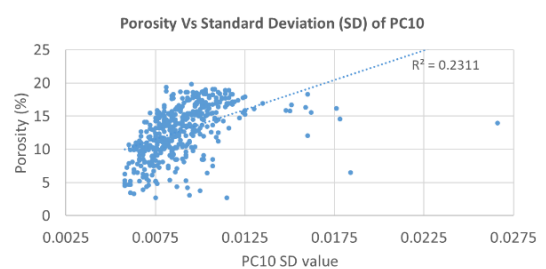
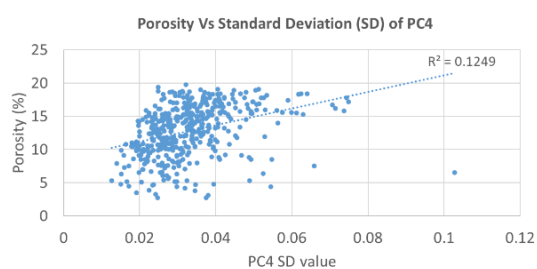
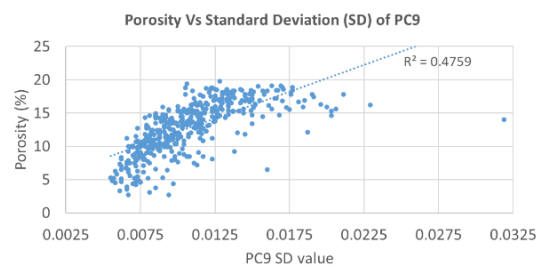
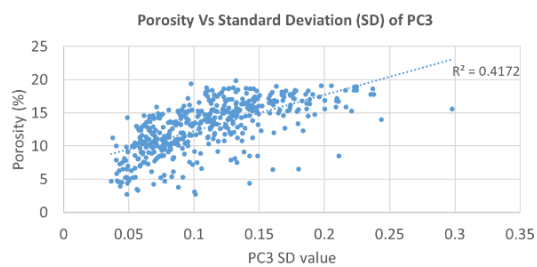
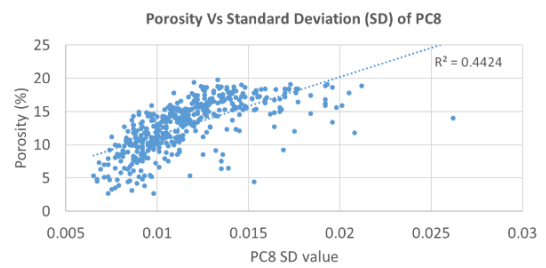
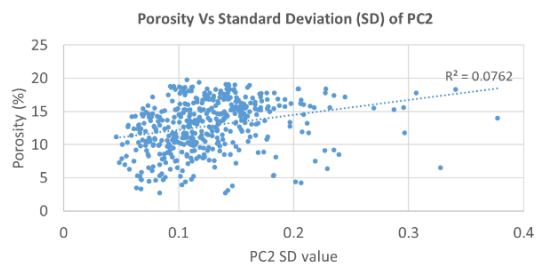
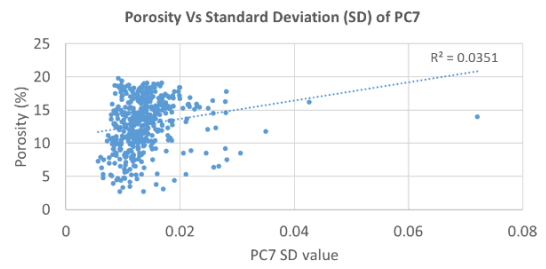
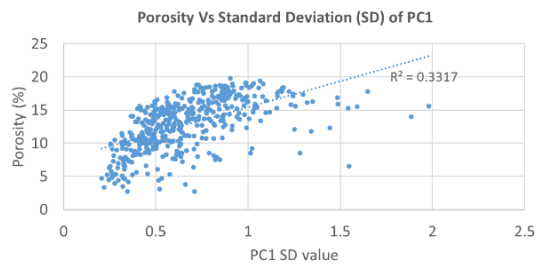
Plug label	Depth (m)	Porosity (%)	Hor. Perm. (mD)	Plug label	Depth (m)	Porosity (%)	Hor. Perm. (mD)
1	2074.0	8.6	*	45	2258.6	13.9	303
2	2074.3	7.4	101.0	46	2258.9	10.7	45.0
3	2074.6	7.1	*	47	2259.2	12.1	205.0
4	2074.9	6.9	*	48	2259.5	11.4	106
5	2075.2	6.1	0.2	49	2259.8	8.9	*
6	2075.5	6.1	0.2	50	2260.1	12.5	176.0
7	2075.8	7.8	51	51	2260.4	5.4	0.2
8	2076.1	8.2	39.0	52	2260.7	11.9	296.0
9	2076.3	6.4	0.2	53	2261.0	11.9	227.0
10	2076.6	8.5	0.2	54	2261.3	13.6	290.0
11	2076.9	7.3	0.2	55	2261.6	13.2	281
12	2077.2	7.5	*	56	2261.9	13.2	319.0
13	2077.5	5.9	*	57	2262.2	14.3	1622.0
14	2077.8	6.2	*	58	2262.5	14.3	674.0
15	2165.0	5.1	0.2	59	2262.8	17.4	2698.0
16	2250.1	7.6	0.2	60	2263.1	15.3	2413.0
17	2250.4	8.7	0.2	61	2263.4	15.6	1622.0
18	2250.7	8.4	0.2	62	2263.7	15.0	1323.0
19	2251.0	7.0	0.2	63	2264.5	12.7	55.0
20	2251.3	8.1	0.2	64	2264.8	10.8	*
21	2251.6	10.3	0.2	65	2265.1	13.7	168.0
22	2251.9	9.0	0.2	66	2265.4	12.2	96.0
23	2252.2	10.1	0.2	67	2265.7	11.2	159.0
24	2252.5	9.6	0.2	68	2266.0	14.7	1780.0
25	2252.8	9.6	0.2	69	2266.3	14.9	1622.0
26	2253.1	7.4	0.2	70	2266.6	7.5	0.2
27	2253.4	9.5	0.2	71	2266.9	12.6	65.0
28	2253.7	7.6	0.2	72	2536.6	7.0	0.2
29	2254.0	6.8	0.2	73	2536.9	7.3	0.2
30	2254.3	6.2	70.0	74	2537.2	8.4	0.2
31	2254.6	4.5	0.2	75	2537.5	10.1	0.2
32	2254.9	3.3	*	76	2537.8	9.2	0.2
33	2255.1	4.1	*	77	2538.1	12.2	42.0
34	2255.4	7.0	*	78	2538.4	4.3	265.0
35	2255.7	13.1	287.0	79	2538.7	6.4	0.2
36	2256.0	13.0	74.0	80	2539.0	11.7	69.0
37	2256.3	12.9	216.0	81	2539.3	13.1	116.0
38	2256.6	12.3	100.0	82	2539.6	9.0	0.2
39	2256.9	10.9	45.0	83	2539.9	11.2	84
40	2257.2	14.2	248.0	84	2540.2	9.8	0.2
41	2257.5	13.4	236.0	85	2540.5	9.4	0.2
42	2257.8	14.9	508.0	86	2540.8	9.0	41.0
43	2258.0	11.6	69.0	87	2541.1	3.4	383.0
44	2258.3	13.6	276	88	2541.4	9.8	105.0

---

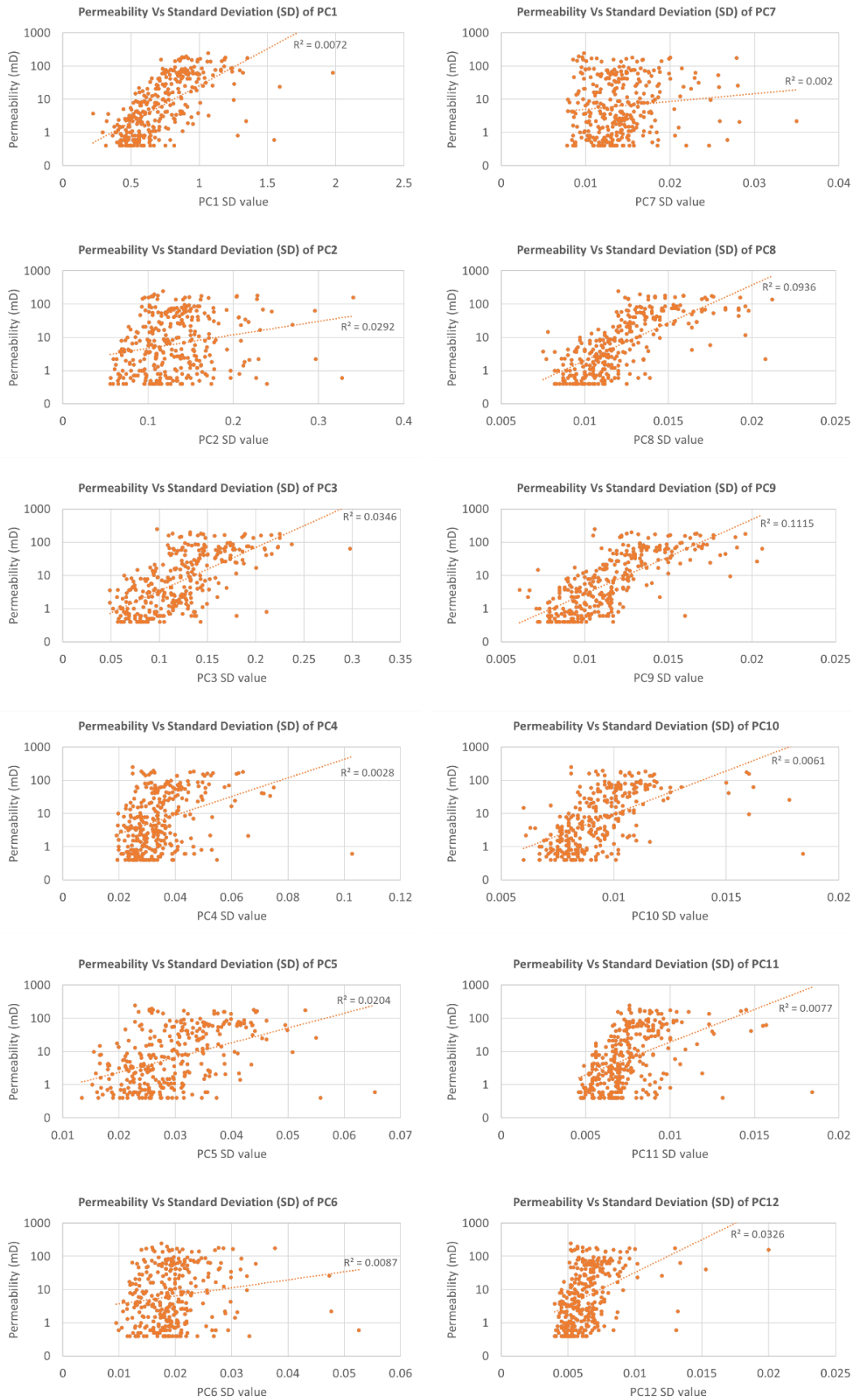
<b>Plug label</b>	<b>Depth (m)</b>	<b>Porosity (%)</b>	<b>Hor. Perm. (mD)</b>
89	2541.7	3.5	0.2
90	2542.0	6.1	0.2
91	2542.3	8.3	0.2
92	2542.6	3.7	0.2
93	2542.9	7.6	0.2
94	2543.2	5.0	0.2
95	2543.5	9.7	0.2
96	2543.8	10.2	43.0
97	2544.1	6.8	0.2
98	2544.4	9.4	51.0
99	2544.7	10.8	105.0
100	2545.3	7.3	0.2
101	2545.6	7.7	0.2
102	2545.9	8.0	0.2
103	2546.2	9.7	54.0
104	2546.5	8.2	0.2
105	2546.8	7.9	0.2
106	2547.1	8.4	0.2
107	2547.4	8.2	0.2
108	2547.7	5.6	0.2

---

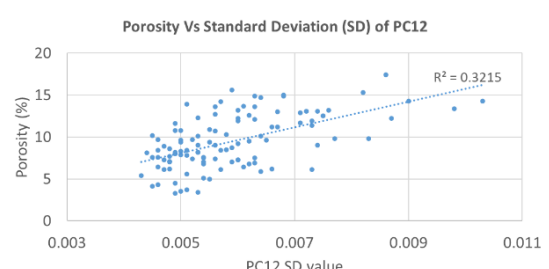
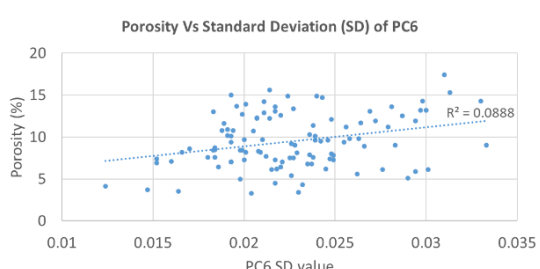
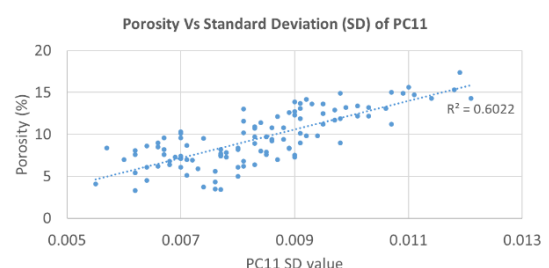
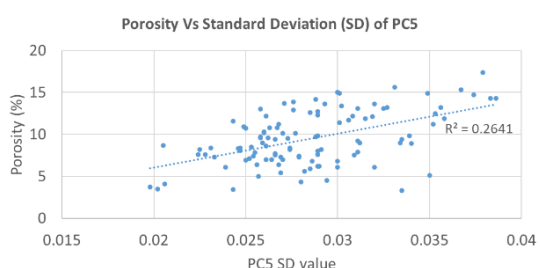
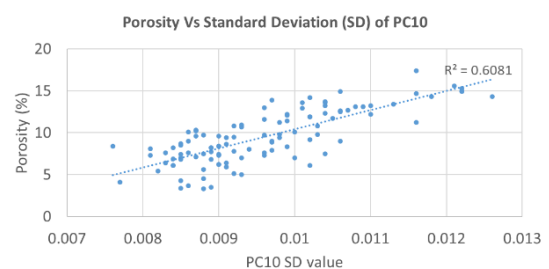
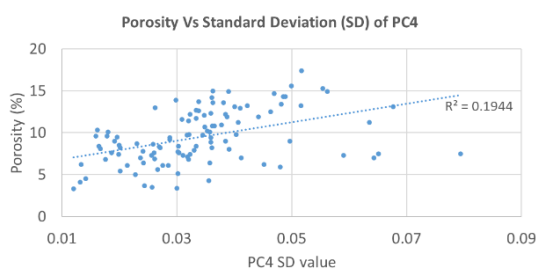
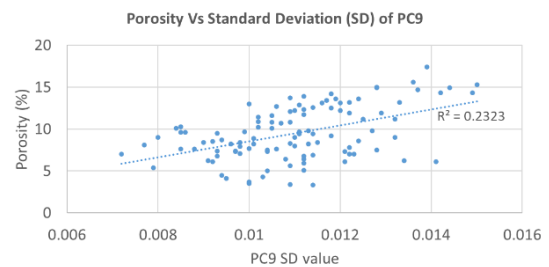
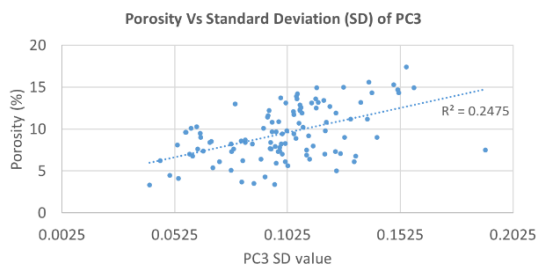
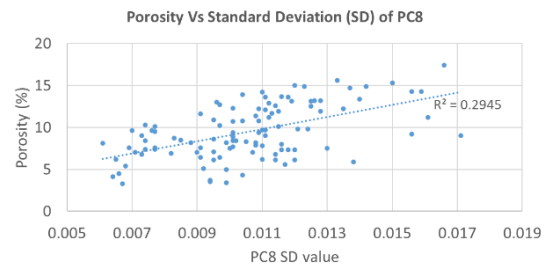
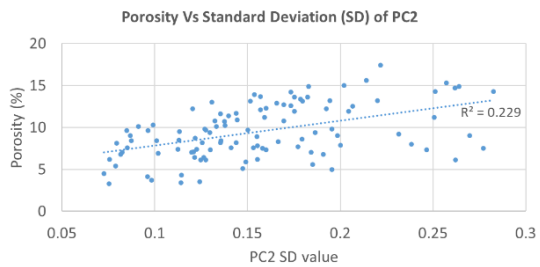
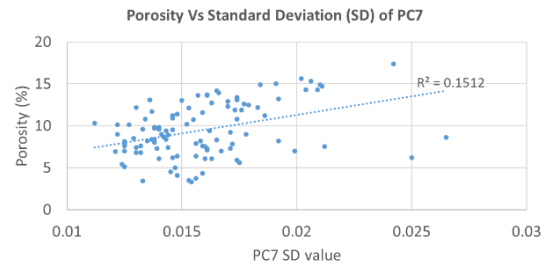
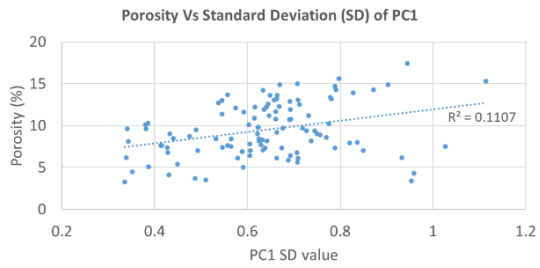
**Appendix 4:** Scatterplots of FLN Porosity vs Standard Deviation (SD) of the first 12 Principal Component (PC) bands.



**Appendix 5:** Scatterplots of FLN Permeability vs Standard Deviation (SD) of the first 12 Principal Component (PC) bands.



**Appendix 6:** Scatterplots of REU Porosity vs Standard Deviation (SD) of the first 12 Principal Component (PC) bands.



**Appendix 7:** Scatterplots of REU Permeability vs Standard Deviation (SD) of the first 12 Principal Component (PC) bands.

